Differentiation of MOR Basalt at 200 MPa: Experimental Techniques and Influence of H_2O and fO_2 on Phase Relations and Liquid Line of Descent

Differentiation von MOR Basalt bei 200 MPa: Experimentelle Grundlagen und Einfluß von H_2O und fO_2 auf Phasenbeziehungen und Schmelzentwicklung

Von dem Fachbereich Geowissenschaften und Geographie

der Universität Hannover

zur Erlangung des Grades eines

DOKTORS DER NATURWISSENSCHAFTEN

Dr. rer. nat.

genehmigte Dissertation

von

Dipl.-Geol. Jasper Berndt

geboren am 11.06.1972 in Hildesheim

2002

Abstract

This study presents improvements of internally heated pressure vessels to realize high pressure experiments at controlled fO$_2$ in low viscosity systems such as basaltic ones. The new design is a combination of two experimental techniques: a hydrogen sensor membrane made of platinum to measure fH$_2$, and therefore fO$_2$, and a rapid-quench system to avoid crystallization of low viscosity melts during quench. The new technique was used to determine the effect of fO$_2$ on water solubility in a melt with MORB composition. The results show that there is a small but significant decrease of water solubility with decreasing fO$_2$ from MnO-Mn$_3$O$_4$- to QFM-buffer conditions in the pressure range 50 – 200 MPa.

Crystallization experiments were performed at 200 MPa in the temperature range 1150 °C – 950 °C at a fO$_2$ corresponding to the MnO-Mn$_3$O$_4$- and QFM-buffer to assess the role of aH$_2$O, fO$_2$, and bulk water content on phase relations and compositions in a primitive (B1) and evolved (B2; MnO-Mn$_3$O$_4$-buffer only) MORB system. Following phases were observed: glass, olivine, clino- and orthopyroxene, plagioclase, magnetite, ilmenite, and amphibole.

B1 phase relations show that olivine is the liquidus phase followed by plagioclase + clinopyroxene, independently of fO$_2$. Amphibole is only present at 950 °C and 1000 °C at water-saturated conditions. In experiments at the MnO-Mn$_3$O$_4$-buffer, olivine is not stable at 950 °C but orthopyroxene is always observed. In contrast, at reducing conditions (QFM-buffer) magnetite and orthopyroxene are not stable.

It is shown that variations of the bulk water content influence significantly phase relations and compositions, as a result of a simultaneous variation of aH$_2$O, fO$_2$, and melt fraction. Increasing aH$_2$O results in an increase of X_{Fo} in olivine and Mg# of the melt due to increasing fO$_2$. In addition, increasing bulk water content (constant aH$_2$O and fO$_2$) has the same effect due increasing melt fraction. CaO content of olivine is not only dependent on melt anhydrous composition and X_{Fo}, but on aH$_2$O. Amphibole was only found to be stable at water-saturated conditions (melt water content > 5.0 wt% H$_2$O). Its stability is also dependent on the residual melt composition, which is a function of the bulk water content in the system. Liquid lines of descent obtained at high and low fO$_2$ are mainly controlled by the fO$_2$ and only to a little extent by aH$_2$O. Residual liquids from experiments conducted at a fO$_2$ corresponding to the QFM-buffer show a tholeiitic differentiation trend. The crystallization of magnetite at a fO$_2$ corresponding to the MnO-Mn$_3$O$_4$-buffer results in a continuous decrease of the FeO*/MgO of the residual melt causing a calc-alkaline differentiation trend. SiO$_2$–rich residual melts can be obtained under both, oxidizing and reducing fO$_2$ but at least one fractionation step is required to reach plagiogranitic residual melt compositions.

Zusammenfassung

Die in der ozeanischen Kruste ablaufenden Differentiationsprozesse von subalkalischen tholeiitischen Magmen sind bislang wenig erforscht worden. Insbesondere der genaue Mechanismus der Entwicklung von SiO_2-reichen Schmelzen aus MORB Magmen ist ungeklärt. Vorhandene experimentelle Ergebnisse aus basaltischen Systemen, die meist bei Drücken von 1 bar unter trockenen Bedingungen durchgeführt wurden, reichen nicht aus, um die ablaufenden Differenzierungsprozesse zu verstehen, da MOR Basalte im initialen Stadium der Differentiation bis zu 0.5 gew% H_2O enthalten können. So zeigen petrographische und strukturelle Befunde aus Ophiolithen an, daß die Kristallisation der Plagiogranite bei Drücken zwischen 100 und 200 MPa und einer Wasseraktivität ($a$$H_2O$) > 0.5 erfolgte. Daher kann die Rolle der für die SiO_2-Anreicherung der Restschmelze sehr wichtigen, $f$$O_2$ -sensiblen Fe-Ti-Oxide nicht aus 1 bar Studien abgeleitet werden. Um die natürlichen Bedingungen (Druck, Temperatur, $a$$H_2O$, $f$$O_2$) experimentell präzise einstellen und die ablaufenden Differentiationsprozesse nachvollziehen zu können, mußte eine spezielle Apparatur für intern beheizte Gasdruckanlagen entwickelt werden. Damit ist es möglich, durch schnelles Abkühlen der Probenkapsel nach dem Experiment Ungleichgewichtskristallisation zu verhindern und durch Einbringen einer Wasserstoffmembrane in die Versuchsanlage unter Verwendung von Ar/H_2-Gemischen als Druckmedium die Sauerstoffugazität ($f$$O_2$) entsprechend den natürlichen Bedingungen (~QFM –Puffer) einzustellen und zu variieren.

Diese neue Technik wurde zunächst benutzt, um den Einfluß der Sauerstoffugazität auf die Wasserlöslichkeit in MORB Schmelzen zu untersuchen. Die Versuche wurden dabei unter sehr oxidierenden, intrinschen $f$$O_2$-Bedingungen (MnO-$Mn_3O_4$-Puffer) und reduzierenden $f$$O_2$-Bedingungen (QFM-Puffer) durchgeführt. Dabei hat sich gezeigt, daß die Wasserlöslichkeit im Druckbereich 50-200 MPa mit abnehmendem $f$$O_2$ ebenfalls abnimmt.

Für die Experimente zur Klärung der Genese von SiO_2-reichen Restschmelzen unter krustalen Druckbedingungen wurden unter Verwendung der oben beschriebenen Technik Kristallisationversuche mit einem primitiven MORB Glas (B1) bei 200 MPa und einem Temperaturintervall von 1150 °C bis 950 °C durchgeführt. Die Sauerstoffugazität wurde ebenfalls variiert und entsprach den oxidierenden MnO-Mn_3O_4- und den reduzierenden QFM-Puffer-Bedingungen. Um den Einfluß der Wasseraktivität zu untersuchen, wurden vier Startzusammensetzungen mit unterschiedlichen H_2O-Gehalten verwendet (zwischen 0.35 und 4.7 gew%). Weiterhin wurden mit einem zweiten, stärker differenzierten MORB Glas (B2) Versuche durchgeführt, das in seiner Zusammensetzung dem erstem, primitiven Glas B1 nach 50% Kristallisation entsprach.

Folgende Phasen konnten in den experimentellen Versuchsprodukten beobachtet werden: Olivin, Klino- und Orthopyroxen, Plagioklas, Magnetit, Ilmenit, Amphibol und Schmelze. In der primitiven B1 Zusammensetzung ist Olivin, unabhängig von der Sauerstoffugazität, die Liquidusphase, gefolgt von Plagioklas und Klinopyroxen. Die Amphibolstabilität ist auf Temperaturen von 950 °C (QFM-Puffer) und 1000 °C (MnO-Mn$_3$O$_4$-Puffer) in Versuchen mit einer Wasseraktivität = 1 begrenzt. Magnetit tritt nur bei oxidierenden Versuchsbedingungen bei Temperaturen zwischen 1100 °C und 1050 °C auf, während das Ilmenit-Stabilitätsfeld, unabhängig von der Sauerstoffugazität, auf 950 °C bei niedrigem Wassergehalt begrenzt ist. Unter oxidierenden Bedingungen ist Olivin, unabhängig vom Wassergehalt, bei Versuchstemperaturen von 950 °C nicht mehr stabil und wird durch Orthopyroxen ersetzt. In der stärker differenzierten Zusammensetzung B2, die nur bei oxidierenden Bedingungen untersucht wurde, ist Magnetit die Liquidusphase, gefolgt von Klinopyroxen, Plagioklas, Ilmenit und Orthopyroxen.

Sowohl hinsichtlich der Phasenbeziehungen als auch der Zusammensetzungen kann festgestellt werden, daß der unterschiedliche Wassergehalt der Startzusammensetzung signifikanten Einfluß hat. Dies ist das Resultat der wechselwirkenden Parameter aH$_2$O, fO$_2$ und Schmelzmenge. Mit ansteigender Wasseraktivität steigt zugleich auch die Sauerstoffugazität, welche wiederum die Mg-Zahl der Schmelze und damit die Olivinzusammensetzung beeinflußt. Weiterhin ist der CaO-Gehalt der Olivine nicht allein von der Oxidaktivität in der trockenen Schmelze abhängig, sondern wird durch gelöstes Wasser, welches CaO in der Schmelze stabilisiert, reduziert.

Der Vergleich der B1 Restschmelzzusammensetzungen bei Versuchen unter oxidierenden und reduzierenden Bedingungen zeigt, daß die Sauerstoffugazität, unabhängig vom Wassergehalt, der entscheidende Parameter bei der Differentiation ist. Bei reduzierenden Bedingungen nimmt das FeO/MgO-Verhältnis kontinuierlich zu und zeigt einen tholeiitschen Trend. Die Kristallisation von Magnetit bei oxidierenden Bedingungen hingegen bewirkt eine FeO-Verarmung der Schmelze, was einen kalk-alkalischen Differentiationstrend zur Folge hat. Bezüglich der Genese von sehr SiO$_2$-reichen Restschmelzen muß festgestellt werden, daß die experimentelle Differentiation der primitiven B1 Zusammensetzung nur einen maximalen SiO$_2$-Gehalt von etwa 60 gew% erreicht. Typische Plagiogranite zeigen jedoch SiO$_2$-Gehalte zwischen 65 und 75 gew%. Diese Schmelzzusammensetzungen konnten experimentell nur mit der stärker differenzierten B2 Zusammensetzung erreicht werden. Dies deutet darauf hin, daß wenigstens ein Fraktionierungsschritt für die Entstehung von SiO$_2$-reichen Schmelzen aus MORB Magmen nötig ist.

Danksagung

Table of Contents

1. Experimental Techniques: A combined Rapid-Quench and H_2-Membrane Setup for Internally Heated Pressure Vessels

1.1. Introduction

Experimental investigations on the influence of oxygen fugacity (fO_2) and water activity (aH_2O) on phase relationships and physicochemical properties of basaltic, low-viscosity, volatile- and iron-bearing systems at geologically relevant conditions require the development of special vessel and furnace setups with the following features: 1. The maximum temperature must at least reach 1200 °C because of the high liquidus temperature of basaltic compositions. 2. Temperature (T) and pressure (p) in the range 0.05 – 1GPa must be held precisely for long duration if equilibrium crystal-liquid phase studies are performed. 3. pH_2 has to be controlled accurately to achieve an exact determination of fO_2 and fH_2O during the experiments. 4. The iron-loss from the sample to the container must be minimized. 6. The experimental setup has to be equipped with a rapid-quench system to quench the charges within a few seconds to avoid the formation of quench crystals in low-viscosity, hydrous compositions. Such design features can be attained best using internally heated pressure vessels (IHPV).

The general features of IHPV were described by Holloway (1971). The main advantages can be summarized as follows: p and T uncertainties are smaller than in piston cylinder apparatus; the relatively large volume of the IHPV under hydrostatic, Ar-medium pressure allows the use of highly sophisticated furnace- and sample holder apparatuses; the maximum capsule size is generally larger in IHPV when compared to piston cylinder or cold seal pressure vessels (CSPV). Roux and Lefevre (1992) and Holloway et al. (1992) described a rapid-quench system for IHPV that allows high-temperature and high-pressure experiments with basaltic liquids and quench rates of about several hundred degrees Celsius per second. A major weakness of their IHPV rapid-quench setup is the lack of fO_2 monitoring which is important for experiments on iron-bearing compositions. The effect of fO_2 on phase relationships in basaltic liquids has been the object of numerous studies using 1 atm furnaces (e.g., Osborn, 1959; Presnall, 1966; Juster et al., 1989; Snyder et al., 1993; Toplis and Carroll, 1995; Toplis

and Carroll, 1996;). However, the influence of volatiles is not considered in these studies. The effect of pressure, H_2O, and fO_2 on basaltic compositions has also been investigated by numerous authors (e.g., Yoder and Tilley, 1962; Hamilton et al., 1964; Holloway and Burnham, 1972; Helz, 1973; Helz, 1976) mostly using the double-capsule technique (Eugster, 1957; Eugster and Wones, 1962) or intrinsic buffered fO_2 -conditions. In these studies the analyses of liquids and phases were often complicated by the formation of quench crystals during cooling. Additionally, the lifetime of solid buffers limits the duration of the experiments (Scaillet et al., 1992) and the large size of the whole sample and buffer charge can even cause quench crystals using the conventional rapid-quench setup of Roux and Lefevre (1992) and Holloway et al. (1992).

A further technique for the control and measurement of fO_2 is the H_2-membrane (Shaw, 1963). Several studies showed the reliability of this method for experiments under various p, T, and fO_2 in CSPV (Hewitt, 1977; Hewitt, 1978; Gunter et al., 1979; Gunter et al., 1987; Schmidt et al., 1995; Frantz et al., 1977) and IHPV (Piwinskii et al., 1973; Scaillet et al., 1992). Thus, the combination of a rapid-quench system and the H_2-membrane technique in IHPV was challenging. It fulfills the criteria discussed above to conduct experiments with low viscosity, volatile- and iron- bearing basaltic compositions. We developed an experimental design that
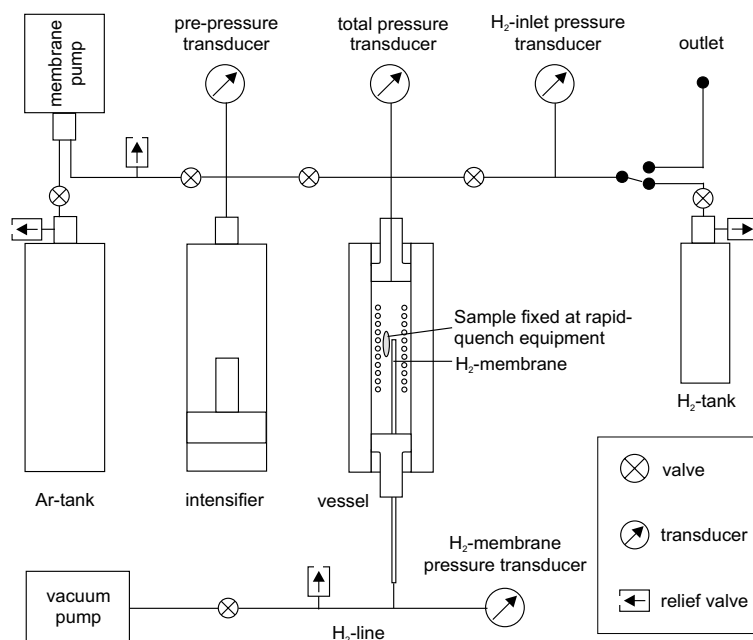
Figure 1.1 Diagram of the rapid-quench-H_2-membrane IHPV assemblage.

allows one to perform such experiments, and hence, to investigate the influence of p, T, fO_2, and aH_2O on phase relationships and physicochemical properties of basaltic systems. Applications for the determination of water solubilities and phase relationships are presented.

1.2. The Vessel

Schematic illustrations of the complete high-pressure equipment, the vessel, furnace, and the rapid-quench setup are shown in Figures 1.1 and 1.2.

The double-end designed vessel body consists of two outer cylindrical Böhler W300 Isobloc® tool-steel parts shrinked on each other and of an inner Inconel 718®-steel cylinder. In operation mode the vessel is vertically mounted. For easy insertion of furnace and sample holder the vessel can be turned around into a horizontal position. Internal threads (heat treated to 60 HRC) and closure nuts (45 HRC) are installed at both ends of the autoclave. The working space of the vessel is a cylinder of 45 mm i.d. and a length of 350 mm.

The maximum operating pressure is 1 GPa. The upper closure head of the IHPV is attached to the furnace (Fig. 1.3) and contains two ports for power supply of the furnace. The lower closure head holds the rapid-quench-H_2-membrane device (Fig. 1.4) and contains overall four
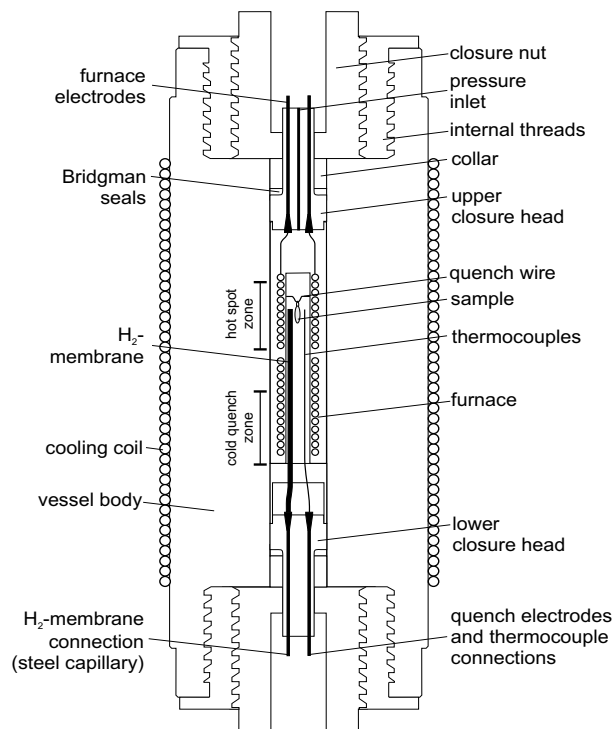
Figure 1.2 Schematic cross section of the IHPV equipped with rapid-quench-H_2-membrane device.

ports for S-type thermocouples (Pt-PtRh$_{10}$), power lead for rapid-quench function and steel tubing which is connected to the H$_2$-membrane inside the IHPV and the H$_2$-membrane transducer (Fig. 1.1, 1.2, 1.4). To avoid embrittlement problems due to hydrogen permeation in steel, the closure heads were made of CuBe2 beryllium bronze (40 HRC). Bridgman type pressure packings consisting of bronze-Teflon-copper-bronze-rings are used for sealing the closure heads.

1.3. The Furnace

The vertically operating resistance furnace apparatus (Fig. 1.3) is based on the double wire element furnaces for IHPV described by Holloway (1971), Holloway and Wood (1988), and Holloway et al. (1992). The internal ceramic tube (99.9% Al$_2$O$_3$, i.d. 22 mm) is wrapped with two molybdenum windings (o.d. 0.5 mm) which are connected to electrical leads made of steel cones insulated by Teflon heat shrink tubing. Ground connection of the windings is done through the vessel body itself. Separate controlled heating zones (using an Eurotherm 906 EPC controller) combined with radially thermal insulation made of steel foil, mullite, and quartz wool yield stable isothermal conditions in a large volume (5 °C along 50 mm length and 22 mm diameter in the temperature range 900 – 1250 °C up to 500 MPa) and a temperature oscillation 3 °C. Thermal insulation between the hot spot zone and the closure head, steel cones, and electrical leads is ensured by a ceramic-, a pyrophyllite-, and a Teflon plate. The position of the capsules is determined by the sample holder (see below) and lies approximately 15 mm above the boundary between the two windings. The typical heating rate is about 30°C/min with a power distribution of about 560 W for the lower and 200 W for the upper winding (at 200 MPa and 1250 °C).

1.4. The Rapid-Quench Device

General features of rapid-quench devices used in IHPV to avoid non-equilibrium quench effects such as the formation of quench crystals from the melt or overgrowth of existing phases were described in detail by Roux and Lefevre (1992) and Holloway et al. (1992).
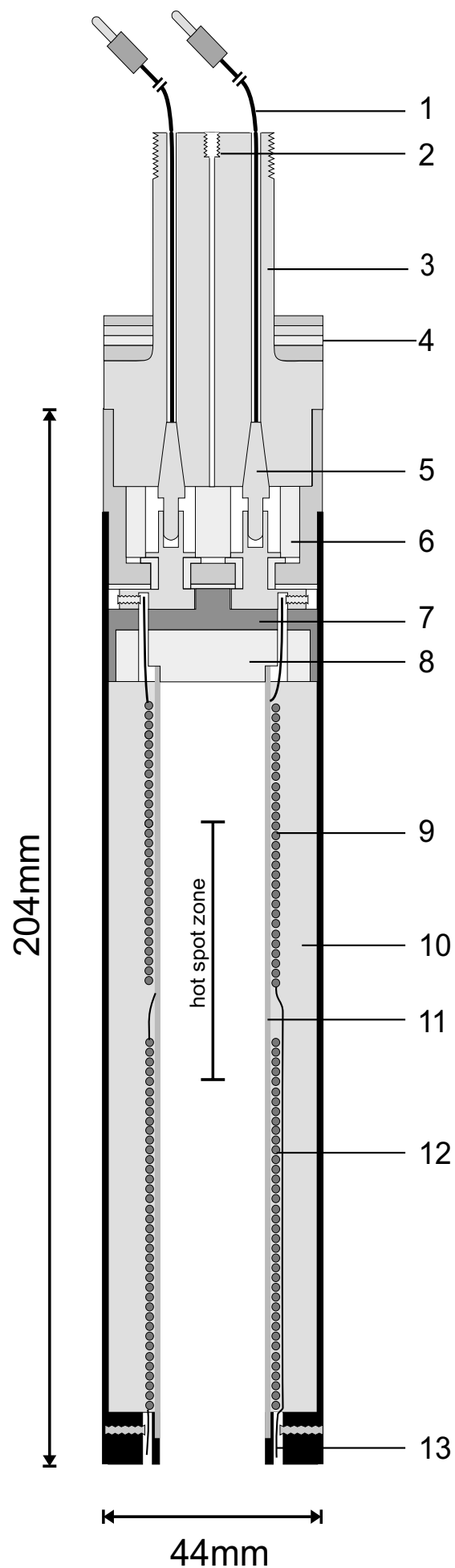
Figure 1.3 Schematic illustration of the furnace: (1) furnace electrodes; (2) pressure inlet; (3) closure head; (4) Bridgman seal; (5) steel cone; (6) Teflon insulation; (7) pyrophyllite insulation; (8) ceramic plate; (9) upper molybdenum winding; (10) mullite quartz steel-foil insulation; (11) ceramic tube; (12) lower molybdenum winding; (13) ground connection.
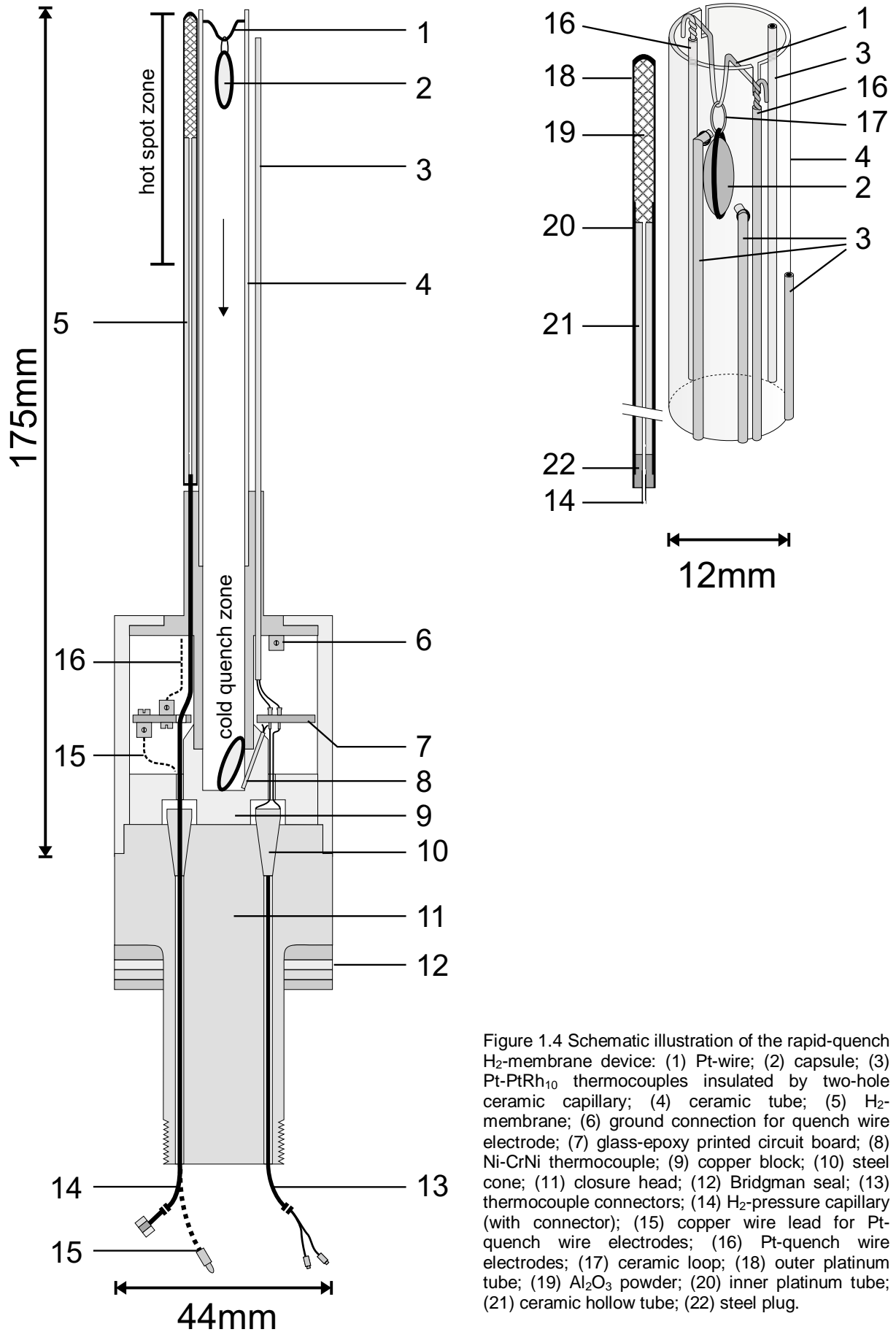
Figure 1.4 Schematic illustration of the rapid-quench H_2-membrane device: (1) Pt-wire; (2) capsule; (3) Pt-PtRh$_{10}$ thermocouples insulated by two-hole ceramic capillary; (4) ceramic tube; (5) H_2-membrane; (6) ground connection for quench wire electrode; (7) glass-epoxy printed circuit board; (8) Ni-CrNi thermocouple; (9) copper block; (10) steel cone; (11) closure head; (12) Bridgman seal; (13) thermocouple connectors; (14) H_2-pressure capillary (with connector); (15) copper wire lead for Pt-quench wire electrodes; (16) Pt-quench wire electrodes; (17) ceramic loop; (18) outer platinum tube; (19) Al_2O_3 powder; (20) inner platinum tube; (21) ceramic hollow tube; (22) steel plug.

Some new design features of the experimental setup are presented in this study (Fig. 1.4, 1.5). A general description of the rapid-quench device can be summarized as follows: The sample is fixed to a Pt-wire in the hot spot of the furnace and is quenched by fusing the Pt-wire electrically. The sample falls on a *copper block unit* with high thermal conductivity fixed on the lower closure head which is in direct contact to the water-cooled vessel body.

A K-type thermocouple placed on the bottom of the copper block unit records *continuously* the temperature of the cold quench area (20 - 25 °C for typical experiments up to 1250 °C and 200 MPa). This allows to check the successful rapid quench of the sample due to temperature increase in the cold zone when the capsule drops. All temperatures and pressures of the IHPV are logged automatically by a *LabView computer monitoring* system. Thus, a premature drop of the capsule, temperature oscillations or other temporally occurring failures can be detected. Four unsheathed S-type thermocouples are placed in the hot spot zone. Two of them, connected to the Eurotherm unit, are used to control the power supply of the two furnace windings. Two additional thermocouples are inserted into the ceramic tube (ceramic tube has been drilled) and are positioned about 2 mm from the capsules to determine the exact temperature of the samples hanging inside the ceramic tube.

Thin enameled copper wires (o.d. 0.15 mm) pass through the pressure ports to allow the connection between the thermocouples wires (in the vessel) and the Eurotherm controller. Only two pressure ports are available for the copper wires which are easily damaged especially when pressurizing the vessel. To protect these wires, small slits are made along the
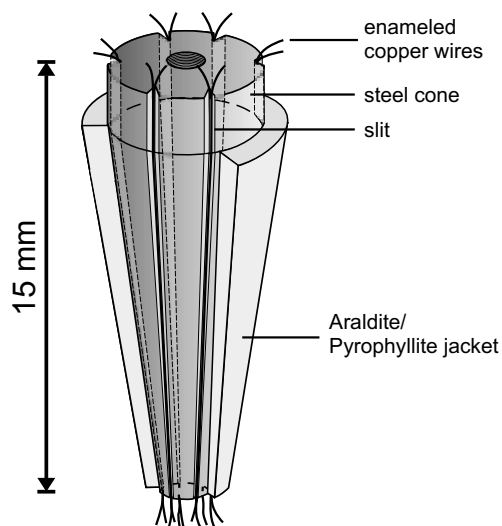
Figure 1.5 Steel cone with slits containing enameled copper wires which are connected to the thermocouples.

7

steel cones (angle 7.5°; Fig. 1.5) in which the enameled copper wires are fixed with an Araldite/Pyrophyllite mixture (Roux, pers.com.). The steel cones are sealed by a second Araldite/Pyrophyllite jacket. Thermocouple pressure ports made in this way show high reliability and durability. More than 150 experiments under conditions up to 500 MPa and 1250 °C were performed with the same cones.

The cooling rate of rhyolite melts quenched with the device described above has been estimated by Benne (2000, unpublished diploma thesis) using the geospeedometer of Zhang et al. (2000). Results show a quench rate of 150 °C/s with a factor of two uncertainty. Holloway et al. (1992) calculated a theoretical quench rate of about 500 °C/s for a similar internally heated rapid quench vessel whereas Roux and Lefevre (1992) estimated that the samples cool to room temperature in less than 1 minute. However, quench rates depend on the size of the capsule, heat conductivity of the sample, pressure, and run temperature. Our experimental design allows one to quench water-saturated MORB liquids containing 9.38 wt% H_2O (see below) from 500 MPa and 1200 °C to a homogenous, crystal- and bubble- free glass.

1.5. H_2-Membrane Design

Only a few H_2-membranes for IHPV have been described in detail (e.g., Piwinskii et al., 1973; Scaillet et al., 1992). Most of them were made of AgPd alloys because of its high permeability. Despite the lower permeability of hydrogen through Pt when compared to AgPd-alloys (e.g., Chou, 1986), platinum was chosen as permeable metal for the membrane. The use of a Pt-membrane is justified by the high experimental temperatures needed for investigations of basaltic systems (melting point of Pt at 1 atm: 1772 °C; melting point of $Ag_{40}Pd_{60}$ at 1 atm and 1330 °C). It is emphasized that the setup described below can only be used as a hydrogen sensor because of the low volume of the membrane compared to the vessel. The small space that is available for a H_2-membrane near to a rapid-quench setup (Fig. 1.4) requires a relatively small-sized membrane configuration. Therefore, controlling the large free volume of the IHPV (190 cm^3) via the membrane as an H_2-reservoir (3.53 cm^3) is

difficult due to the long equilibration time between the Pt-membrane and the vessel (Hewitt, 1977; Scaillet et al., 1992; Schmidt et al., 1995).

The H_2-membrane is attached to the rapid-quench sample holder (Fig. 1.4). It is composed of an outer Pt tube (i.d. 2.8 mm, o.d. 3.2 mm and 90 mm length) which is welded at its top and filled with Al_2O_3 powder (grain size 100 - 180 μm) along the last 30 mm (part of the membrane located in the hot spot zone). In the lower part a second Pt tube (o.d. 2.7 mm, i.d. 2.5 mm) containing a ceramic hollow tube (i.d. 0.5 mm) followed by a steel plug is inserted in the outer Pt tube. A steel capillary connecting the membrane assembly to the H_2-pressure transducer (Fig. 1.1) is inserted inside the lower part of the steel plug. Inner and outer platinum tube, steel plug, and steel capillary are brazed at their bottom ends.

First attempts to measure pH_2 in the hot spot zone were made using porous AlSiMag rods (described by Scaillet et al., 1992 and Schmidt et al., 1995) instead of Al_2O_3 powder. But high run temperatures of more than 1000 °C at 200 MPa lead to a fast recrystallization of AlSiMag which completely hampered the diffusion of hydrogen through the membrane into the H_2-line. As a result of the failure of these AlSiMag rods at high temperatures it could be deduced that the ceramic hollow tube which is located in the lower part of the membrane is impermeable to hydrogen. Thus, the H_2-diffusing zone is restricted to the porous Al_2O_3 powder filled membrane section lying in the hot spot zone near the samples.

1.6. Experimental Procedure and Achievement of Equilibrium

Experiments with the described setup were performed at pressures of up to 500 MPa from 900 °C to 1200 °C. After loading the IHPV and flushing with pure hydrogen, the vessel is first charged with hydrogen up to the initial pH_2. After isolation from the H_2-reservoir, the vessel is loaded with argon until about 50 % of the final pressure (depending on the run temperature) is reached. The vessel is then completely isolated from the Ar-pressure line. The H_2-line is air-evacuated (Scaillet et al., 1992) before raising the temperature to the desired value. At the end of the experiment the quench wire is fused electrically and the samples drop down to the cold quench area. In experiments with duration shorter than the time needed to

attain hydrogen equilibrium between the vessel and the H_2-membrane, the H_2-equilibrated samples are quenched and stay on the bottom of the sample holder (Fig. 1.4) under pressure (in the cold area of the vessel) until equilibrium is reached for exact pH_2 measurement in the membrane. Due to the low temperature in the cold quench zone (20 – 25 °C), which is far below the glass transition temperature, no reaction takes place in the experimental charge.

To test the reliability of the H_2-membrane response, several experiments using the solid redox sensor technique after Taylor et al. (1992) and capsules charged with solid oxygen buffer assemblages (Ni-NiO and Co-CoO) have been carried out. The intrinsic fH_2 buffering capacity in IHPV´s used at Hannover has been measured with Ni-Pd solid sensors (Taylor et al., 1992) and is equivalent to the MnO-Mn_3O_4 solid oxygen buffer in the temperature range 900 °C - 1200 °C at 200 MPa and 500 MPa (identical values for IHPV were found by Webster et al. (1999). Solid redox sensor measurements in the IHPV equipped with the H_2-membrane have been carried out at 1000 °C and 1150 °C at 200 MPa but were not successful. The adjusted fH_2 was slightly above the Ni-NiO buffer (using Ni-Pd sensor) and at the QFM buffer (Co-Pd sensor), respectively. Analyses of the resulting sensor alloys as well as of the used capsule material ($Au_{80}Pd_{20}$ and Pt) showed that the reactive metal component was almost completely lost to the capsule wall despite placing the sensor mixtures in an inert ZrO_2 jacket (probably due to the high run temperatures at low oxygen fugacities).

Further experiments were carried out to verify the pH_2 values measured by the H_2-membrane (Tab. 1.1). Charges (25 mg) of NiO and Co (with an excess of H_2O) were sealed separately in

Table 1.1 Experimental results for the reaction $Co + H_2O = CoO + H_2$
and $NiO + H_2 = Ni + H_2O$.

run	T [°C]	duration [h]	p_{total} [MPa]	pH_2 [bar]	log fO_2 [bar]	Δ QFM [bar]	reactants	products
145a	1000	82	207	18.68	-10.77	+0.01	Co	Co.CoO
145b	1000	82	207	18.68	-10.77	+0.01	NiO	Ni. (NiO)
128a	1150	79	205.7	20.50	-8.60	+0.12	Co	(Co). CoO
128b	1150	79	205.7	20.50	-8.60	+0.12	NiO	Ni. (NiO)
128c	1150	5*	205.7	20.50	-8.60	+0.12	NiO	Ni. (NiO)

* charge quenched after 5 h to compare results with 128b

phases in parentheses have been identified qualitatively

10

$Au_{80}Pd_{20}$ capsules and placed inside the rapid-quench-H_2-membrane device. Two capsules were heated at 1000 °C and 207 MPa (run 145) and three capsules at 1150 °C and 205.7 MPa (run 128). Following the experimental procedure described above, the vessel was loaded with the calculated pH_2 corresponding to the QFM solid oxygen buffer. Results in Table 1.1 show that NiO has been reduced to Ni and Co has been oxidized to CoO at both temperatures. This indicates that the measured pH_2 corresponds roughly to the QFM buffer because of the approach of both, the Ni-NiO and Co-CoO buffer assemblages towards the QFM buffer lying between the Ni-NiO and Co-CoO buffer curve.

A method to check the validity of performed pH_2-measurements in IHPV has been used
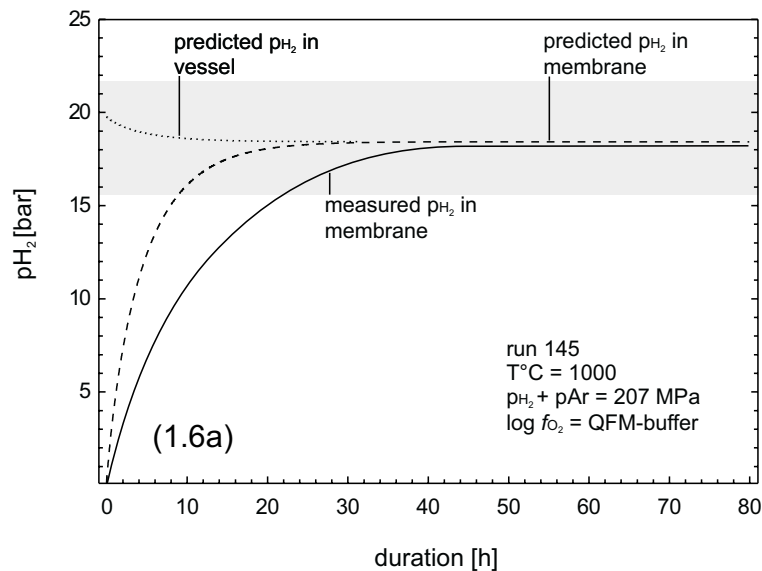
Figure 1.6a Predicted and measured pH_2 response of the H_2-sensor membrane at 1000 °C. Grey zone marks the QFM solid oxygen buffer zone ± 0.15 log units. Note that pH_2 is constant after reaching osmotic hydrogen equilibrium between membrane and vessel.
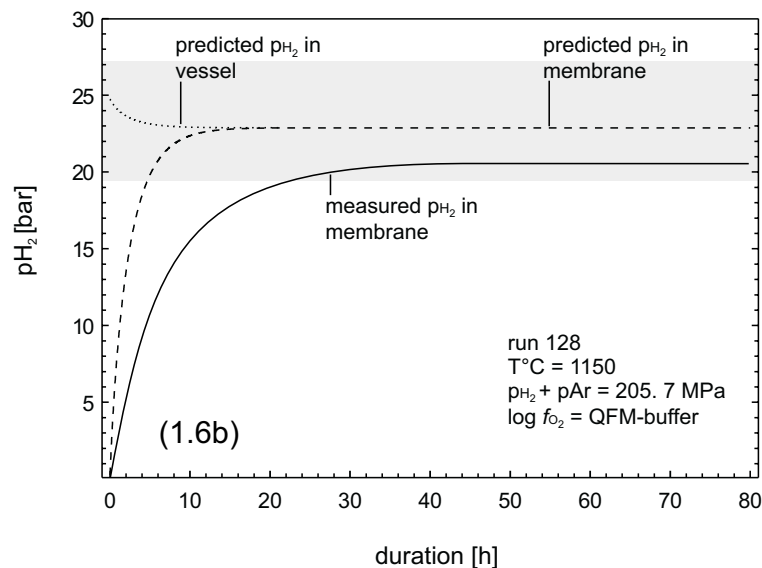
Figure 1.6b Predicted and measured pH_2 response of the H_2-sensor membrane 1150 °C. For detailed comments see Figure 1.6a.

successfully by Scaillet et al. (1992). The theoretical H_2-mass transfer from the vessel through H_2-membranes was calculated and compared with the measured membrane response. Results of Scaillet et al. (1992) showed a good agreement between the predicted and measured evolution of pH_2 in IHPV using Pt and $Ag_{40}Pd_{60}$ membranes at 400 MPa and 700 - 750 °C. Similar calculations to model the mass transfer of hydrogen have been done for experiments no. 145 and 128 (Tab. 1.1, Fig. 1.6a, b). The calculation procedures have been described in detail by Scaillet et al. (1992) using the equation of Harvie et al. (1980; see appendix). The main assumptions made in this calculation procedure can be summarized as follows: 1. The calculation follows an iterative procedure where $f_{H_2}^i$ (membrane or capsule) is initially zero and $f_{H_2}^e$ (vessel) is the initial fH_2 of the vessel after loading the IHPV with calculated pH_2 and Ar considering the run temperature. Due to the permeation of H_2 through the membrane during Dt, $f_{H_2}^i$ increases whereas $f_{H_2}^e$ decreases until equilibrium is reached. 2. The intrinsic oxygen buffer capacity of the vessel is neglected (pH_2 for MnO-Mn_3O_4 buffer conditions at relevant p-T conditions is < 1 bar, see above). 3. Ideal mixing of H_2 and Ar is assumed. 4. The run temperature in the hot spot zone is believed to be the uniform temperature in the free vessel volume. The predicted and measured evolutions of pH_2 at 1000 °C and 1150 °C plotted in figures 1.6a and 1.6b are in good agreement and support the validity of the results obtained from experiments using the Ni-NiO and Co-CoO buffer assemblage.

Figures 1.6a, b can also be used to analyze the possible hydrogen loss by diffusion of hydrogen through the vessel walls in long duration experiments. In contrast to observations made by Scaillet et al. (1992), no decrease of pH_2 in the vessel after osmotic equilibrium between vessel and membrane could be detected (e.g., at 1150 °C pH_2 is identical after 40 and 80 h runtime; Fig. 1.6b). This is confirmed using calculations based on the equation of Harvie et al. (1980; k for Inconel® 718 from Robertson, 1972 in Gunter et al., 1987) which shows that only 6.9×10^{-7} mol H_2 (in 80 h assuming a uniform temperature of the vessel body of 100 °C and a pH_2 of 20.5 bar in the vessel, which corresponds to QFM buffer conditions at 205.7 MPa and 1150 °C run temperature) will be lost through the vessel walls. This minor pH_2

decrease of about 2×10^{-4} bar cannot be detected. A possible explanation for the decrease of pH_2 observed by Scaillet et al. (1992) is that hydrogen escaped through the sheathed thermocouples which were used in their setup.

1.7. Applications

1.7.1. Determination of Water Solubility in Basaltic Liquids

Water solubility determinations have been carried out at intrinsic buffered fO_2 conditions (MnO-Mn$_3$O$_4$ buffer, see above) and at fO_2 corresponding to the QFM buffer to investigate the influence of oxygen fugacity on water solubility in a primitive MORB composition (Tab. 1.2). A powder (size 100 - 200 µm) of synthetic dry MORB glass (composition B1, Tab. 1.3) was used for the solubility experiments.

Charges of about 70 mg powder with an excess of H_2O (Tab. 1.2) were sealed in Au$_{80}$Pd$_{20}$ capsules (Kawamoto and Hirose, 1994). A significant problem for phase equilibrium crystallization experiments in basaltic systems is the loss of iron to the sample container (e.g., Ford, 1978; Grove, 1981; Johannes and Bode, 1978; Ratajeski and Sisson, 1999). It can be shown that there is no iron loss to the Au$_{80}$Pd$_{20}$ capsule material at oxidizing conditions

Table 1.2. Experimental results for water solubility in MORB at 1200 °C.

	MnO-Mn$_3$O$_4$*						QFM†		
run	125	25	24	23	27	26	121	122	126
wt basalt powder [mg]	74.33	80.19	59.88	72.88	63.88	65.66	87.44	69.44	79.48
H$_2$O loaded [ml]	2.69	4.38	6.66	9.09	6.98	11.58	3.24	3.74	7.08
H$_2$O [wt%] in charge	3.49	5.18	10.01	11.09	9.85	14.99	3.57	5.11	8.18
wt charge before experiment [mg]	623.85	697.69	688.40	1045.81	676.67	702.82	646.02	536.73	669.45
wt charge after experiment [mg]‡	623.88	697.73	688.42	1045.84	676.69	702.86	646.12	536.85	669.53
duration [h]	1.5	24	20	24	22	20	1.5	1.5	1.5
P$_{total}$ [MPa]	50.5	53.2	102.3	202.1	304.3	500.9	55.4	101.9	203.3
P$_{H_2}$ [bar]*, †	0.05	0.06	0.10	0.17	0.22	0.30	10.20	16.10	26.40
log fO_2 [bar]§	-3.86	-3.86	-3.83	-3.78	-3.73	-3.63	-8.37	-8.29	-8.18
Δ QFM [bar]	+ 4.362	+ 4.361	+ 4.357	+ 4.344	+ 4.331	+ 4.307	- 0.140	- 0.103	+ 0.064
H O [wt%] in glass ‖	2.20 (0.08)	2.23 (0.09)	3.32 (0.09)	4.8 (0.07)	6.27 (0.09)	9.38 (0.06)	2.23 (0.04)	3.05 (0.05)	4.46 (0.02)
duplicate	2.28 (0.06)	-	-	-	-	-	2.14 (0.04)	3.18 (0.04)	-

* intrinsic buffering capacity of used IHPV corresponds to the MnO-Mn O solid oxygen buffer (measured with solid oxygen sensor method of Taylor et al., 1992)
† P$_{H_2}$ was monitored using H$_2$-membrane
‡ weight gain of the capsules after experiments is caused by small adherent pieces of Pt quench wire
§ based on equation for MnO-Mn$_3$O$_4$ (Chou 1978) and QFM (Schwab and Küstner 1981) buffer curve
‖ uncertainty from Karl-Fischer-Titration given in parentheses (0,02µg/s) ; for further comments see text

(Berndt et al., 2000). For the experiments at reducing conditions, the capsules were presaturated in iron at fO$_2$ conditions similar to the desired redox conditions in solubility experiments. Presaturation was performed for 3 days at 1200 °C in an 1 atm gas mixing furnace (H$_2$/H$_2$O) and the capsules were placed in a ceramic crucible containing a MORB glass (with composition given above). The capsules were subsequently extracted from the surrounding glass by placing them in HF. Microprobe analysis of glasses obtained by hydration runs at 1200 °C and 203 MPa (aH$_2$O = 1; fO$_2$ corresponding to the QFM buffer) in capsules treated by this method showed that iron loss is small (about 3 wt% relative). The run duration at reducing conditions was short (1.5 h) to minimize iron loss. By using a powder of maximal 200 µm grain size, it can be shown that a duration of 1.5 h is long enough to attain equilibrium distribution of water at 1200 °C and 200 MPa (assuming $2\sqrt{Dt}$ and D$_{H_2O}$ values in basaltic melts with 0.2 wt% H$_2$O from Zhang and Stolper, 1991). Additionally, experiments no. 25 (24 h runtime) and 125 (1.5 h runtime) at MnO-Mn$_3$O$_4$ buffer conditions show similar results for water solubility and are evidence for achievement of equilibrium distribution of water in the glasses. The experimental products were crystal- and bubble- free glasses and the water contents were analyzed by Karl-Fischer-Titration (KFT; Behrens, 1995; Holtz et al., 1995; Behrens et al., 1996). Water solubility data results at oxidizing conditions are in good agreement with previous data of Hamilton et al. (1964) in the p-T range 50 - 400 MPa (Tab. 1.2; Fig. 1.7a). Our results show that Hamilton et al. (1964) probably underestimated the water solubility at higher pressures due to their analytical method (weight loss at 110 °C, see discussion in Holtz et al., 1995). The evolution of water solubility as a function of pressure (MPa) in the range 100 - 500 MPa at 1200 °C is almost linear and can be modeled by the following equation: $y = 0.01515\,x + 1.8$ where y is the water content of the melt and x is the pressure in MPa. The data obtained up to 200 MPa at MnO-Mn$_3$O$_4$ and QFM redox conditions show that water solubility is slightly higher at high fO$_2$ (MnO-Mn$_3$O$_4$) than at the QFM buffer (Tab. 1.2; Fig. 1.7b). Although the absolute differences are low, they are not considered to be an artifact. Water contents determined by KFT show a good reliability

especially in the range 2 - 8 wt% water (Behrens, 1995) and the precision of the KFT analyses are below $\pm$ 0.15 wt% H_2O absolute (for a total measured amount of H_2O of 500 – 1000 µg). The uncertainties given in Table 1.2 are always below this value and the results from duplicate analyses are also within this range. Due to the low viscosity of hydrous basaltic liquids, the glasses are bubble free and the analysis cannot be influenced by the presence of water in bubbles. At 200 MPa the uncertainty of the determination is lower than the water solubility difference between high and low fO_2. There are two possible explanations for the
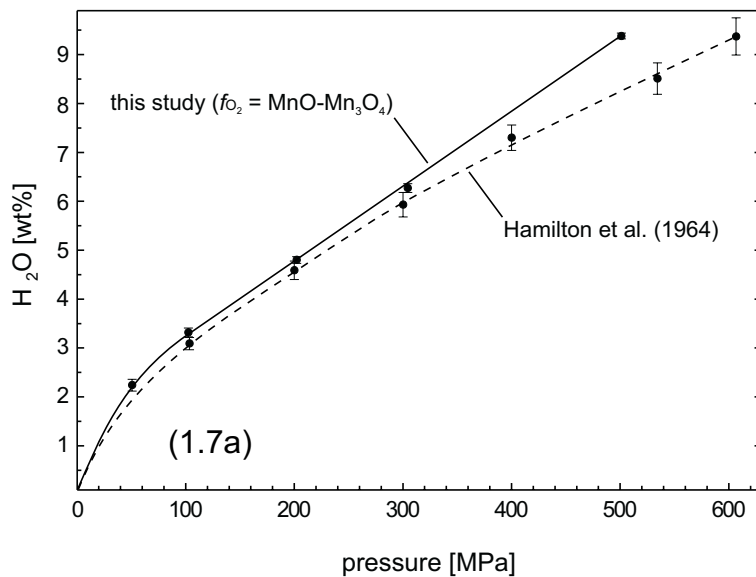
Figure 1.7a Water solubilities for the MORB system at 1200 °C between 50 and 500 MPa and redox conditions corresponding to the MnO-Mn_3O_4 buffer compared with solubility data of Hamilton et al. (1964) for Columbia River basalt.
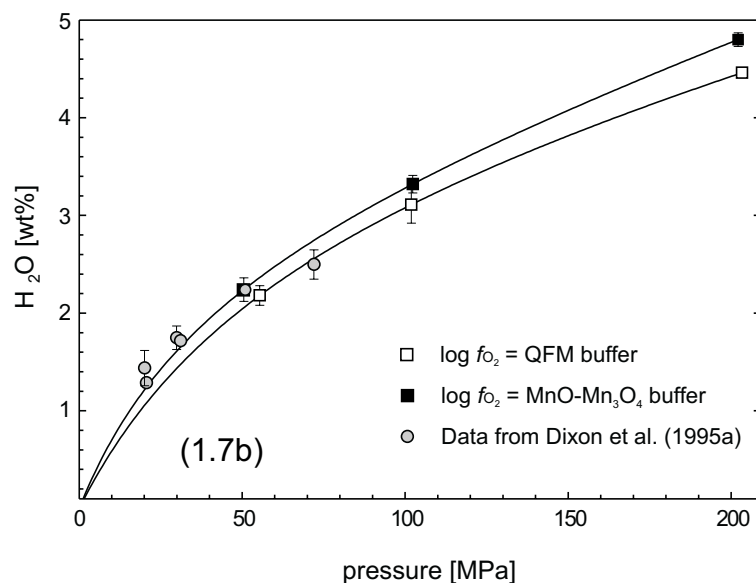
Figure 1.7b Water solubilities for the MORB system at 1200 °C in the pressure range 50 - 200 MPa at fO_2 corresponding to the MnO-Mn_3O_4 buffer and QFM buffer and water solubility data of Dixon and Stolper (1995) for more differentiated MORB composition than used in this study.

effect of fO_2 on water solubility: 1. The water activity is reduced by the higher pH_2 at QFM redox conditions when compared to low pH_2 (<1 bar) at oxidizing conditions. However, it has been shown by Schmidt et al. (1999) that such a low variation in pH_2 (less than 30 bar, see Tab. 1.2) does not influence significantly the water solubility. 2. The Fe^{2+}/Fe^{3+} ratio in the melt is responsible for the different water solubility. Melts at higher fO_2 contain more Fe^{3+} and are therefore more polymerized at dry conditions. The dissolution of water involves reaction with bridging oxygens. Because of the higher Fe^{3+} content in melts at oxidizing redox conditions (higher amount of bridging oxygens) it can be expected that more water is incorporated at such high fO_2 conditions. In addition it has been shown that water solubility increases with increasing polymerization of the anhydrous composition (from basalt to andesite, Ohlhorst et al., 2000). Our water solubility results can also be compared with those of Dixon et al. (1995; Fig. 1.7b). Depending on their calculation method, the fO_2 calculated by Dixon et al. (1995) is between QFM and QFM+2. Our results are in general good agreement with those of Dixon et al. (1995), but it is difficult to extract information on the effect of fO_2 from the study of Dixon et al. (1995) because of the relatively high uncertainty on fO_2 determination. Furthermore, the composition is slightly different from that used in this study.

1.7.2. Determination of Phase Relations in Basaltic Systems

The experimental setup described above has been used to understand kinetic controls on crystallization in iron-bearing basaltic systems. In most high pressure experiments designed to investigate phase relationships, the starting material is a glass synthesized at 1 atm in air. Such starting glasses have low Fe^{2+}/Fe^{3+} ratio corresponding to a log fO_2 = -0.68. The fO_2 range adjusted in the high pressure experiments is 10 to 15 log units below this value. Consequently the Fe^{2+}/Fe^{3+} ratio changes strongly in the first minutes of experiments. Because crystallization of basaltic systems is fast, the osmotic hydrogen equilibrium between vessel and capsule needs to be reached directly after heating up. If this condition is not fulfilled, it can be expected that the individual crystals will not be homogenous (the core of the minerals crystallize at higher fO_2) which may influence the interpretation of the experimental results.

16

The best method to attain rapid osmotic H_2-equilibrium is to pressurize the vessel with a mixture of Ar and H_2 and to use the membrane as a low-volume hydrogen sensor (which corresponds to the technique described in this study) because the desired fH_2 in the vessel is reached immediately after heating up (in contrast to other techniques where the membrane is used as H_2-reservoir). However, even if fH_2 is reached immediately in the vessel, the Fe^{2+}/Fe^{3+} ratio in the starting glass is not necessarily that corresponding to the desired fO_2.

We performed a crystallization experiment using a hydrous MORB glass powder (see composition in Tab. 1.3) synthesized at $\log fO_2 = MnO-Mn_3O_4$ buffer, at 1200 °C, 200 MPa, and $aH_2O = 1$ (with approx. 4.8 wt% H_2O). A powder (size 100 - 200 µm) of this glass was sealed in a Fe-presaturated $Au_{80}Pd_{20}$ capsule, and the crystallization experiment was performed at following conditions: 200 MPa, 1000 °C, $\log fO_2 = QFM - 0.1$ for 5 h. Figure 1.8 shows a BSE image of the experimental products composed of plagioclase, olivine, clinopyroxene, glass and oxides. Microprobe analyses of glasses and $Au_{80}Pd_{20}$ capsule materials in experiments conducted under these conditions showed that no significant iron loss occurs.

Table 1.3. Starting material, selected olivine and melt compositions.

SC B1*			Phase	ol rim	ol core	ol small		melt†	
n‡	18	σ	no.§	1	2	3	n‡	2	σ
wt%									
SiO	49.64	0.27		40.17	40.78	39.55		53.67	0.13
TiO_2	0.87	0.05		0.02	0.04	0.04		1.33	0.02
$Al O$	16.07	0.16		0.72	0.02	0.04		18.64	0.31
FeO	8.63	0.07		21.10	15.36	23.24		8.37	0.07
MnO	0.15	0.07		0.24	0.40	0.35		0.22	0.14
MgO	9.77	0.09		37.50	43.29	38.27		4.01	0.12
CaO	12.44	0.16		0.31	0.19	0.28		9.76	0.06
Na_2O	2.28	0.09		0.10	0.00	0.00		3.85	0.07
$K O$	0.08	0.03		0.02	0.00	0.04		0.16	0.03
P_2O_5	0.08	0.05		-	-	-		-	
Total	100.00			100.18	100.08	101.81		100.00	
			X_{Fo}	0.76	0.83	0.75			
Mg#	82.35		Kd ‖	0.316	0.199	0.341	Mg#	50.53	

Experimental conditions: 200 MPa, 1000°C, P_H = 20.5 bar,
$\log fo_2$ = -10.87 (QFM - 0.1) aH_2O=1;
* Starting composition synthesized at 1200 °C and 200 MPa with aH O =1 and
$\log fo_2$ = -3.78 ($MnO-Mn_3O_4$- buffer); † melt analyses are normalized to 100 wt%;
‡ number of analyses; § see Figure 8; ‖ Kd Ol-Melt/Mg-Fe

Large olivine crystals show compositional zonation. The composition of olivine cores (X_{Fo} 0.83, see Tab. 1.3 and Fig. 1.8) is different from that of the rims (X_{Fo} 0.76) and of small, probably later grown, olivines (X_{Fo} 0.75). The Mg#, defined as $X_{Mg}/(X_{Mg} + X_{Fe}^{2+})$, of the basaltic glass is 50.5 (Tab. 1.3). At equilibrium conditions, the $Kd_{Fe-Mg}^{Ol-Melt}$ for basaltic melts with Mg# = 50.5 should be about 0.3 (Ulmer, 1989; Roeder and Emslie, 1970; Toplis and Carroll, 1995). Such a Kd-value is obtained between olivine rims (and small olivines) and the analyzed melt, suggesting equilibrium conditions between these phases. The higher Mg# of the olivine cores is interpreted to result from fast crystallization from the melt before osmotic hydrogen equilibration with the prevailing oxygen fugacity in the vessel is reached. Different fO_2 conditions in the first stages of the experiment are also confirmed by the presence of oxides in olivine cores only. The higher X_{Fo} of the olivine cores is consistent with crystallization under higher fO_2. This higher fO_2 results from the initial Fe^{2+}/Fe^{3+} of the melt which is lower than at equilibrium conditions (see above).

The chemical zoning of the large olivine crystals shows that fH_2 in the charge was not reached
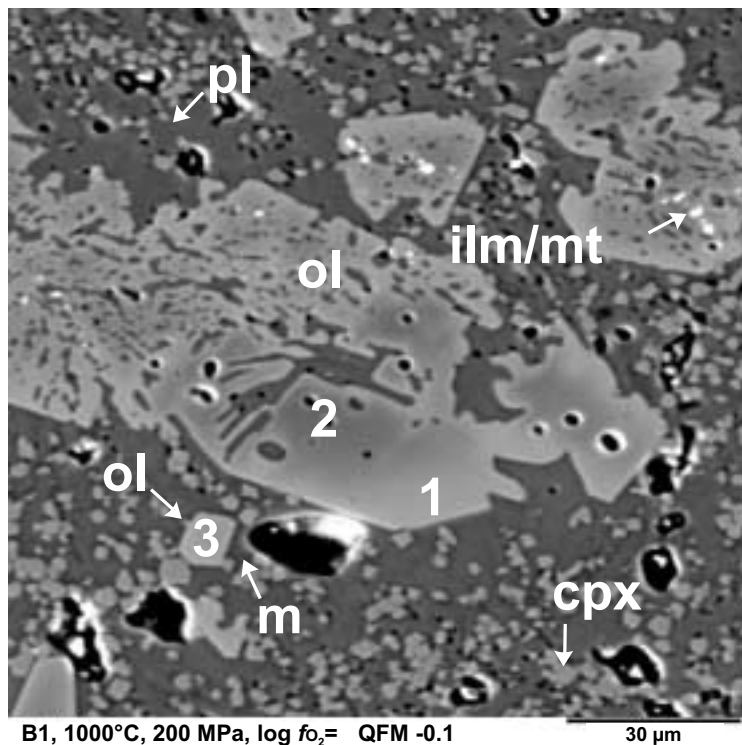
Figure 1.8 BSE picture of MORB crystallization experiment (1000 °C, 200 MPa, = QFM = -0.1 log units, buffer conditions, aH_2O = 1.5 h duration). pl plagioclase, ol olivine, ilm ilmenite, mt magnetite, cpx clinopyroxene, m melt. Numbers indicate olivine analyses in Table 1.3.

B1, 1000°C, 200 MPa, log fo_2= QFM -0.1   30 μm

18

immediately after heating up. This delay is most probably due to the relatively slow permeation of hydrogen through $Au_{80}Pd_{20}$ alloys (the diffusion of hydrogen through a basaltic liquid is probably faster than through the noble metal; Chekhmir et al., 1985). No diffusion data for hydrogen in $Au_{80}Pd_{20}$ alloys for temperatures of 1000 °C are available. For temperatures up to 112 °C, Maestas and Flanagan (1973) and Sakamoto et al. (1982) showed that with decreasing Au content, the diffusion coefficient of hydrogen increases for alloy compositions from $Au_{50}Pd_{50}$ to $Au_{10}Pd_{90}$. Permeation of hydrogen through pure Au and Pd capsules (i.d. 0.28 cm, o.d. 0.32 cm at 1.5 cm length) using the equation of Harvie et al. (1980) shows a different behavior between these two metals: at the experimental conditions described above the osmotic fH_2 equilibrium with Au and Pd capsules is attained after about 1.5 h (1 h 28min; k for Au from Chou, 1986) and a few seconds (6s; k for Pd of Holleck, 1970 in Gunter at al., 1987), respectively. The calculations above show that the use of $Au_{80}Pd_{20}$ capsules to avoid iron loss and to perform experiments up to 1200 °C requires several minutes before osmotic H_2-equilibration is reached. Thus, a starting glass preequilibrated at fO_2 conditions similar to the desired redox conditions has to be used to perform successful phase equilibrium studies and to avoid disequilibrium effects due to slow fH_2 equilibration between capsule and vessel.

1.8. Conclusions

The setup for IHPV described in this study is a new combination of two established experimental techniques: hydrogen sensor membrane to measure fH_2 (e.g., Shaw, 1963; Piwinskii et al., 1973; Scaillet et al., 1992) and rapid-quench-system to avoid crystallization of low viscous melts during quench (Roux and Lefevre, 1992; Holloway et al., 1992). The high temperature membrane setup allows experiments in basaltic compositions to be performed routinely at fO_2 and aH_2O conditions which can be varied accurately in small intervals without being fixed to fO_2 values controlled by solid oxygen buffers (double capsule technique). The experimental setup has been tested in the pressure range 50 - 500 MPa and 1200 °C for more than 80 runs. High temperature experiments in this pressure range could

only be performed with piston cylinder apparatus in which the adjustment of oxygen fugacity is difficult. In addition, the use of IHPV allows the synthesis of large experimental samples. Using a low-volume hydrogen sensor membrane has the main advantage to attain rapidly the desired fH$_2$ in the vessel which is important for phase relation investigations due to the fast crystallization of basaltic systems. Furthermore, the low volume of the sensor membrane does not influence the fH$_2$ in the vessel. When compared with AgPd-membranes, the osmotic equilibration time of Pt-membrane (necessary for high run temperatures) is longer. However, this is not a problem with our setup, because of the possibility to quench and store the sample in the cold part of the IHPV (copper block) until osmotic hydrogen equilibrium is reached.

2. Influence of H$_2$O on Differentiation of MORB at 200 MPa and High Oxygen Fugacity (MnO-Mn$_3$O$_4$ -Buffer Conditions)

2.1. Introduction

In the last decades, many experimental studies have been focused on the investigation of phase relations in natural basaltic systems for a better understanding of the differentiation mechanisms under crustal pressure and temperature conditions. Most of these experiments have been carried out at a pressure of 1 atm (e.g., Osborn, 1959; Grove and Bryan, 1983; Grove and Baker, 1984; Thy and Lofgren, 1994; Toplis and Carroll, 1995; Toplis and Carroll, 1996; Juster et al., 1989; Snyder et al., 1993), assuming that the small pressure difference between shallow magma chambers and the surface does not influence significantly the results and implications drawn from these studies. In other words it was considered that the low volatile content of basaltic melts (which can only be incorporated in melts at high pressure) has little influence on phase relations in MORB systems. One of the benefits of these 1 atm studies was to evaluate the role of fO$_2$ which greatly effects the Fe-Ti oxide stabilities and the related iron / silica enrichment of the melt. Concerning the role of volatiles, especially H$_2$O, the broadly absence of amphibole in tholeiitic plutonic complexes (e.g., Skaergaard, Kigplait,

Pleasant Bay, typical oceanic crust) is believed to be an evidence for very low water activities during fractionation of these melts.

Recent studies on water contents in basalts from Kovalenko et al. (2000) showed that even primitive MORB have an average H$_2$O content of 0.31 wt%. Sobolev and Chaussidon (1996) have reported water contents for primitive MORB up to 0.51 wt%. Assuming an initial water content for a primitive MORB liquid of 0.5 wt% at a pressure corresponding to shallow level, the crystallization of 60 wt% of water-free solid phases results in an increase of water activity (aH$_2$O) up to about 0.23 (calculated after Burnham, 1979) for MORB at 1100 °C and 100 MPa; see below). Thus, it can be expected that the water activity of MORB liquids increases to values which influence phase relations in these systems (especially in later stages of fractionation) even if the stability field of amphibole may not have been reached.

Very little experimental data are available to understand the effect of aH$_2$O on the differentiation trends of primitive MORB´s at moderate pressure. To our knowledge, only Spulber and Rutherford (1983) performed experiments using a primitive MORB from Galapagos Spreading Center to assess the origin of plagiogranites in oceanic ridges, but aH$_2$O has not been varied systematically. Experimental investigations have been carried out in more alkali-rich compositions. The comparison of results from melting and crystallization experiments of Holloway and Burnham (1972) on the 1921 Kilauea tholeiite at an aH$_2$O ~ 0.6 with those of Yoder and Tilley (1962) and Helz (1973, 1976) at water-saturated conditions show that water influences phase relations and that the occurrence amphibole influences the differentiation processes from andesite to rhyolite residual melts. Sisson and Grove (1993a) and Sisson and Grove (1993b) investigated experimentally phase relations in calc-alkaline systems at water-saturated conditions and Kawamoto (1996) carried out melting experiments at aH$_2$O $\leq$ 1 in similar systems. These authors emphasized the dramatic role of water and pointed out the absence of amphibole in these systems not necessarily mean that dry conditions are prevailing.

The lack of experiments in basaltic systems at moderate pressure (100 – 500 MPa) in the presence of volatiles is due to experimental problems. The crystallization of quench products is a serious problem when performing experiments with low-viscosity basaltic compositions and often hampered the interpretation of results from former phase equilibrium studies (e.g., (Helz, 1973; Helz, 1976; Holloway and Burnham, 1972; Hamilton et al., 1964). In this study, experiments were carried out in internally heated pressure vessels (IHPV) using a rapid-quench sample holder to avoid the formation of quench crystals during cooling the experimental charge (Roux and Lefevre, 1992; Holloway et al., 1992; see chapter 1). The study was planned to provide information on the influence of aH₂O on phase relations in a primitive MORB system at 200 MPa and fO_2 corresponding to the MnO-Mn₃O₄ buffer. We performed crystallization experiments in the temperature range 1150 - 950 °C using both, a primitive and a fractionated synthetic 10-component MORB glass. For each composition the phase relations and phase compositions have been determined for four different bulk water contents (ranging from 4.70 down to 0.74 wt% H₂O). The results are used to improve our knowledge on the influence of water on liquid lines of descent in a primitive MORB and on crystallization processes in basaltic systems.

2.2. Experimental Techniques

2.2.1. Apparatus

All experiments were performed in a large volume, vertically mounted IHPV with pure Ar as pressure medium. A detailed description of the apparatus is given in chapter 1. Total pressure was recorded continuously with a Burster© Typ 8221 transducer (relative error < 0.5 %). Different transducers from multiple IHPV were calibrated against each other and showed no discrepancy. At 200 MPa, pressure uncertainty is about 1 MPa. A doubly wound resistance furnace (Holloway, 1971; Holloway and Wood, 1988; Holloway et al., 1992) controlled by an Eurotherm 906 EPC unit allows a large isothermal volume in the hot spot zone (± 5 °C along 50 mm length and 22 mm diameter). Temperature oscillation is below 3 °C. Temperatures

were read with four unsheathed S-type (Pt-PtRh$_{10}$) thermocouples. Two of them are connected to the Eurotherm unit for controlling the power supply of the furnace. Two additional thermocouples are positioned about 2 mm away from the capsules for an exact determination of the sample temperature. To avoid the formation of quench crystals during cooling the experimental charge, a rapid-quench system was used (Roux and Lefevre, 1992; Holloway et al., 1992; see chapter 1) in which up to six capsules are fixed to a Pt-wire in the hot zone of the furnace. By fusing the Pt-wire electrically, the capsules drop onto a copper block placed at the bottom of the sample holder (the temperature in this part of the vessel is about 25 °C). Quench rates achieved using this method completely avoid the formation of quench crystals. Basaltic glasses containing high water contents (up to 9.4 wt% H$_2$O) could be quenched perfectly with this technique (see chapter 1). Intrinsic fO$_2$ of the IHPV has been measured at four temperatures (900 – 1200 °C) using the Ni-Pd solid redox sensor technique after Taylor et al. (1992) and is found to be equivalent to the MnO-Mn$_3$O$_4$ solid oxygen buffer (Fig. 2.1). The experiments have been performed using both Pt and Au$_{80}$Pd$_{20}$ capsules. Results show that fO$_2$ values obtained in Au$_{80}$Pd$_{20}$ capsules are slightly lower than in Pt capsules but are within the error of the method of Taylor et al. (1992).
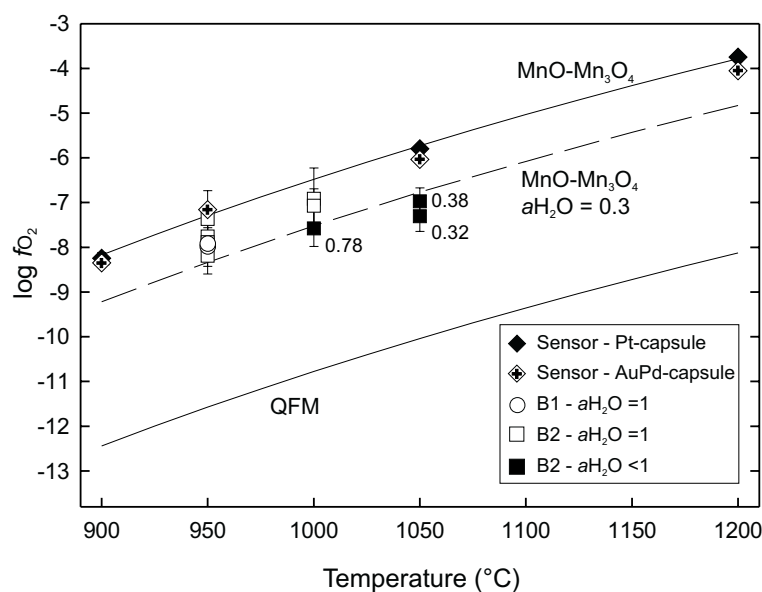
Figure 2.1 Intrinsic fo$_2$ in the used IHPV measured by solid sensor technique after Taylor et al. (1992) and calculated fo$_2$ using coexisting magnetite/ilmenite pairs (Andersen et al., 1993). Solid lines show MnO-Mn$_3$O$_4$ and QFM buffer curve. Dashed line shows the shift of fo$_2$ relatively to MnO-Mn$_3$O$_4$ buffer curve at lower water activities (aH$_2$O = 0.3) towards more reducing conditions in experiments. Note that fo$_2$ values calculated after Andersen et al. (1993) for magnetite/ilmenite pairs crystallized at aH$_2$O < 1 show clearly more reducing conditions in charge. NiPd Sensor measurements after Taylor et al. (1992) have been performed using both Pt and Au$_{80}$Pd$_{20}$ capsules.

2.2.2. Starting Material

Two synthetic starting compositions (Tab. 2.1) have been used for the crystallization experiments: a primitive MORB glass B1 for the first set of experiments and a more evolved MORB glass B2 corresponding to a residual glass composition obtained after 50% crystallization at 1100 °C (run no. 42; Tab. 2.1, 2.2). The starting materials have been made from synthetic oxide and carbonate powders. The oxide powder mixtures have been placed into a Pt crucible and fused at 1600 °C, 1 atm, and a log fO$_2$ corresponding to about -0.68 (air). The resulting glass was removed from the Pt crucible and grounded. This glass powder was melted a second time (same conditions as above). To avoid alkali loss from the glass, melting duration has not exceeded 1.5 h. Microprobe analyses of chips extracted from the top, middle and bottom of the glass showed them to be homogeneous (see standard deviation in Tab. 2.1). The glass B1 lies within the compositional range of natural primitive MORB´s.

2.2.3. Sample Preparation and Experimental Procedure

For the crystallization experiments a powder was made of the starting glasses (grain size < 50 µm). First attempts were made by preparing the samples with dry powder and a given amount of water added with the help of a syringe in Au$_{80}$Pd$_{20}$ capsules. After loading the capsules into the rapid-quench sample holder, they were first held for about 1 h above the

Table 2.1. Composition of natural primitve MORB and synthetic MORB B1 and B2 (starting material)

	n^a	SiO$_2$	TiO$_2$	Al$_2$O$_3$	FeO* ^{c}	MnO	MgO	CaO	Na$_2$O	K$_2$O	P$_2$O$_5$
natural MORB^b		49.47c (16)^d	0.83 (10)	16.35 (54)	8.71 (49)	0.16 (9)	9.80 (26)	12.35 (33)	2.16 (12)	0.07 (5)	0.09 (5)
synthetic MORB B1	18	49.64 (27)	0.87 (5)	16.07 (16)	8.63 (7)	0.15 (7)	9.77 (9)	12.44 (16)	2.28 (9)	0.08 (3)	0.08 (5)
glass run no. 42	10	51.38 (57)	1.46 (11)	15.97 (57)	10.98 (25)	0.19 (15)	6.16 (29)	10.50 (30)	3.06 (24)	0.12 (7)	0.18 (12)
synthetic MORB B2	12	51.17 (23)	1.43 (6)	15.93 (16)	10.72 (26)	0.21 (7)	6.49 (7)	10.57 (13)	3.13 (11)	0.15 (4)	0.19 (7)

^{a} number of analyses

^{b} average composition of primitive MORB compositions from: Frey et al. (1974), Bryan and Moore (1977) and Natland and Melson (1980), all in Ethon (1991); Melson and O´Hearn (1986) in Brooks et al. (1991); Langmuir et al. (1977); Spulber and Rutherford (1983); Christie and Sinton (1986); McKenzie and Bickle (1988)

^{c} oxide concentrations from microprobe are normalized to 100 wt% with all Fe as FeO* (total iron)

^{d} number in parantheses are one standard deviation of replicate analyses in terms of least units cited

liquidus temperature at 200 MPa to obtain a homogeneous distribution of H_2O in the melt and to allow redox equilibrium of the melt. In a second step, the temperature was lowered to the desired run temperature. The resulting products clearly showed disequilibrium features. Clinopyroxene minerals were zoned. Compositional variations for Al_2O_3 with concentrations of 5 – 9 wt% within a single crystal were measured. To avoid these effects, charges with dry glass plus water have been brought directly to the desired run temperature. Results for relatively high temperatures (1050 – 1150 °C at 200 MPa) did not show disequilibrium features, but the mineral size and distribution were heterogeneous at lower temperatures and low aH_2O. This is probably due to a crystallization which takes place before equilibrium distribution of water was achieved in the glass powder.

Therefore, the experimental strategy used in this study consisted in using pre-hydrated glass powder as starting materials. Large amounts of dry glass powder were placed into $Au_{80}Pd_{20}$ capsules (i.d. 0.5 cm; o.d. 0.54 cm at 3 cm length) and stuffed with the help of a steel piston. Distilled and deionized water was added to the charge using a microsyringe in five steps to achieve homogeneous H_2O distribution within the capsule. The sealed capsules were heated at 1250 °C and 200 MPa (above liquidus) for 24 h in an IHPV equipped with the rapid-quench device described above. Homogeneous crystal- and bubble free glasses were obtained and the water content were determined by Karl-Fischer-Titration (KFT; for technique and precision see Behrens, 1995; Holtz et al., 1995; Behrens et al., 1996). For B1, glasses containing 4.70 wt% (water-saturated), 2.53 wt% ($aH_2O = 0.47$), 1.49 wt% ($aH_2O = 0.21$), and 0.89 wt% H_2O ($aH_2O = 0.09$) have been synthesized. For B2, glasses containing 4.50 wt% (water-saturated), 2.05 ($aH_2O = 0.34$), 1.25 wt% ($aH_2O = 0.15$), and 0.74 wt% H_2O ($aH_2O = 0.06$) have been synthesized. For each starting glass only one KFT analysis has been made. Thus, the homogeneous distribution of water has not been checked. However, this technique has proved to be successful for the synthesis of large homogeneous hydrous glass samples (e.g., Schulze et al., 1999). In addition, the whole batch of each hydrous glass was crushed and

Table 2.2. Experimental conditions and results for composition B1(MnO-Mn3O4)

run	wt% H O[a] bulk	wt% H O[b] in melt	aH O	fH O [bar]	log fo [c] [bar]	ΔQFM[d] [bar]	phases detected and modal proportions [e, f]	ΣR²
1150°C; 205.4 MPa; 23.8 h								
66	4,70	*4.55 g*	1	2074	-4,38	+4.33	gl(100) fl	
65	2,53	2,56	0,47	971	-5,04	+3.67	gl(98.7) ol(1.3)	0,52
64	1,49	1,54	0,21	441	-5,73	+2.99	gl(96.5) ol(3.5)	0,30
63	0,89	1,01	0,10	214	-6,36	+2.36	gl(88.5) ol(4.7) cpx(2.6) pl(4.2)	0,31
1100°C; 202.1 MPa; 21 h								
45	4,70	*4,57*	1	2011	-5,03	+4.32	gl(98.2) ol(1.8) fl	0,42
44	2,53	3,13	0,61	1218	-5,47	+3.89	gl(80.8) ol(5.2) cpx(9.6) pl(4.4)	0,52
43	1,49	2,45	0,43	861	-5,77	+3.59	gl(60.9) ol(8.2) cpx(15.4) pl(15.5)	0,27
42	0,89	1,79	0,27	544	-6,17	+3.19	gl(49.6) ol(8.9) cpx(17.6) pl(23.9)	0,15
1100°C; 203.8 MPa; 72 h								
62	4,70	*4,56*	1	2029	-5,03	+4.32	gl(98.5) ol(1.5) fl	0,40
61	0,89	1,72	0,25	506	-6,24	+3.11	gl(51.8) ol(8.6) cpx(17.4) pl(22.2)	0,21
1050°C; 201.7 MPa; 20.75 h								
41	4,70	*4,73*	1	1964	-5,73	+4.31	gl(77.5) ol(7.4) cpx(10.5) pl(3.9) mt(0.7) fl	0,33
40	2,53	*4,84*	1	1964	-5,73	+4.31	gl(51.4) ol(9.7) cpx(18.1) pl(18.8) mt(2.0) fl	0,35
39	1,49	3,63	0,70	1373	-6,04	+4.00	gl(41.0) ol(8.9) cpx(23.8) pl(24.7) mt(1.6)	0,20
38	0,89	2,34	0,38	752	-6,56	+3.48	gl(38.1) ol(8.3) cpx(24.7) pl(26.4) mt(2.5)	0,28
1000°C; 205 MPa; 20 h								
37	4,70	*5,09*	1	1947	-6,48	+4.30	gl(47.6) ol(5.8) cpx(25.9) pl(15.1) mt(3.5) am(2.1) fl	0,17
36	2,53	*5,08*	1	1947	-6,48	+4.30	gl(34.7) ol(8.0) cpx(25.8) pl(27.7) mt(3.8) fl	0,34
35	1,49	*5,21*	1	1947	-6,48	+4.30	gl(24.9) ol(7.9) cpx(27.8) pl(33.2) mt(4.3) opx(1.9) fl	0,32
34	0,89	*5,19*	1	1947	-6,48	+4.30	gl(17.0) ol(5.7) cpx(29.9) pl(37.4) mt(4.5) opx(5.5) fl	0,25
950°C; 202.5 MPa; 20 h								
49	4,70	*5,19*	1	1862	-7,29	+4.28	gl(20.4) cpx(17.4) pl(25.8) mt(3.9) opx(3.9) am(28.6) fl	0,10
48	2,53	*5,25*	1	1862	-7,29	+4.28	gl(12.6) cpx(16.7) pl(35.7) mt(4.4) opx(7.1) am(23.5) fl	0,21
47[h]	1,49	*5,24*	1	1862	-7,29 (-7.91)i	+4.28	gl(4.8) cpx(26.0) pl(44.3) mt(4.1) ilm(2.4) opx(13.9) am(4.5) fl	
46[h]	0,89	*5,24*	1	1862	-7,29 (-7.99)	+4.28	gl(4.2) cpx(26.3) pl(45.5) mt(3.1) ilm(2.9) opx(13.6) am(4.4) fl	

[a] wt% H O in starting glasses determind by Karl-Fischer-Titration

[b] water content of the residual glasses estimated by mass balance calculations (see text)

[c] log fo based on equation for MnO-Mn O buffer curve (Chou 1978) assuming intrinsic buffering capacity of used IHPV corresponding to the MnO-Mn₃O₄ buffer (see text)

[d] Δ QFM indicates log fo (experiment) - log fo (QFM buffer) as estimated by Schwab and Küstner (1981)

[e] gl glass, ol olivine, cpx clinopyroxene, opx orthopyroxene, pl plagioclase, mt magnetite, ilm ilmenite, am amphibole, fl fluid (H_2O)

[f] phase proportions calculated by mass balance are given in wt%

[g] numbers in italics indicate runs with aH₂O = 1 where water content was calculated using the Burnham model (Burnham 1979)

[h] melt composition was calculated using ImageAnalysis (see text)

[i] log fo_2 values in parentheses are calculated using experimentally crystallized coexisting ilm/mt pairs (Andersen et al. 1993)

[j] phases in parentheses have been identified qualitatively

mixed, so that the bulk water content is identical in all charges performed with the same starting glass.

The glasses and capsule walls have been analyzed by microprobe to check for iron loss or enrichment, respectively. No iron was detected in the capsule material and the Fe content of the hydrous glasses is equivalent to that of the dry starting material. Thus, the oxidizing conditions in the IHPV and the use of $Au_{80}Pd_{20}$ capsule material completely prevent iron loss (Kawamoto and Hirose, 1994).

Table 2.3. Experimental conditions and results for composition B2 (MnO-Mn$_3$O$_4$ buffer)

run	wt% H$_2$O^a bulk	wt% H$_2$O^b in melt	aH$_2$O	fH$_2$O [bar]	log fO$_2$^{c} [bar]	Δ QFM^d [bar]	phases detected and modal proportions $^{e, f}$					ΣR^2
1150°C; 203.1 MPa; 20.15 h												
86	4.50	4.58 g	1	2058	-4.38	+4.33	gl(100)	fl				
87	2.05	2.05	0.34	695	-5.33	+3.39	gl(100)	mt(tr) ^{j}				
88	1.25	1.25	0.15	309	-6.03	+2.69	gl(100)	mt(tr)				
89	0.74	0.75	0.06	127	-6.80	+1.91	gl(98.7)	mt(1.3)				0.32
1100°C; 200.8 MPa; 21.5 h												
90	4.50	4.63	1	1997	-5.03	+4.32	gl(97.8)	mt(2.2)	fl			0.41
91	2.05	2.10	0.34	688	-5.96	+3.40	gl(97.7)	cpx(1.2)	mt(1.1)			0.52
92	1.25	1.84	0.28	554	-6.15	+3.21	gl(68.1)	cpx(12.5)	pl(16.5)	mt(2.9)		0.21
93	0.74	1.45	0.19	386	-6.46	+2.90	gl(51.0)	cpx(18.5)	pl(27.2)	mt(3.3)		0.45
1050°C; 204.4 MPa; 20 h												
94	4.50	4.80	1	1992	-5.73	+4.31	gl(92.5)	cpx(2.5)	mt(5.0)	fl		0.61
95	2.05	2.65	0.43	861	-6.45	+3.58	gl(77.5)	cpx(15.7)	mt(6.8)	pl(tr)		0.74
96	1.25	2.48	0.38	765	-6.56 (-6.97)i	+3.48	gl(50.5)	cpx(19.8)	opx(1.9)	pl(20.6)	mt(6.5) ilm(0.7)	0.37
98	0.74	2.22	0.32	644	-6.71 (-7.28)	+3.33	gl(33.2)	cpx(18.9)	opx(4.7)	pl(35.4)	mt(6.7) ilm(1.1)	0.60
1000°C; 203.9 MPa; 19.75 h												
99	4.50	5.06	1	1936	-6.48	+4.30	gl(75.1)	cpx(18.3)	mag(6.6)	fl		1.03
100	2.05	5.18	1	1936	-6.48 (-6.91)	+4.30	gl(35.4)	cpx(23.7)	opx(3.0)	pl(30.3)	mt(6.3) ilm(1.3) fl	0.52
101	1.25	5.26	1	1936	-6.48 (-7.07)	+4.30	gl(21.8)	cpx(24.4)	opx(5.0)	pl(40.8)	mt(5.4) ilm(2.6) fl	0.38
102	0.74	4.23	0.78	1516	-6.69 (-7.58)	+4.08	gl(17.5)	cpx(29.5)	opx(2.4)	pl(42.3)	mt(7.6) ilm(0.7)	0.75
950°C;201 MPa; 21.5 h												
103	4.50	5.19	1	1848	-7.29 (-7.37)	+4.28	gl(41.5)	cpx(19.1)	pl(19.1)	mt(5.7)	ilm(2.2) am(14.8) fl	0.61
104	2.05	5.14	1	1848	-7.29 (-7.76)	+4.28	gl(16.8)	cpx(22.4)	opx(6.0)	pl(45.7)	mt(6.7) ilm(2.4) fl	1.04
105	1.25	5.29	1	1848	-7.29 (-7.92)	+4.28	gl(15.5)	cpx(24.1)	opx(7.3)	pl(45.0)	mt(5.5) ilm(2.6) fl	0.20
106	0.74	5.20	1	1848	-7.29 (-8.19)	+4.28	gl(14.0)	cpx(28.0)	opx(3.2)	pl(45.4)	mt(6.7) ilm(2.7) fl	0.15
950°C; 202.6 MPa; 96h												
111	2.05	5.18	1	1863	-7.29 (-7.83)	+4.28	gl(19.1)	cpx(19.2)	opx(6.2)	pl(45.8)	mt(6.9) ilm(2.8) fl	0.64

for notes and abbreviations see Table 2.2

For the crystallization experiments, the hydrous glasses were crushed in a steel mortar and sieved to fractions with grain sizes of 100 - 200 µm. About 50 - 80 mg of the hydrous glass powders were sealed in Au$_{80}$Pd$_{20}$ capsules (i.d. 0.3 cm; o.d. 0.34 cm at 1 cm length). A set of four capsules (corresponding to the four different bulk H$_2$O contents of B1 and B2) have been fixed to the rapid-quench device and brought directly to run temperature. Phase relations were investigated at 200 MPa in 50 °C intervals in the temperature range 1150 – 950 °C (Tab. 2.2, 2.3). The run duration was 24 h except for runs no. 62 and 61 (B1; 72 h) and run no. 111 (B2; 96 h). Results of these experiments have been compared with 24 h runs conducted at identical pressure and temperature (runs no. 45, 42 and 104; see below and Tab. 2.2, 2.3).

2.2.4. Calculations of aH$_2$O and fO$_2$

It has been shown that the thermodynamic model of Burnham (1979) is not always correct for the calculation of aH$_2$O and melt water contents, especially at high pressures (e.g., water

solubility can be underestimated by 20% relative at 500 MPa; Holtz et al., 1995). The calculated H_2O solubilities after Burnham (1979) for synthesized MORB glasses B1 and B2 (at 200 MPa and 1250 °C) are 4.54 wt% H_2O and 4.57 wt% H_2O, respectively. Measured H_2O solubilities (determined by KFT) for these glasses were 4.70 wt% ($\pm$ 0.09) for B1 and 4.50 wt% ($\pm$ 0.10) for B2. Due to the good agreement between measured and calculated water solubilities we have used the model of Burnham (1979) to calculate melt water content at aH_2O = 1 in this study. In addition, water activities have also been calculated for runs in which aH_2O is < 1.

Oxygen fugacity for experimental charges was computed from the water dissociation reaction, where $fH_2O°$ was extrapolated from Burnham et al. (1969) with a K_w from Robie et al. (1978) and γH_2O from Pitzer and Sterner (1994). fH_2 is imposed by the vessel (see above) and corresponds to the MnO-Mn_3O_4 solid oxygen buffer (based on the equation of Chou, 1978). fH_2O and thus fO_2 in water-undersaturated experiments was obtained from aH_2O (Scaillet et al., 1995).

2.2.5. Analytical Techniques and Determination of Phase Proportions

The electron microprobe analyses of glasses and minerals were performed with a Cameca Camebax and a Cameca SX 100 microprobe and are listed in Tables 2.4 – 2.11. Analytical conditions for solid phases were 15 kV, 15 nA beam current, and counting times of 5 s for Na and K and 10 s for all other elements. Glasses have been analyzed with a defocused beam of 20 µm with a 5 nA beam current and counting times of 2 s for Na and K and 5 s for the other elements. In runs with high degree of crystallization (typically melt fraction below 30 wt%) the beam was defocused as much as possible. Loss of alkalis was observed for spot sizes below 15 µm. In this case analyses were corrected by a loss factor using the B1 hydrous starting glasses as standards with known water contents.
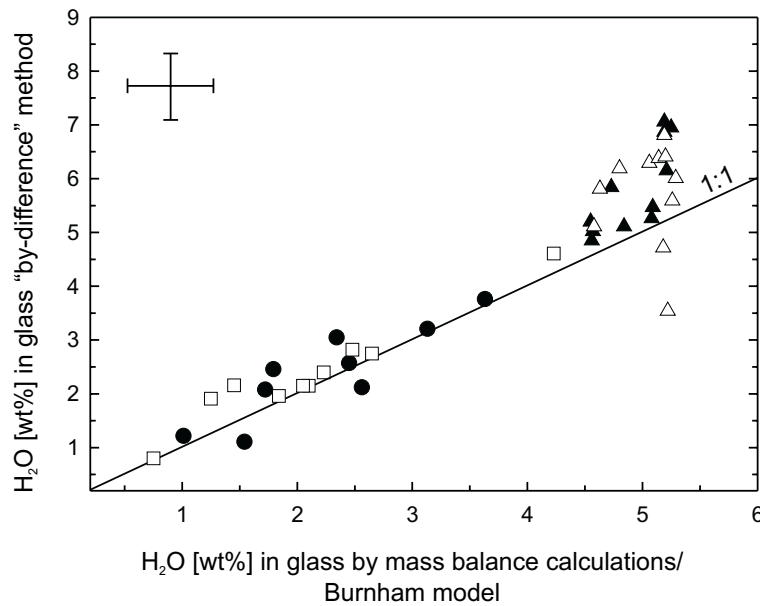
Figure 2.2 Comparison of melt water contents for B1 and B2 obtained by the mass balance calculations (aH₂O < 1; B1 dots, B2 open squares) and melt water contents calculated using the "Burnham model" (aH₂O = 1; B1 filled triangles, B2 open triangles) with the H₂O contents obtained from the "by-difference" method. Error bars correspond to the average errors obtained for values using the "by-difference" method (± 1.23 wt%) and mass balance calculations (± 0.74 wt%) assuming an error of 20% relative for phases with 1 – 10 wt% abundances.

Phase proportions (wt%) were determined by mass balance calculations (glass analyses were normalized to 100 wt% for mass balance calculations). Melt water contents in runs with aH₂O < 1 have been calculated from the known melt fractions (from mass balance calculations) and known bulk water content of the starting materials. No attempts were made to consider crystal water content in amphiboles, because a fluid phase was always present in runs within the amphibole stability field (Tab. 2.2, 2.3) suggesting an aH₂O = 1.

In experimental charges in which a fluid phase was present, indicating water-saturated conditions, the melt water content was calculated using the thermodynamic model of Burnham (1979) at given pressure (p), temperature (T), and melt composition assuming aH₂O = 1. Additionally, the melt water content was also estimated for all runs with the "by-difference" method (Koepke, 1997; Devine et al., 1995). The comparison of melt water contents obtained by mass balance calculations (aH₂O <1) and from the "Burnham model" (aH₂O = 1) with the water contents determined with the "by-difference" method show good agreement (Fig. 2.2).

In experiments with low melt fractions in which water-saturated conditions are mostly prevailing (near water-saturated conditions are prevailing because of the high amount of anhydrous minerals), melt water contents obtained by the "by-difference" method are relatively higher than those from the "Burnham model" (see triangles in Fig. 2.2 for runs with

aH$_2$O = 1). This is probably due to too low microprobe totals resulting from analyses of very small melt pools with a beam that could not be defocused.

It was not possible to analyze the glass composition of the near-solidus experiments no. 47 and 46, because the remaining glass pools were too small even with a focused beam spot. Hence, the phase proportions (vol%) have been estimated from back-scattered electron (BSE) images using ImageAnalysis$^{©}$ 3.0 software (Koepke et al., 1996; Gardien et al., 1995). The proportion in wt% (Tab. 2.2) was recalculated assuming typical average densities for solid phases and for melt (melt density of 2.28 g/cm^3 is estimated from glass composition of run no. 48 after Lange, 1997; Lange and Carmichael, 1990; Ochs III and Lange, 1999). For these two experiments the compositions of the glasses were roughly determined by mass balance calculations (Tab. 2.11).

2.3. Results

2.3.1. General Information on the Effect of H$_2$O on Experimental Results

In this investigation on the influence of water on phase relations, it should be emphasized that there are different ways to understand the effect of H$_2$O on solid phase compositions and liquid lines of descent. The effect of bulk water content can be estimated by comparing experimental charges obtained at identical temperature with different bulk water content of the charge. However, the comparison of such experiments shows that the crystal amount is not constant with changing bulk water contents, especially for high temperature runs (e.g., runs no. 42 to 45 at 1100 °C, Tab. 2.2, Fig. 2.3a). In these high temperature experiments, the residual melts have also different water contents and therefore different aH$_2$O prevail (Fig. 2.3). In contrast, for low temperature runs (e.g., runs no. 34 to 37 at 1000 °C, Tab. 2.2) the crystal content is always high enough to attain water-saturated conditions (due to crystallization of mostly anhydrous phases). In this case, the comparison of experiments performed at a constant temperature of 1000 and 950 °C allows to estimate the effect of bulk water content for a constant aH$_2$O of 1. In the following, the results will be discussed either
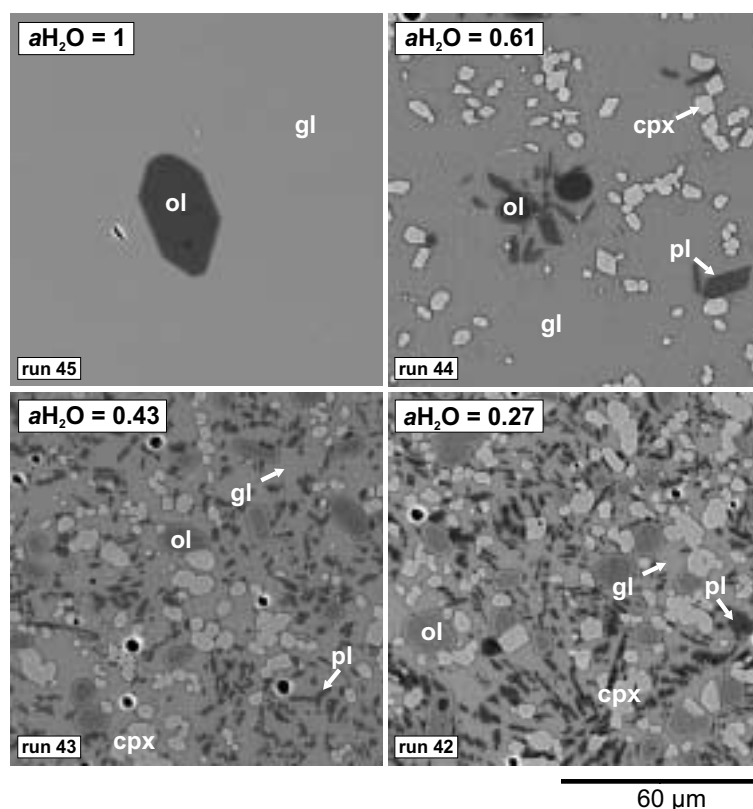
Figure 2.3a Back scattered electron images (BSE) of quench products obtained at 1100 °C from B1 with examples of the phases observed. Abbreviations see Figure 2.4. Images show variation in modal proportion and phase stability in experiments varying bulk water content and thus aH₂O of the charge for a constant temperature. It is emphasized that the low viscosity basaltic melts have been quenched to homogeneous glasses without disequilibrium quench effects.
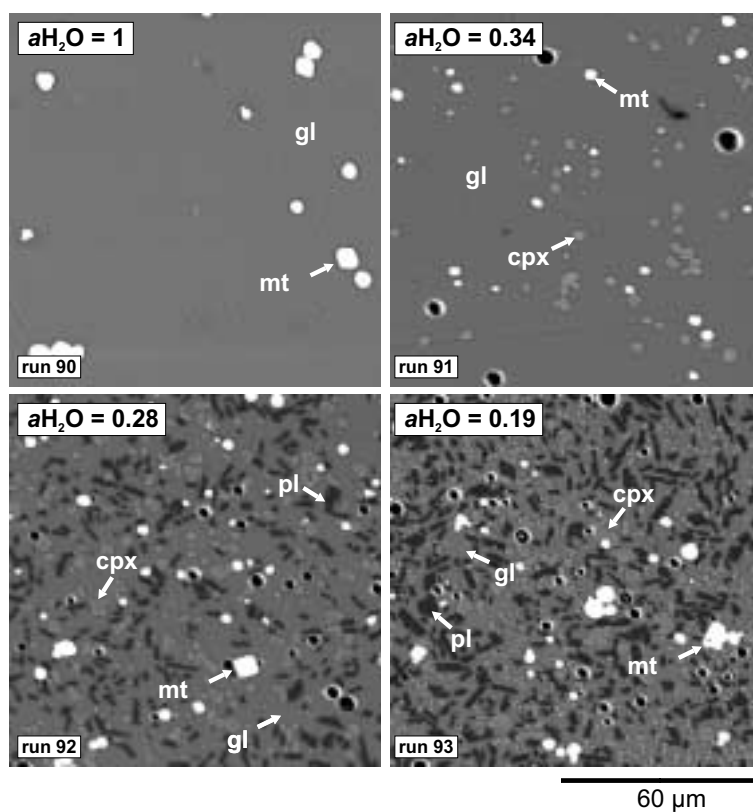

Figure 2.3b Back scattered electron images (BSE) of quench products obtained at 1100 °C from B2 examples of the phases observed. Abbreviations see Figure 2.4. For detailed comments see Figure 2.3a.

31

as a function of bulk water content or aH$_2$O. It is emphasized that these two parameters are not identical.

In addition, a change in water content of the melt (and thus aH$_2$O), while holding all other parameters constant, can result in a change of fO$_2$ (see above). Oxygen fugacity remains constant in runs with aH$_2$O = 1 at isothermal conditions. In this case the fO$_2$ corresponds to the "intrinsic" fO$_2$ conditions of the IHPV (see above). In contrast, at higher temperatures, when H$_2$O-saturation has not been reached, fO$_2$ depends on prevailing aH$_2$O (Scaillet et al., 1995) (Tab. 2.2, 2.3). Hence, it is difficult to discriminate between the individual effects of aH$_2$O and fO$_2$, especially in the discussion on the evolution of iron-bearing phases.

2.3.2. Achievement of Equilibrium

The experimental technique used in this study (crystallization experiments) is known to be the best method to approach equilibrium conditions (Pichavant, 1987), when compared to melting experiments in which residual minerals can remain for long duration in the surrounding melt. In addition, it has been shown above that two step experiments with heating up above the liquidus and subsequent cooling led to heterogeneous clinopyroxene compositions, which is evidence for undercooling. In contrast to the method of Pichavant (1987), using dry glass powder and fluid as starting material, hydrous glass powders have been used in this study. This procedure has the advantage to provide homogenous H$_2$O distribution directly from the beginning of the experiments. Furthermore, redox state of the glass has been equilibrated at given aH$_2$O (note that fO$_2$ decreases with decreasing aH$_2$O; see below).

Following features are evidence for near equilibrium conditions. 1. All phases which crystallized were homogeneous (or heterogenities were less than analytical precision of the electron microprobe) and their composition changed with the experimental conditions, following expected compositional trends. 2. The crystal distribution is homogeneous in all experiments (Fig. 2.3a, b). 3. Iron loss could be completely avoided due to the high fO$_2$. 4. Phase relations and compositions were identical for different run duration (24 h and up to 96

h) at high and low temperatures (for B1 compare runs no. 62 and 61 with no. 45 and 42, respectively, and for B2 run no. 111 with no. 104; Tab. 2.2, 2.3). 5. Mineral-melt and mineral-mineral partitioning coefficients (for olivine, plagioclase, amphibole, and Fe-Ti oxides) are in good agreement with published data from other studies (see below). 6. The formation of quench crystals was avoided (Fig. 2.3a, b) so that there is no need to distinguish between quench and stable phases or performing integrative measurements of glass and quench
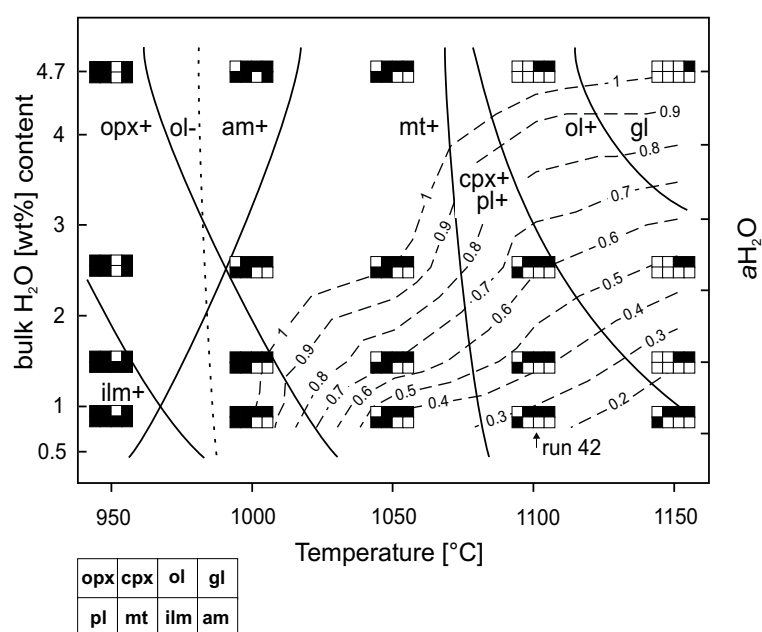
Figure 2.4a Phase relationships of starting material B1 as a function of T-bulk water content-aH$_2$O at 200 MPa. Abbreviations: gl glass, ol olivine, pl plagioclase, cpx clinopyroxene, mt magnetite, ilm ilmenite, am amphibole. Solid lines indicate beginning of crystallization (+) of a phase in equilibrium with the melt. Dashed lines mark phase-out boundary, suggesting phase is no more stable at given p-T-H$_2$O conditions. Lines of equal aH$_2$O are determined from aH$_2$O calculated for each charge after Burnham (1979; Tab. 2.2, 2.3) and if necessary for the sake of completeness extrapolated.
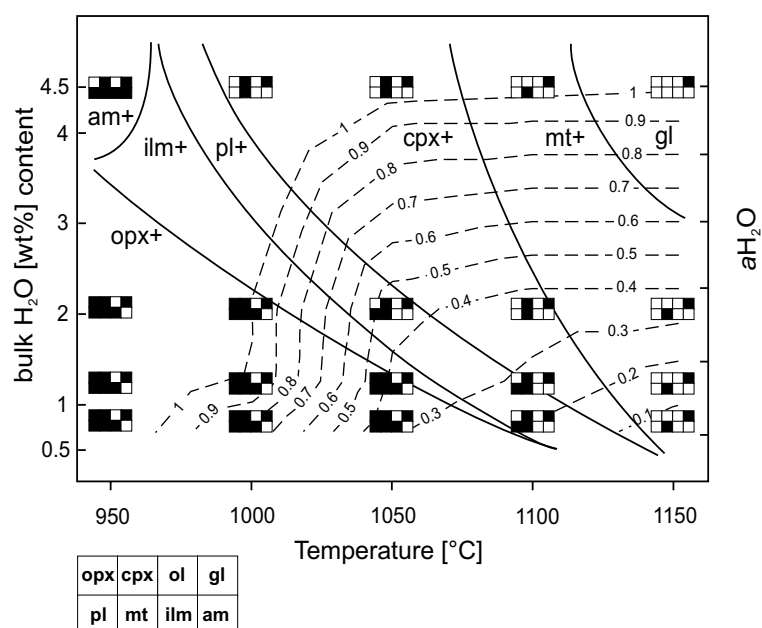
Figure 2.4b Phase relationships of starting material B2. For abbreviations and detailed comments see Figure 2.4a.
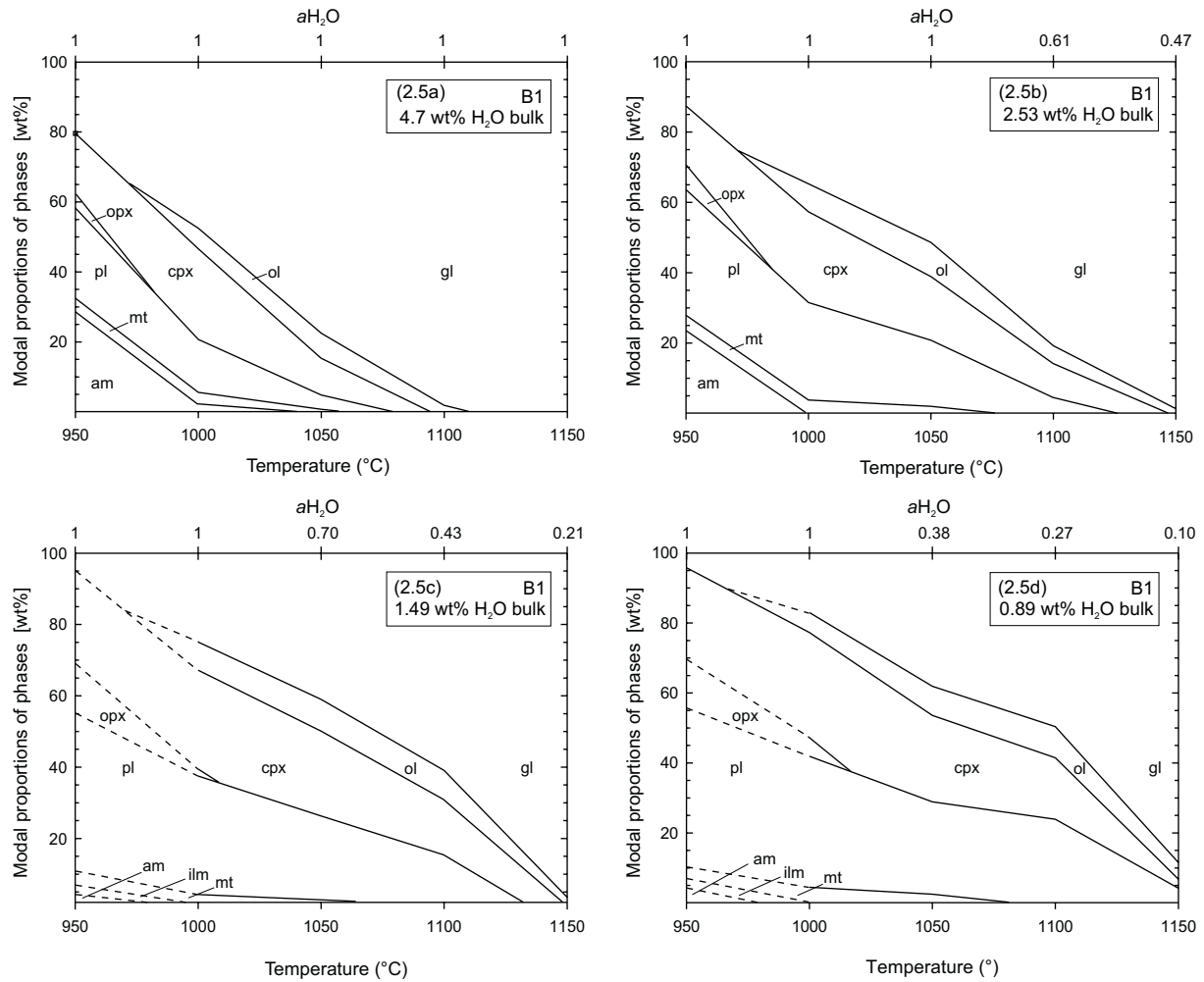
Figure 2.5a-d Modal proportions of phases obtained in B1 crystallization experiments as a function of temperature, bulk water content (insets), and aH₂O. Abbreviations see Figure 2.4. Modal proportions of phases have been obtained by mass balance calculations. Dashed lines show modal phase proportions of experiments no. 47 and 46 which have been estimated from back-scattered electron (BSE) pictures using ImageAnalysis© 3.0 (see comments in chapter analytical techniques).

crystals, as has been done in previous studies (e.g., Helz, 1976). 7. The redox state of the starting hydrous glasses correspond to that of the initial conditions of the crystallization experiments (which is important considering that at identical p and T a decrease in aH₂O can decrease fO_2 about two log units; e.g. compare runs no. 66 and 63; Table 2.2). This is particularly important in experiments conducted with depolymerized systems, in which crystallization occurs rapidly (see chapter 1) showed that compositional zonation of olivine can result from using starting glass which is not equilibrated with respect to fO_2 and aH₂O.

2.3.3. Phase Relations

Experimental conditions and results are listed in detail in Tables 2.2 and 2.3. Phase relations of starting materials B1 and B2 are shown in T-H$_2$O diagrams (Fig. 2.4a, b). Phase boundaries correspond to the presence or absence of phases in the crystallization experiments (detected by microprobe). The influence of water on phase relations is represented both in terms of bulk water content and lines of equal aH$_2$O of the melt (Fig. 2.4a, b). A relation between aH$_2$O and water content of the melt can be found in Tables 2.2 and 2.3.

2.3.3.1. Primitive MORB System (B1)

Olivine is the liquidus phase for all bulk water contents in B1 (Fig. 2.4a). At aH$_2$O = 1 and aH$_2$O = 0.6 the saturation boundary is about 1125 °C and 1150 °C, respectively. In runs below 1000 °C olivine is no longer stable. This is supported by the decreasing calculated modal abundance of olivine in runs at 1000 °C compared with 1050 °C (Tab. 2.2; Fig. 2.5; see below). Furthermore, resorption of olivine with changes from euhedral to rounded crystals could be detected in BSE images (in runs at 1050 °C and 1000 °C). Plagioclase and clinopyroxene saturation curve are almost identical and the relative order of crystallization is unknown. However, phase proportions suggest that the curve of plagioclase saturation lies at slightly higher temperatures. Plagioclase and clinopyroxene start to crystallize between 1100 °C and 1050 °C at aH$_2$O = 1 and at about 1150 °C at aH$_2$O = 0.2. Magnetite was found in all runs below 1050 °C. Amphibole is stable under water-saturated conditions only. It is observed in all runs at 950 °C and at 1000 °C in the composition with 4.70 wt% bulk H$_2$O content. Orthopyroxene (opx) is stable in runs with 0.89 and 1.49 wt% bulk H$_2$O content at 1000 °C and in all runs at 950 °C. The ilmenite stability field is restricted to run conditions of 950 °C with 0.89 and 1.49 wt% bulk H$_2$O content.

2.3.3.2. Differentiated MORB System (B2)

In contrast to B1, olivine was never observed in the B2 starting composition. Magnetite crystallizes as the liquidus phase for all bulk water contents (Fig. 2.4b) and its liquidus temperature is below 1150 °C for bulk water content 4.50 wt%. Clinopyroxene appears between 1100 °C and 1050 °C at aH$_2$O = 1 and 1150 °C and 1100 °C for aH$_2$O < 0.3. Saturation curve for plagioclase depends strongly on aH$_2$O. At water-saturated conditions plagioclase is only stable below 1000 °C. At lower water activities the saturation temperature of plagioclase increases up to 1100 °C (aH$_2$O = 0.25). The ilmenite saturation curve depends also on aH$_2$O and is approximately 50 °C below that of plagioclase. In contrast to B1, orthopyroxene in B2 is observed at higher temperature for low bulk water contents. It appears
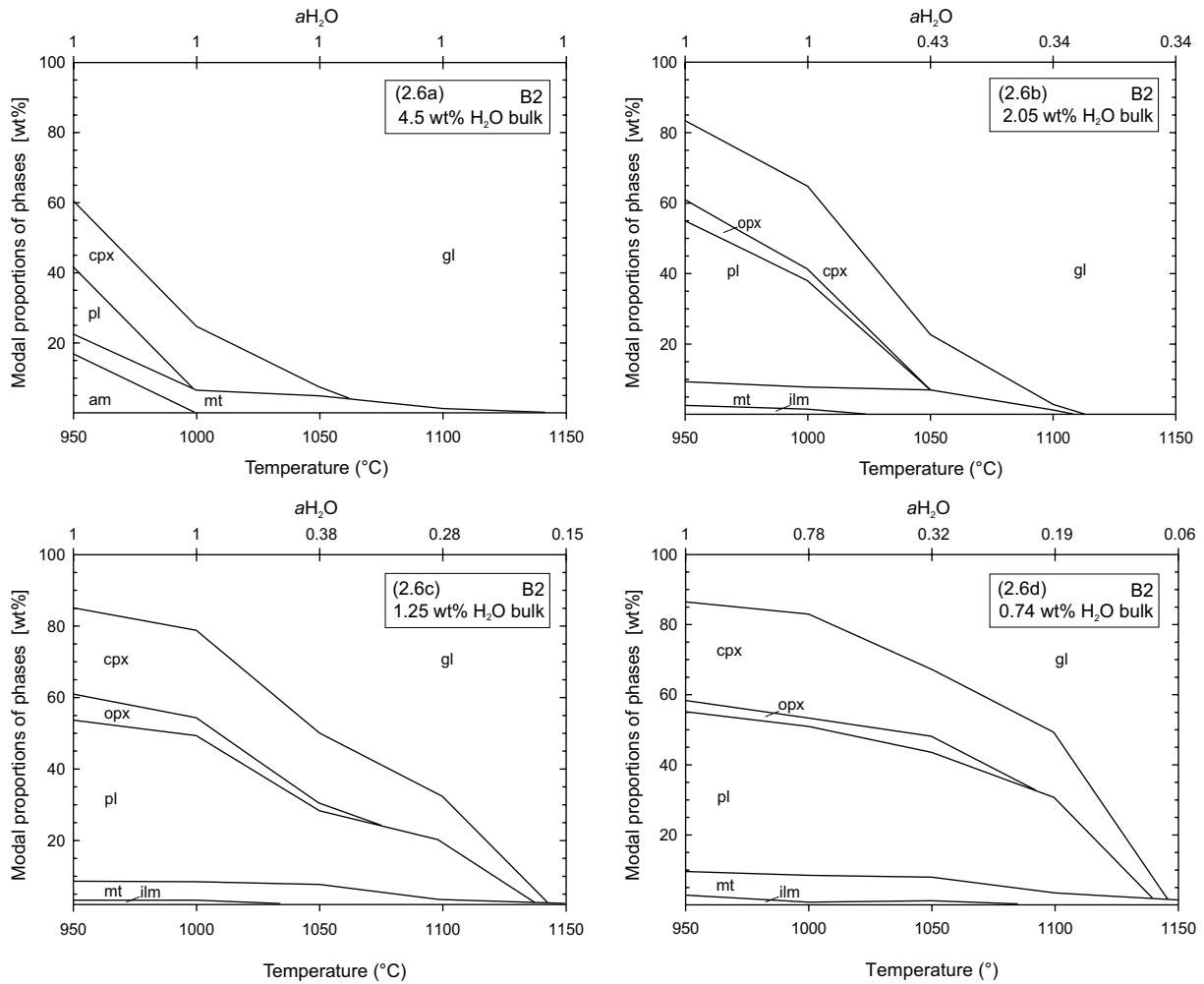

Figure 2.6a-d Modal proportions of phases obtained in B2 crystallization experiments as a function of temperature, bulk water content, and aH$_2$O. For abbreviations see Figure 2.4 and detailed comments Figure 2.5.

first at 1050 °C for an aH$_2$O of 0.38 (run no. 96; Tab. 2.3) but is not stable at 950 °C and 4.5 wt% bulk H$_2$O. At this last condition amphibole is observed.

2.3.4. Phase Chemistry

2.3.4.1. Olivine

Analyses of olivine are reported in Table 2.4. The evolution of olivine composition as a function of temperature and bulk water content is shown in Figure 2.7. The forsterite content in olivine (X_{Fo}) decreases with decreasing bulk water content. For a constant temperature, X_{Fo} varies considerably as a function of bulk water (e.g., at 1100°C from X_{Fo92} to X_{Fo84} for a bulk water content of 4.7 and 0.89, respectively). X_{Fo} falls with decreasing temperature from 1150 - 1050 °C to minimum values of Fo$_{89}$ (4.70 wt% bulk H$_2$O content) and Fo$_{83}$ (0.89 wt% bulk H$_2$O content) and raises again at temperatures < 1050 °C. This is a consequence of increasing magnetite crystallization leading to slightly higher MgO and lower FeO* (total iron) concentrations in the melt (Fig. 2.5, 2.7, 2.9; Tab. 2.2). One of the most significant minor component of olivine is calcium (Libourel, 1999), with concentrations depending on X_{Fo} and ranging between 0.19 wt% and 0.41 wt% CaO (Tab. 2.4).
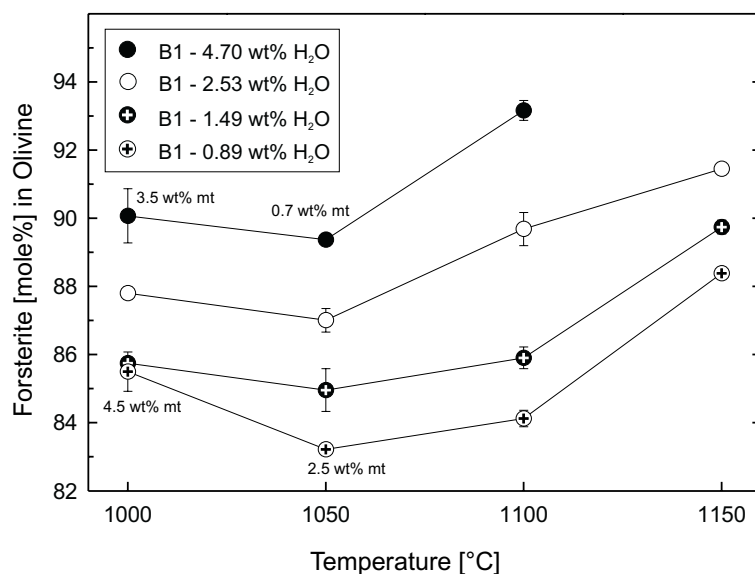
Figure 2.7 Olivine composition as a function of temperature and bulk water content. Errors bars correspond to standard deviation of average olivine compositions. If no error bars are given, the height of the symbols corresponds to the average error. For bulk water contents of 4.70 and 0.89 wt% numbers indicate the proportion of magnetite (wt% mt) crystallization from mass balance calculations.

2.3.4.2. Pyroxene

Clinopyroxenes and orthopyroxenes obtained in runs with B1 vary only moderately with changing experimental conditions and have an average composition of $En_{45}Fs_{12}Wo_{43}$ ($\pm$ 1.3 mole%) and ($En_{82}Fs_1Wo_3 \pm 0.9$ mole%), respectively (Tab. 2.5, 2.6). En and Fs contents in B1 clinopyroxene crystals increase in runs with $aH_2O < 1$ (and thus lower fO_2) and remains relatively constant at water-saturated conditions for constant temperatures. Clinopyroxenes in equilibrium with ilmenite (B1 runs no. 47 and 46) become less Fs-rich at the expense of the Wo content. For a given bulk H_2O content, En-content raises with decreasing temperature which is in contrast to olivine. The comparison of orthopyroxenes obtained at 1000 °C and at 950 °C shows that the En-content increases at the expense of the Fs- and Wo contents with decreasing temperature.

Clinopyroxenes synthesized in experiments with B2 are characterized by a larger compositional variation. At water-saturated conditions clinopyroxenes have an average composition of $En_{42}Fs_{12}Wo_{46}$ ($\pm$ 2.3 mole%; 4.50 wt% bulk water content) which changes continuously with decreasing bulk water content to $En_{48}Fs_{13}Wo_{39}$ ($\pm$ 1.4 mole%; 0.74 wt% bulk water content). In agreement with results obtained for B1, Fs content varies little in water-saturated runs and raises slightly for experiments with $aH_2O < 1$. Orthopyroxenes in equilibrium with the most En-rich clinopyroxenes crystallized at 0.74 wt% bulk water content have the highest Wo contents ($En_{71}Fs_{20}Wo_9 \pm 2.2$ mole%). All other orthopyroxenes vary only little in their mole proportions ($En_{79}Fs_{16}Wo_5 \pm 2$ mole%), showing slight decreasing Fs- and Wo contents with increasing bulk water content.

2.3.4.3. Plagioclase

The effect of bulk water content and temperature on the plagioclase compositions obtained in B1 and B2 (Tab. 2.7) is shown in Figure 2.8. The anorthite content decreases continuously by ~ 0.05 mole%/°C with falling temperature for all bulk water contents. Plagioclase synthesized
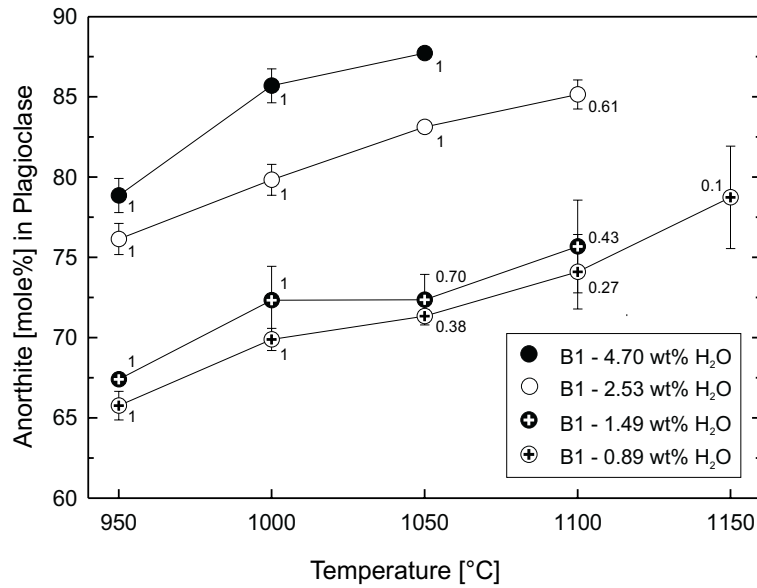
Figure 2.8a Plagioclase composition (B1) as a function of temperature and bulk water content. Error bars correspond to standard deviation of average plagioclase compositions from multiple microprobe measurements. Water contents are given as bulk water contents. Numbers indicate aH_2O of the melt.
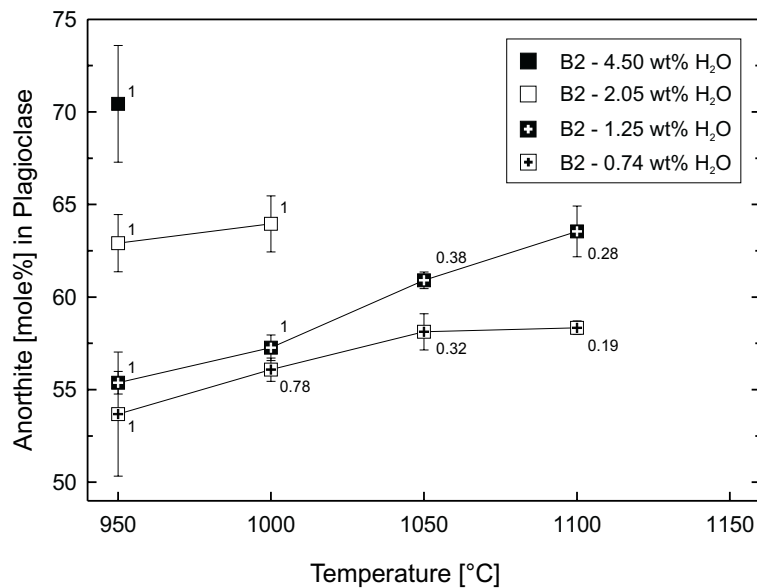
Figure 2.8b Plagioclase composition (B2) as a function of temperature and bulk water content. For abbreviations and detailed comments see Figure 2.8a.

using B1 are generally more An-rich than those crystallized from B2 at similar T-H_2O conditions. The highest An contents of An_{88} (1050 °C) and An_{79} (950 °C) have been obtained for B1 in runs with 4.70 wt% bulk H_2O content (Fig. 2.8a). The most Ab-rich plagioclases (from An_{58} at 1100 °C to An_{54} at 950 °C; Fig. 2.8b) were stable in B2 with 0.74 wt% bulk water content. Plagioclase compositions are systematically more Ca-rich with increasing water content of the melt (in agreement with previous studies of e.g., Turner and Verhoogen, 1960; Scaillet and Evans, 1999; Carmichael et al., 1974; Berndt et al., 2001; Panjasawatwong

et al., 1995; Martel et al., 1998). However, the plagioclase compositions are also systematically more Ca-rich with increasing bulk water content, although the same melt water content (aH$_2$O = 1) has been reached in runs at lower temperatures, independently of bulk water content. In B1, the difference in An content between plagioclases from experiments with the highest and lowest bulk water content (4.70 and 0.89 wt% H$_2$O) is approximately 13 mole% (950 °C) at remains relatively constant for higher temperatures. A difference of 17 mole% is observed in B2 at 950 °C. The Or content in plagioclase is usually below 1 mole% and raises with falling temperature and thus increasing K$_2$O content of the melt (Tab. 2.7).

2.3.4.4. Amphibole

Experimental amphibole analyses of B1 and B2 are listed in Table 2.8. According to the classification of Leake et al. (1997) the synthesized amphiboles are tschermakites except amphiboles obtained in run 37 at 1000 °C which are magnesiohastingsites. The Mg#, (for amphiboles defined as $X_{Mg}/X_{Mg} + X_{Fe}^{2+}$) of amphiboles crystallized in B1 at 950 °C increases (from 0.87 to 1) with increasing bulk water content whereas TiO$_2$ decreases. The number of Si atoms on tetrahedral position of amphiboles synthesized at 1000 °C is lower than that of amphiboles obtained at 950 °C whereas Al^{VI} increases with increasing temperature. This is in agreement with experimental studies of Helz (1981) and Sisson and Grove (1993a). For a given temperature of 950 °C Si and Al^{VI} remain constant at all bulk water contents (Tab. 2.8). Sisson and Grove (1993a) emphasized that the tetrahedral Al^{VI}/Si ratio of amphibole is linearly related to the Al^{VI}/Si ratio of the melt and can be described as $Kd_{Al-Si}^{Am-Melt}$ = $(X_{Al}^{VI}/X_{Si})_{am}/(X_{Al}^{VI}/X_{Si})_{melt}$. An average $Kd_{Al-Si}^{Am-Melt}$ of 1.02 (± 0.09) from coexisting liquid - amphibole pairs obtained in B1 and B2 agrees well with the $Kd_{Al-Si}^{Am-Melt}$ value given by Sisson and Grove (1993a) of about 0.94 (± 0.06) for liquid-amphibole couples in compositions ranging from high-alumina basalt to high-silica rhyolite.

2.3.4.5. Fe-Ti oxides

Owing to the small size of magnetite and ilmenite crystals, analyses of these phases were often contaminated by the surrounding glass. However, analyses were not corrected.

Magnetite of B1 and B2 are characterized by relatively low ulvöspinel contents (X_{Usp}; calculated after Andersen et al., 1993) ranging from 5 to 19 mole%, depending mainly the bulk water content and, to a lesser extent, on temperature. X_{Usp} systematically increases with decreasing bulk water content for all temperatures (Tab. 2.9).

For a given temperature, the difference in X_{Usp} between B1 experiments with different bulk water contents remains relatively constant (e.g., 8 and 9.5 mole% at 1050 °C and 950 °C, respectively, between runs with 4.70 and 0.89 wt% bulk H₂O content). In contrast to B1, magnetite from B2 shows stronger X_{Usp} variation as a function of temperature. At 1050 °C and 950 °C, the difference in X_{Usp} between experiments with 4.50 and 0.74 wt% bulk water content is 14 and 4 mole%, respectively. MgO contents of B1 and B2 magnetite decreases with falling temperature for constant bulk water contents and with decreasing bulk water content for a given temperature. This evolution of MgO content in magnetite is related to Mg# of the melt (melt Mg# is defined as $X_{MgO}/X_{MgO} + X_{FeO}$ x 100; the melt Fe₂O₃ and FeO content is calculated after Kress and Carmichael, 1991). Al₂O₃ content also falls with decreasing temperature for a constant bulk water content.

Ilmenite content (X_{Ilm}; calculated after Andersen et al., 1993) of rhombohedral oxides synthesized in B2 fall regularly with decreasing temperature (from X_{Ilm43} at 1050 °C to X_{Ilm33} at 950 °C for 0.74 wt% bulk water content; Tab. 2.10) and increase systematically at constant temperature with decreasing bulk water content. The same effect of water could be observed for B1 ilmenite crystallized in runs with 0.89 and 1.49 wt% bulk water content at 950 °C, which have generally higher X_{Ilm} than those obtained at similar conditions in B2. Compared with magnetite, MgO, Al₂O₃, and MnO contents in ilmenite are generally lower. As for magnetite, MgO content falls with decreasing bulk water content and temperature.

The results of Bacon and Hirschmann (1988) can be used as a test for coexisting Fe-Ti oxide equilibrium using Mg/Mn partitioning between magnetite and ilmenite. Fe-Ti oxide pairs from B1 and B2 experiments (Tab. 2.2, 2.3) satisfy the Mg/Mn partitioning criterion of Bacon and Hirschmann (1988), having an average magnetite $\log_{(Mg/Mn)}$ of 1.26 ($\pm$ 0.13) and ilmenite $\log_{(Mg/Mn)}$ of 1.40 ($\pm$ 0.08).

2.3.4.6. Glass

Compositions of glasses obtained in B1 and B2 experiments are given in Table 2.11 and the concentrations of SiO_2, TiO_2, FeO*, and MgO are plotted against temperature in Figures 2.9 and 2.10. Depending on experimental conditions, glass compositions range from gabbroic through granodioritic to granitic (run no. 106; classification using TAS diagram after Wilson, 1989).
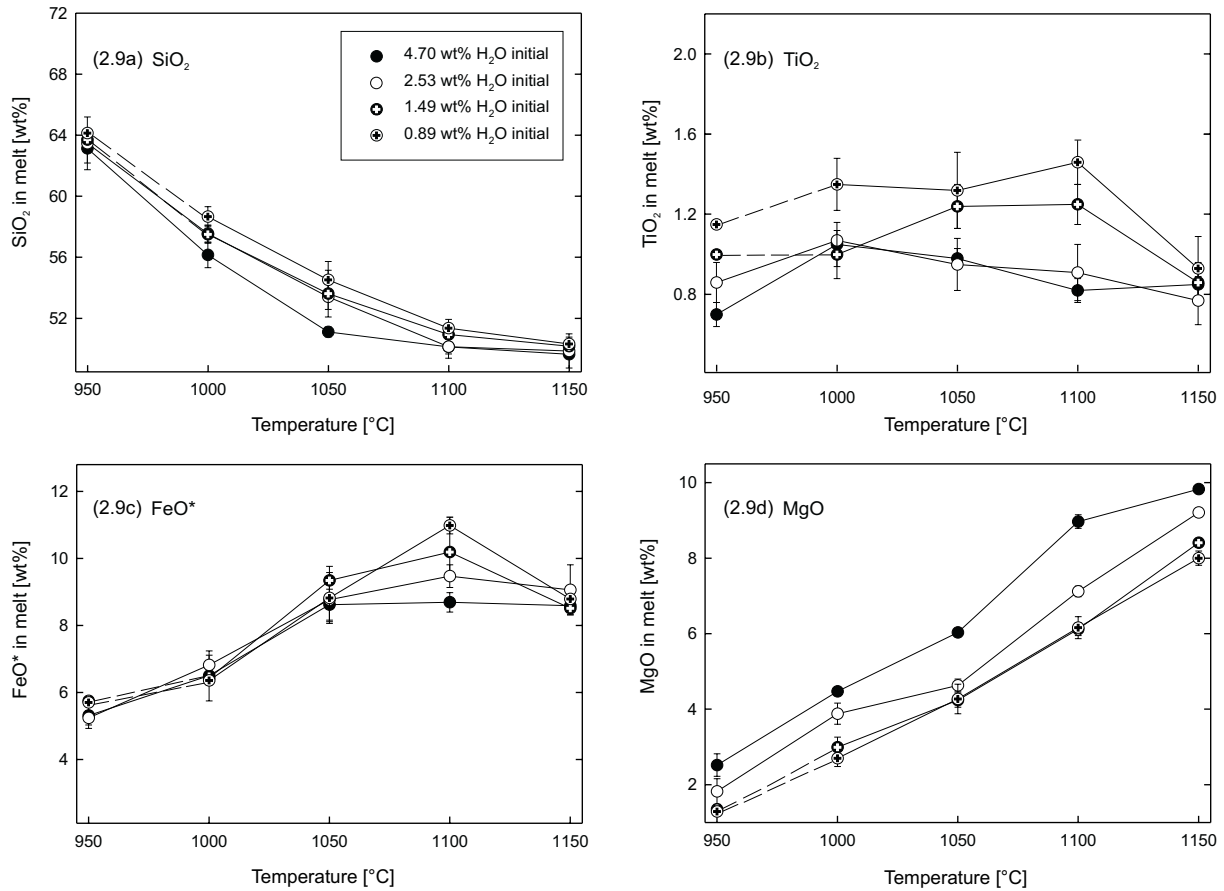
Figure 2.9 B1 melt oxide concentrations of SiO₂, TiO₂, FeO*, and MgO as a function of bulk water content and temperature. Error bars are from standard deviation multiple microprobe measurements (Tab. 2.11). If no errors bars are given, the height of the symbols corresponds to the average error. Note that all analyses are normalized to 100 wt%. Dashed lines indicate calculated melt compositions of experiments no. 47 and 46 (see comments in chapter analytical techniques).

SiO_2, Na_2O, and K_2O concentrations continuously increase for B1 and B2 with falling temperature and decreasing bulk water content. However, when compared with B2, SiO_2 contents of B1 vary only slightly for a given temperature with changing bulk water content (Fig. 2.9a, 2.10a). The maximum SiO_2 concentration is about 64 wt% in B1 and 70 wt% in B2. Despite different initial Na_2O contents of B1 and B2 the same maximum Na_2O concentration of about 5.5 wt% to 4 wt% is reached in both systems for the lowest and highest bulk water contents, respectively (at 950 °C). Because of general low K_2O contents, the increase in K_2O with falling temperature and bulk water content is not as distinct as for SiO_2 and Na_2O, but K_2O increases up to values of 0.75 wt% in B2 (run no. 105; Tab. 2.11).

The MgO and CaO concentrations in glasses from B1 and B2 decrease with decreasing temperature (Fig. 2.9d, 2.10d). In runs with high bulk water contents (4.70 and 4.50 wt% H_2O
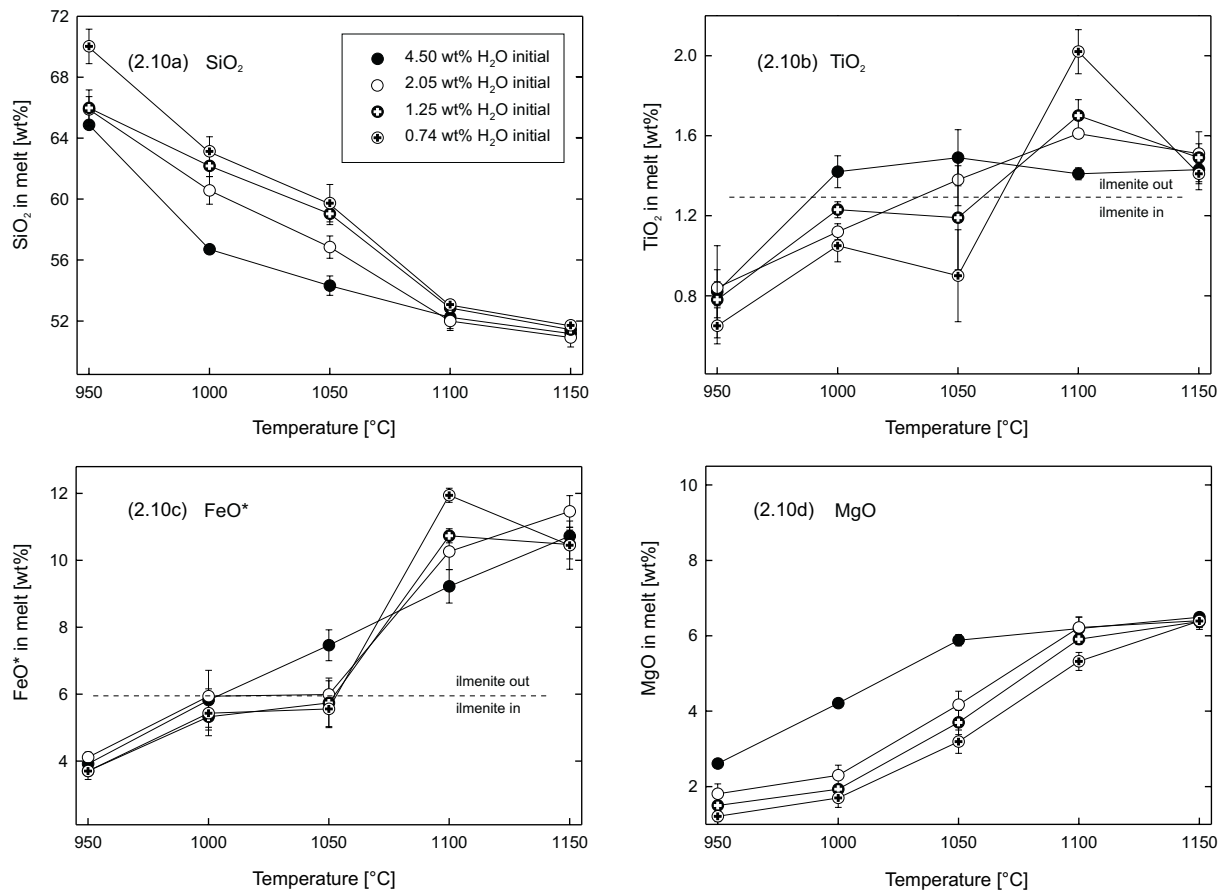

Figure 2.10 B2 melt oxide concentrations of SiO_2, TiO_2, FeO*, and MgO as a function of bulk water content and temperature. For further details see comments of Figure 2.9.

in B1 and B2, respectively), the CaO remains constant (B1) or rises slightly (B2), but decreases once clinopyroxene begins to crystallize. In contrast to SiO$_2$, Na$_2$O, and K$_2$O, for a constant temperature MgO and CaO contents fall with decreasing bulk water content. MgO contents decrease from their initial values of 9.77 wt% (B1) and 6.49 wt% (B2) to a minimum of approximately 2.5 wt% (highest bulk water contents) and 1.2 wt% (lowest bulk water content). Al$_2$O$_3$ contents of B1 and B2 glasses do not vary systematically with bulk water content but show a maximum for B1 and B2 at 1000 °C of about 18.5 wt% and 17.6 wt%, respectively.

As crystallization proceeds, P$_2$O$_5$ concentration in B1 and B2 glasses increases. Due to the low P$_2$O$_5$ concentrations, it is difficult to work out the possible influence of water or temperature on P$_2$O$_5$ contents of residual glasses. It can be noted that the highest P$_2$O$_5$ content in B2 is 0.95 wt% (run no. 102 at 1000 °C).

The TiO$_2$ concentrations in B1 glasses (Fig. 2.9b) decrease with increasing bulk water contents, which can be correlated to the increasing X$_{Usp}$ in magnetite with increasing bulk water content (see above). For given bulk water contents, the TiO$_2$ concentrations first increase and than decrease with falling temperature (Fig. 2.9b). The maximum value is reached at 1100 °C for 0.89 and 1.49 wt% bulk water content and at 1000 °C for 2.53 and 4.70 wt% bulk water content. For B2, Figure 2.10b shows that the TiO$_2$ concentrations at low temperatures are mainly controlled by the crystallization of ilmenite. In all experiments containing ilmenite, the TiO$_2$ concentration is below 1.3 wt%. In addition, TiO$_2$ contents show a general decrease with falling bulk water content and temperature.

The evolution of FeO* content in B1 and B2 glasses is similar to that of TiO$_2$. In B1, the maximum FeO* values are observed at 1100°C (10.19 wt% for 1.49 wt% bulk water content; 10.98 wt% for 0.89 wt% bulk water content; Fig. 2.9c). The FeO* concentration of liquids from experiments with 2.05 and 4.70 wt% bulk water content show only little variation down to 1050 °C (about 8.9 wt%). In B2, FeO* contents of all glasses in experiments containing

ilmenite are below 5.8 wt% (Fig. 2.10c). In addition to the effect of ilmenite, FeO* also decreases with decreasing temperature (for $aH_2O = 1$, 4.5 wt% bulk water) and with increasing water content of the melt (cp. runs at 1100 °C; Fig. 2.10c).

2.4. Discussion

2.4.1. Element Partitioning between Olivine and Melt

2.4.1.1. Mg/Fe Partitioning

Partitioning of Fe and Mg between olivine and melt, expressed as $Kd_{Fe-Mg}^{Ol-Melt}$ (Roeder and Emslie, 1970); defined as $X \frac{Ol-FeO}{Melt-FeO} \times X \frac{Melt-MgO}{Ol-MgO}$), is known to show only small dependence of melt composition, temperature, and fO_2 with a value of about 0.3 ($\pm$ 0.02). The $Kd_{Fe-Mg}^{Ol-Melt}$ determined in this study (at 200 MPa) is slightly higher with an average value of 0.33 ($\pm$ 0.01). This higher value is in agreement with the results of Ulmer (1989), who showed a slight positive pressure dependence of $Kd_{Fe-Mg}^{Ol-Melt}$, thus suggesting that equilibrium conditions between olivine and melt have been reached in our experiments. Although $Kd_{Fe-Mg}^{Ol-Melt}$ is generally assumed to be constant, implying a linear relationship between X_{Fo} and melt Mg#, it is emphasized that small but significant deviations occur as a function of the melt Mg#. This is demonstrated in Figure 2.11 showing that X_{Fo} decreases with the melt Mg# over a wide range of bulk compositions, temperatures, and oxygen fugacities. Toplis and Carroll (1995) observed, in agreement with data of Longhi and Pan (1988) and Shi (1993), that $Kd_{Fe-Mg}^{Ol-Melt}$ values increase up to 0.4 for melt Mg# < 30. This shows the non-ideality of Fe^{2+}-Mg mixing either in the olivine (Wiser and Wood, 1991; Toplis and Carroll, 1995) or in the melt (Hoover and Irvine, 1977), which leads to relative higher Fe^{2+}/Mg ratios in olivine than in the coexisting melt (Fig. 2.11). Our data confirm the non-linear relationship between X_{Fo} and melt Mg# and extend the available database towards high melt Mg#. Using this database (obtained various p, T, aH_2O, fO_2, and bulk compositions), we show that the equilibrium
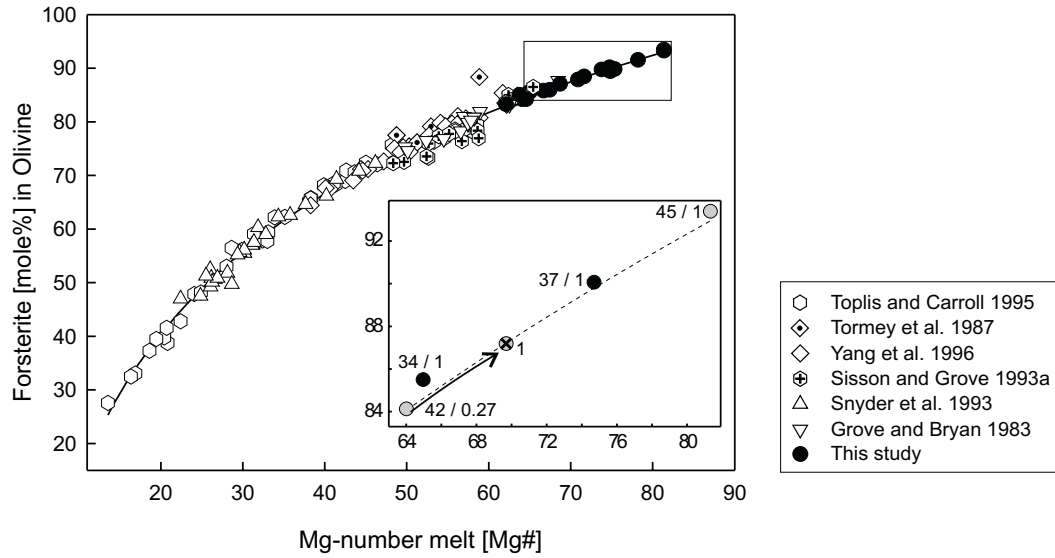
Figure 2.11 The variation of forsterite content (X_{Fo}) of olivine as a function of melt Mg#. Olivine compositions and corresponding melt Mg# from the following studies have been added to the plot: Toplis and Carroll (1995): 1 atm, QFM + 1 to QFM − 2, 1170 − 1050 °C, Ferrobasaltic composition representing parental liquid of Skaergard intrusion; Tormey et al. (1987): only 1 atm experiments were considered, QFM, 1240 − 1152 °C, MORB starting composition dredged near the Kane Fracture Zone; Yang et al. (1996): 1 atm, QFM, 1251 − 1110 °C, six various MORB glasses as starting material; Sisson and Grove (1993a): 200 MPa, NNO, H_2O-saturated, 1050 − 925 °C, high alumina basalts were used as starting material; Snyder et al. (1993): 1 atm, QFM to 0.5 log units above IW, 1192 − 1061 °C, Ferrobasaltic compositions representing parental liquids Newark of Island layered Intrusion, Kiglaplait intrusion and Skaergard intrusion and a tholeiitic composition from Langjökull, Iceland; Grove and Bryan (1983): 1 atm, QFM, 1245 − 1131 °C, four different compositions (primitive basalts from the FAMOUS area, one primitive basalt characterized by "plume-type" geochemistry and one basalt with typical parental composition near the Kane Fracture Zone). Line shows a logarithmic fit to all data describing melt Mg# of corresponding olivine composition for anhydrous to water-saturated basaltic systems crystallizing under low pressure (1 atm − 200 MPa). Insetted plot shows exemplary olivine obtained at 1000 °C (black dots) and 1100 °C (grey dots) from initially water-saturated runs no. 37 and 45 (4.70 wt% H_2O added) and from experiments no. 34 and 42 (0.89 wt% H_2O added). Numbers indicate the experiment number and prevailing aH_2O in the melt (e.g, run no. 37 with aH_2O = 1 is written as 37/1). Arrow marks calculated compositional evolution of olivine with increasing aH_2O from 0.27 to 1 (crossed dot).

compositions of olivine-liquid pairs (plotted in Fig. 2.11) can be described as a logarithmic function of the melt Mg# in the pressure range 0.1 − 200 MPa for both dry and hydrous systems at various fO_2. For a given olivine composition, melt Mg# can be calculated with the following equation:

$$x = e^{\left(\dfrac{y + 68.17}{36.7}\right)} + 0.76 \qquad [1]$$

where x is Mg# of the melt and y is mole% forsterite (X_{Fo}) in olivine.

2.4.1.2. Individual Effect of fO_2 and aH_2O on Olivine and Melt Compositions

Although there is a complex interaction between fO_2 and aH_2O in our experiments, it is possible to distinguish the individual effects of H_2O and fO_2 on olivine composition. The

comparison of olivine compositions obtained in experiments no. 34 and 37 (1000 °C, aH$_2$O = 1, identical fO$_2$) shows that X$_{Fo}$ decreases from 90.07 to 85.50 with decreasing bulk water content from 4.70 to 0.89 wt%. This example shows that a variation of the bulk water content results in a maximum variation of X$_{Fo}$ in olivine of ~ 5 mole% with a corresponding variation of melt Mg# of 10 mole% (decreasing Mg# from 74.69 to 64.96; see inset Fig. 2.11 and Tab. 2.11).

Experiment no. 42 has been used to estimate the effect of fO$_2$ on X$_{Fo}$ resulting from a variation of aH$_2$O (at a given temperature of 1100 °C). In this experiment aH$_2$O is 0.27, log fO$_2$ was calculated to be –6.17 and melt Mg# is 64 (inset Fig. 2.11). For the same temperature and melt composition at aH$_2$O = 1, the log fO$_2$ would be –5.03. It is known that melt Mg# increases with increasing fO$_2$ (Kress and Carmichael, 1991) and melt Mg# should be 69.68 at log fO$_2$ = –5.03 (FeO/Fe$_2$O$_3$ content of the melt and thus melt Mg# calculated after Kress and Carmichael, 1991). Thus, increasing the melt water content by 2.8 wt% H$_2$O (aH$_2$O from 0.27 to 1) results in an increase of melt Mg# of 5.68. Using the inverse function of equation [1], this increase in melt Mg# results in an increase of X$_{Fo}$ of 3.1 mole% (for an increase of ΔMg# = 5.68). This theoretical olivine-melt compositional pair for 1100 °C and aH$_2$O = 1 is reported in Figure 2.11 (crossed circle).

The olivine composition for 1100 °C and 4.70 wt% bulk water content (aH$_2$O = 1) is also included in Figure 2.11 (run no. 45). It can be noted that the compositional difference between the theoretical X$_{Fo}$ value calculated above (87.2) and run no. 45 (93.2) is identical to that between X$_{Fo}$ in runs no. 34 and 37 (~ 5 mole%; aH$_2$O = 1; see above). This confirms that the effect of fO$_2$ (via variation of aH$_2$O) on X$_{Fo}$ calculated above is realistic. In conclusion, during differentiation at buffered fO$_2$, increasing aH$_2$O in the melt results in an increase of melt Mg# and therefore X$_{Fo}$ as a result of two processes: 1. increasing melt fraction and 2. increasing fO$_2$.

2.4.1.3. Ca Partitioning between Olivine and Melt

Calcium partitioning between olivine and melt and its dependence on p, T, fO$_2$, and bulk composition has been the object of numerous studies. It is generally accepted that neither oxygen fugacity nor temperature and pressure directly influence the Ca partitioning (Roeder, 1974; Watson, 1979; Libourel, 1999; Jurewicz and Watson, 1988; Longhi et al., 1978). As demonstrated recently by Libourel (1999), Ca concentration in olivine depends strongly on olivine compositions as well as on alkali and alumina content of the melt. Generally, partition
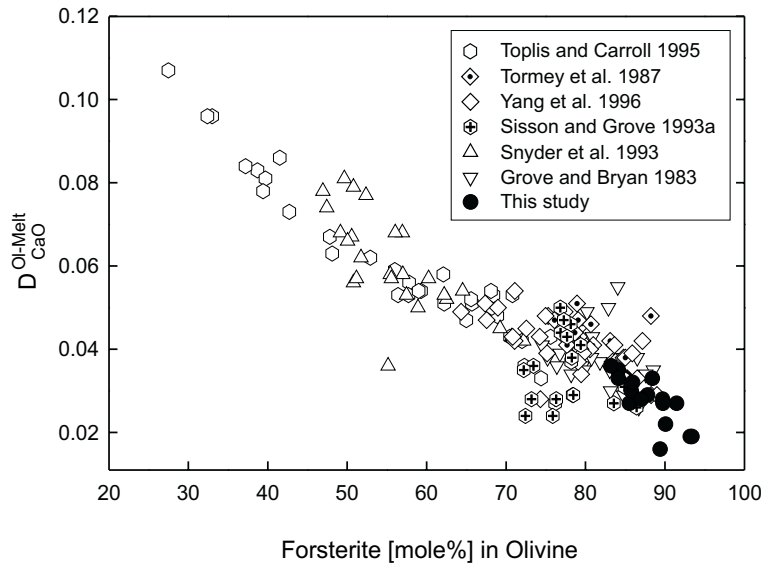
Figure 2.12a $D_{CaO}^{Ol-Melt}$ versus the forsterite content of olivine. Added data for various natural basaltic compositions from other studies as in Figure 2.11. Error for $D_{CaO}^{Ol-Melt}$ is typically $\pm$ 0.004 and has been obtained from error propagation calculating $D_{CaO}^{Ol-Melt}$ from standard deviation of CaO concentrations in olivine and melt. Errors of olivine compositions are given in Figure 2.12b.
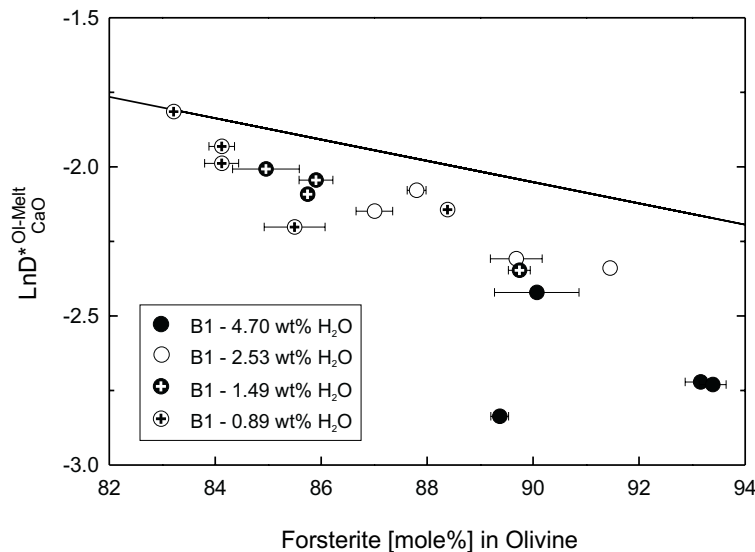
Figure 2.12b Calculated $LnD*_{CaO}^{Ol-Melt}$ values for olivine-melt pairs obtained in this study after the model of Libourel (1999). Solid line shows $LnD*_{CaO}^{Ol-Melt}$ trend calculated using an empirical function of Libourel (1999) which describes $LnD*_{CaO}^{Ol-Melt}$ values of olivine-liquid pairs obtained in dry systems. Error bars of olivine composition correspond to standard deviation of average olivine compositions.

coefficient $D_{CaO}^{Ol-Melt}$ ($CaO_{Olivine}/CaO_{Melt}$, in wt%) increases with decreasing X_{Fo} and increasing melt alkali and CaO content (Fig. 2.12a). Figure 2.9a shows $D_{CaO}^{Ol-Melt}$ versus X_{Fo} obtained in this study. As expected from the generally high X_{Fo} and low melt alkali content, Ca concentration in olivine is typically low in our system. Comparison with other data from experimental studies on more iron-rich, tholeiitic, and other basaltic systems confirm $D_{CaO}^{Ol-Melt}$ values obtained in this study suggesting equilibrium conditions with respect to Ca partitioning between olivine and melt.

Based on experimental data, Libourel (1999) developed a model which provides an empirical Ca partition coefficient $LnD*_{CaO}^{Ol-Melt}$ taking into account the effect of melt and olivine composition. Thus, modeling Ca partitioning between olivine and melt allows to predict Ca contents in olivine during magmatic differentiation or Ca contents of the melt for a given olivine composition. However, the application of the model of Libourel (1999) on our data does not systematically reproduce the predicted Ca partitioning (Fig. 2.12b).

Experimental data obtained at low aH_2O and with high SiO_2 content of the melt (maximum values of 59 wt%; Tab. 2.11) are consistent with the model of Libourel (1999). The maximum deviation from the modeled Ca partitioning trend is observed for melts containing high water contents and low SiO_2 (Fig. 2.12b). A possible explanation for this observation is that water influences partitioning of Ca between olivine and melt, which has not been considered in the model of Libourel (1999) since all experimental data were obtained in dry systems.

As emphasized by Libourel (1999), Ca incorporation in olivine depends on the structural position of Ca in the melt. In anhydrous melts, Ca is usually considered as a network modifying cation following the reaction SiOSi + CaOCa = 2CaOSi and Libourel (1999) has assumed this incorporation mechanism. In hydrous aluminosilicate glasses, Behrens and Schulze (2000) reported a strong decrease of water diffusivity with increasing Ca content of the melt. They concluded that Ca forms complexes with OH groups and H_2O molecules and is thus strongly bonded with the hydrous species. Hence, the activity of Ca incorporated as Ca-O-Si species can be lowered in basaltic systems by the presence of water, resulting in lower

Ca concentrations in olivine. This is confirmed by our results showing the highest discrepancy between experimental and calculated $LnD*_{CaO}^{Ol-Melt}$ for water-saturated SiO_2-poor melts. This discrepancy is lower for SiO_2-rich melts, because the high SiO_2 content favors the formation of CaOSi species in the melt. These observations indicates that the Ca content of olivine can be potentially used as a hygrometer in basaltic melts if the coexisting equilibrium anhydrous melt composition is known.

2.4.2. Effect of aH$_2$O on Plagioclase Composition

Plagioclase is one of the most common phases in igneous rocks, and its composition and stability depends on p, T, and bulk composition and also on H_2O content of the melt (e.g., Turner and Verhoogen, 1960; Holloway and Burnham, 1972; Scaillet and Evans, 1999; Carmichael et al., 1974; Panjasawatwong et al., 1995; Martel et al., 1998). It has been shown that MORB´s may contain significant amounts of H_2O (e.g., Sobolev and Chaussidon, 1996; Danyushevsky et al., 1996; Kovalenko et al., 2000) and understanding the effect of H_2O on plagioclase stability and composition is of importance to interpret crystallization processes in MORB.

Direct influence of H_2O on plagioclase-liquid equilibrium compositions is shown in Figure 2.13. For a constant Ca/Na ratio of the melt, the An content of plagioclase obtained at water-saturated conditions (4.55 – 5.25 wt% H_2O in melt) is noticeably higher compared with An contents in plagioclases in runs with about 2 wt% H_2O in melt. Consequently, $Kd_{Ca-Na}^{Pl-Melt}$ (defined as $(Ca/Na)_{Plagioclase}$ / $(Ca/Na)_{Melt}$) increases with increasing aH$_2$O of the melt. Solid lines in Figure 2.13 indicate $Kd_{Ca-Na}^{Pl-Melt}$ values given by Sisson and Grove (1993a) for plagioclase-melt pairs obtained in high-alumina basalts with 4 wt% H_2O in the melt (at 100 MPa , $Kd_{Ca-Na}^{Pl-Melt} \sim 3.4$, Data from Sisson and Grove, 1993b) and 2 wt% H_2O in melt (at 200 and 500 MPa, $Kd_{Ca-Na}^{Pl-Melt} \sim 1.7$, Data from Baker and Eggler, 1987). As emphasized by Sisson and Grove (1993a), it should be noted that the pressure dependence of $Kd_{Ca-Na}^{Pl-Melt}$ in dry systems in the range 1 atm to 20 MPa is always significantly lower than the influence of
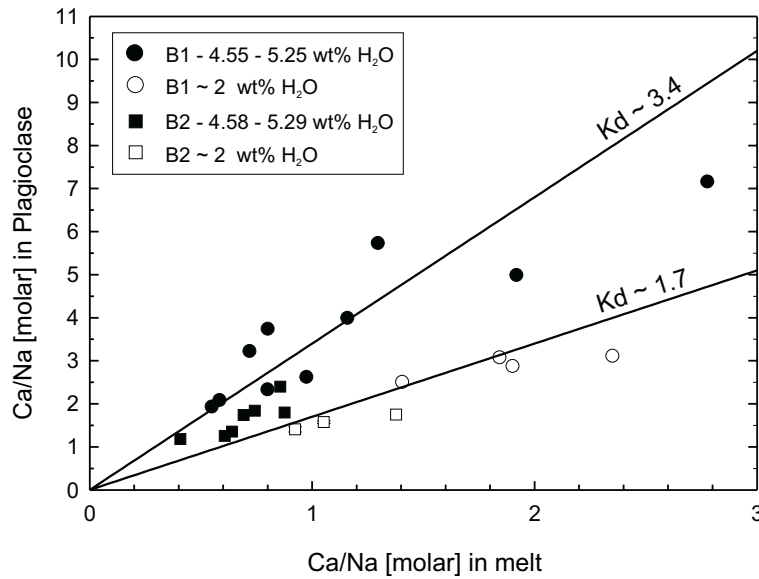
Figure 2.13 Ca/Na ratios for plagioclase-melt pairs (B1 and B2) obtained at water-saturated conditions (aH$_2$O = 1, melt water contents calculated after Burnham (1979) and approximately 2 wt% H_2O in melt. Solid lines show $Kd_{Ca-Na}^{Pl-Melt}$ after Sisson and Grove (1993a) for plagioclase-melt pairs in high-alumina basalt (Sisson and Grove, 1993b; at 100 MPa and about 4 wt% H_2O in melt ($Kd_{Ca-Na}^{Pl-Melt}$ ~ 3.4) and about 2 wt% H_2O in melt at 200 and 500 MPa (Baker and Eggler, 1987; ($Kd_{Ca-Na}^{Pl-Melt}$ ~ 1.7).

water. Thus, it is assumed that variations between 100 and 500 MPa are negligible. $Kd_{Ca-Na}^{Pl-Melt}$ values obtained in this study for given melt water contents over a wide range of liquid compositions (from gabbroic to granitic, see above) agree well with data of Sisson and Grove (1993a), Sisson and Grove (1993b), and Baker and Eggler (1987) for high-alumina basalts. This confirms that plagioclase composition mainly depends on aH$_2$O and melt Ca/Na ratio and is widely independent of bulk composition of the system.

Compared with experimental studies in dry systems (e.g. Toplis and Carroll, 1995), the An content of plagioclase obtained in our study decreases only by about 0.05 mole%/°C (cp. 0.5 mole%/°C in the study of Toplis and Carroll, 1995) for a given bulk water content with decreasing temperature (Fig. 2.8), although a strong concomitant depletion in melt Ca/Na ratio content is observed. As discussed above, in water-bearing systems, for a given bulk water content, increasing crystal fraction (due to decreasing temperature) results in an increase of melt water content (see aH$_2$O evolution in Fig. 2.8). Thus, the effect of decreasing Ca/Na in melt on An content of plagioclase with progressive crystallization (resulting in a strong decrease of An content in dry systems) is partly compensated by progressive increase of melt water content in hydrous systems.

It can be noted that after reaching water-saturated conditions in all experiments due to decreasing temperature and increasing crystal fraction (in B1 at 1000 °C, in B2 at 950 °C;

Fig. 2.8a, b), plagioclase compositions are still more An-rich in runs with high bulk water content (despite identical p, T, fO$_2$, and aH$_2$O). This is the result of different coexisting residual melt compositions. In experiments with high crystal fraction (low bulk water content) melts are more evolved and plagioclases are less An-rich. This shows that the bulk water content of a system can also control plagioclase composition in differentiation processes, despite all extensive parameters are equal.

2.4.3. Effect of aH$_2$O on Fe-Ti oxide Compositions

The influence of Fe-Ti oxides on the differentiation of basaltic systems has been investigated by numerous authors (e.g., Hill and Roeder, 1974; Grove and Baker, 1984; Thy and Lofgren, 1994; Toplis and Carroll, 1995; Juster et al., 1989; Snyder et al., 1993). It is generally accepted that the concentrations of iron and silica in the melt are sensitive to the crystallisation of Fe-Ti oxides and it has been shown (e.g., Toplis and Carroll, 1995) that fO$_2$ greatly influences the stability of Fe-Ti oxides.

H$_2$O is not known to have a direct influence on Fe-Ti oxide composition. However, due to the variation of fO$_2$ with aH$_2$O, Fe-Ti oxide compositions are influenced by the H$_2$O concentration of the melt, too. As discussed above, the magnetite/ilmenite pairs analyzed in this study have equilibrium compositions (Bacon and Hirschmann, 1988). Thus, the calculated fO$_2$, applying the oxide geothermobarometer (e.g., Andersen et al., 1993) to the Fe-Ti oxide pairs for a known temperature, should correspond to values measured by the solid redox sensor technique (Taylor et al., 1992). As shown in Figure 2.1, the calculated fO$_2$ for Fe-Ti oxides at aH$_2$O = 1 agree well with fO$_2$ values obtained by the solid sensor method of (Taylor et al., 1992) and confirm the intrinsic MnO-Mn$_3$O$_4$ buffer conditions prevailing in the IHPV. Magnetite/ilmenite pairs crystallized in runs with aH$_2$O < 1 show lower calculated fO$_2$ values than those obtained at water-saturated conditions (Fig. 2.1; Tab. 2.2, 2.3). This confirms that H$_2$O can significantly influence the composition of iron-bearing phases by influencing the fO$_2$ in the system.

2.4.4. Effect of H$_2$O on Phase Stability, Phase Proportions, and Liquid Lines of Descent

The addition of H$_2$O to a silicate system is not only influencing the composition of phases but also greatly influences phase stability and proportions. As discussed above, the increasing crystal fraction with falling temperature leads to water-saturated conditions (aH$_2$O = 1) in all experiments (Fig. 2.4a, b). Hence, it could be expected that for a given temperature (e.g., 1000 °C in B1), all other parameters being equal (p, T, bulk composition, fO$_2$, and aH$_2$O), the phase assemblage should be identical. This is not the case because melt proportion and the relative proportions of minerals (Fig. 2.5, 2.6), and therefore melt compositions (Fig. 2.9, 2.10) differ as a function of the bulk water content. This, in turn, influences the compositions and stability of solid phases and liquid lines of descent. For example, in B1 experiments at 1000 °C, orthopyroxene is only stable at low bulk water contents (0.89 and 1.49 wt% H$_2$O) and the stability of amphibole is reached only at the highest bulk water content of 4.70 wt% (Fig. 2.4a). In the following parts, the individual effect of H$_2$O on phase stability, modal proportion, and its influence on liquid line of descent is discussed.

Owing to the importance of olivine in igneous differentiation processes of basaltic systems special attention must be drawn to its behavior with respect to water content of the melt. H$_2$O is known to depolymerize melts and thus enhance the stability field of depolymerized phases like olivine (e.g., Kushiro, 1975; Ulmer, 1989). In order to understand the evolution of the stability field of olivine as a function of water, the texture and modal proportions of this mineral in experimental products can be used (Toplis and Carroll, 1995). The highest proportions of olivine in B1 is reached at 1050 °C for all bulk water contents (Tab. 2.2; Fig. 2.5). At this temperature, olivine textures change from euhedral to rounded crystals indicating the beginning resorption of these phases. This is supported by the decreasing olivine abundance estimated by mass balance calculations at temperatures below 1050 °C. Toplis and Carroll (1995) made similar observations for olivine in a dry ferrobasaltic system at slightly higher temperatures (1070 – 1130 °C) for fO$_2$ in the range QFM +1 to QFM –2. Toplis and Carroll (1995) observed a decreasing onset temperature of olivine resorption with

decreasing fO_2. However, onset of olivine resorption in our study is observed at lower temperatures despite fO_2 is higher than in the study of Toplis and Carroll (1995). A possible explanation is that the higher depolymerization of our hydrous melts leads to increasing stability and activity of olivine (e.g., Kushiro, 1975). This is supported by the study of Spulber and Rutherford (1983) showing that olivine is stable in a MORB composition (DO8) until solidus is reached at low fO_2 (G-CH buffer) and hydrous conditions (aH_2O ~ 0.6) suggesting that the olivine stability field is extended to lower temperatures with decreasing fO_2 and increasing aH_2O in basaltic systems.

Discussing the stability of olivine requires to turn one's attention to the appearance of orthopyroxene in B1 and B2 run products. As emphasized by Juster et al. (1989) and Toplis and Carroll (1995), high silica activities of the melt promote resorption of olivine involving a reaction of the type $Mg_2SiO_4^{ol} + SiO_2^{glass} = 2MgSiO_3^{pig}$. In B1, orthopyroxene saturation curve (opx-in curve; Fig. 2.3a) and olivine out curve are not identical, but overlap at 1000 °C and 0.89 and 1.49 wt% bulk water content. Since the resorption of olivine roughly parallels the crystallization of orthopyroxene, it can be assumed that the occurrence of orthopyroxene is related to a reaction as described above. Furthermore, orthopyroxene crystallizes first in runs with lower bulk water contents and thus higher crystal fraction and silica activity of the melts. In the fractionated B2 composition, olivine is absent. Therefore, the general higher melt SiO_2 contents of the more evolved B2 compositions expand the stability field of orthopyroxene particularly at low aH_2O up to 1050 °C.

Stability of plagioclase as a function of water has been widely discussed (Helz, 1973; Holloway and Burnham, 1972; Spulber and Rutherford, 1983; Sisson and Grove, 1993a; Panjasawatwong et al., 1995). In agreement with previous studies, the proportions of plagioclase relative to mafic phases are depressed with increasing bulk water content in B1 and B2 (Fig. 2.5, 2.6). This is related to the higher An content of plagioclases coexisting with water-rich melts (less plagioclase needs to crystallize to adjust the melt CaO content). In contrast to observations of Spulber and Rutherford (1983), Beard and Lofgren (1991), and

Gaetani et al. (1993) no Al$_2$O$_3$ enrichment with increasing bulk water content due to the depression of plagioclase could be detected. A possible explanation is that the increasing An content of plagioclase with increasing bulk water content in combination with the general high An plagioclases in this study (Fig. 2.8) counteract the relatively lower proportions of plagioclase at high water contents of the system.

The occurrence of amphibole in natural systems is often used to characterize whether magmas were "dry" or hydrous in a broadly qualitative sense. Our results support previous experimental findings in hydrous basaltic and calc-alkaline systems (e.g., Helz, 1973; Holloway and Burnham, 1972; Spulber and Rutherford, 1983; Sisson and Grove, 1993a; Johnson et al., 1994) showing that a relatively high amount of H$_2$O in the melt is necessary to stabilize amphibole (~ 5 wt% in our study). In our study the stability field of amphibole is always restricted to runs with aH$_2$O = 1 (Fig. 2.3) but not all experiments performed under water-saturated conditions contain amphibole. This suggests that the amphibole stability is also very sensitive to melt composition (amphibole crystallizes at higher temperature for high CaO content of the melt). Thus, in differentiation processes the conditions at which amphibole starts to crystallize is controlled by both the aH$_2$O and the initial bulk water content of the system.

The effect of H$_2$O on stability of Fe-Ti oxides has been the object of interest in several studies (e.g., Helz, 1973; Holloway and Burnham, 1972; Grove and Baker, 1984; Baker and Eggler, 1987; Sisson and Grove, 1993a) due to the significant influence of oxide stability on liquid line of descent. For calc-alkaline systems, Sisson and Grove (1993a) emphasized that Fe-Ti oxides crystallize are formed earlier in the crystallization sequence of hydrous melts compared to dry systems.

Consequently, hydrous residual melts follow a different liquid line of descent which is typical for the calc-alkaline trend characterized by an early FeO* depletion. For the dry systems, oxide saturation will occur at lower temperatures resulting in a more tholeiitic differentiation trend, characterized by an enrichment in FeO* in residual melts. Our results show that this

assumption is oversimplified and that the compositional trends are dependent on the nature of fractionated oxides (either magnetite or ilmenite). Ilmenite stability depends mainly on melt TiO_2 content (Fig. 2.10) and is less dependent melt oxidation state (Thy and Lofgren, 1994; Toplis and Carroll, 1995). The saturation curve of ilmenite which can be observed in Figure 2.4b is a result of decreasing temperature and of increasing TiO_2 content of the melt with increasing crystal fraction. Thus, because the melt fraction increases with bulk water content, ilmenite saturation is indirectly influenced by H_2O.

In contrast, magnetite stability in 1 atm experiments depends strongly on fO_2 (Roeder, 1974; Hill and Roeder, 1974; Grove and Juster, 1989; Toplis and Carroll, 1995; Juster et al., 1989; Snyder et al., 1993). In addition, Sisson and Grove (1993a) emphasized that magnetite stability is also enhanced by H_2O. The effect of H_2O on magnetite stability in B1 is demonstrated in Figure 2.4a. This figure shows that magnetite is indeed stable at high temperature when fO_2 is high, but that magnetite saturation is independent on aH_2O and bulk water content. In B2, magnetite is not stable at 1150 °C and 4.5 wt% bulk water content but in all experiments performed at the same temperature with lower bulk water contents. This also indicates that stability of magnetite in MORB is not enhanced by H_2O. This observation is also confirmed by results of Spulber and Rutherford (1983) for hydrous MORB composition. The Fe-Ti oxides in their experiments conducted at high water activities under the G-CH buffer show only a very restricted stability field and were not stable until 955 °C at 200 MPa. Thus, our data and those of Spulber and Rutherford (1983) indicate that water does not affect the stability of magnetite, in contrast to the assumption of Sisson and Grove (1993a) for a calc-alkaline system.

2.4.5. Fractionation Effects

To understand the differentiation processes of basaltic systems it should be borne in mind that a perfect fractional crystallization path requires a continuous removal of solids from the systems. In our study we have investigated two compositions, B1 and B2, B2 being representative of the residual melt obtained in B1 after 50 wt% crystallization and a bulk

water content of 0.89 wt%. Thus, only one fractionation step has been carried out. This fractionation event is far to be representative of natural fractionation steps but can show exemplary the influence of fractionation on liquid line of descent and phase relations.

Experimental results from the evolved B2 composition show that phase relations are different from B1 (Fig. 2.4). Magnetite is the liquidus phase in B2 due to the high fO₂ and the melt Fe_2O_3 content, which is higher than in B1. Thus, saturation temperature of magnetite is increased in B2. Stability fields of both, orthopyroxene and ilmenite, are enhanced as a result of the absence of olivine and of general higher melt TiO_2 concentrations, respectively. Furthermore, the stability field of amphibole is depressed probably resulting from the lower melt CaO contents. The lines of equal aH₂O are shifted to lower temperatures because of the general crystal fraction in B2 (Fig. 2.4b). Mineral and melt compositions produced in B2 are different compared to B1 and are consistent with equilibrium compositions in more evolved systems. Our results also show that starting with a primitive MORB, a quartz-dioritic melt can be obtained without any fractionation (e.g., B1, 12.6% melt fraction, run no. 48), and a trondhjemitic (granitic) melt can be obtained by at least one fractionation step (B2, 14% melt fraction, run no.106).

However, despite the major difference in phase relations and mineral compositions in B1 and B2, liquid line of descent shows generally the same trend for both compositions (cp. Fig. 2.9 and 2.10). This supports the assumption that liquid lines of descent obtained by perfect equilibrium and perfect fractional crystallization are similar over a wide crystallization path, as emphasized by theoretical considerations of Toplis and Carroll (1996) for ferrobasaltic systems. Nevertheless, our study shows that phase relations can be greatly influenced by one fractionation step.

2.5. Conclusions

Experimental results of this study show the effect of H₂O on the phase relations in a primitive MORB system under high fO₂. H₂O is found to have a large influence on solid phase compositions and stability. It has been demonstrated that changing aH₂O also influences

significantly the Mg/Fe ratio in iron-bearing phases like olivine as a result of changing fO₂. Furthermore, our data suggest that partitioning of CaO between olivine and melt also depends on melt water content. This is due a possible stabilization of Ca in hydrous melts when compared to dry liquids leading to lower $D_{CaO}^{Ol-Melt}$ values for olivine crystallizing under hydrous conditions. As well as for olivine, increasing aH₂O influences Fe-Ti oxide compositions by raising the fO₂ of the charge. $Kd_{Ca-Na}^{Pl-Melt}$ values for plagioclase obtained in this study for given melt water contents agree well with previous data (e.g., Sisson and Grove, 1993a) confirming that plagioclase composition mainly depends on melt water content and Ca/Na ratio of the system.

Liquid lines of descent for both investigated starting compositions B1 and B2 differ slightly from each other, but show similar trends. At a given temperature, melt fraction is strongly controlled by the bulk water content and is always higher in systems with high bulk water contents, even if water-saturated conditions are prevailing. We confirm that high melt water contents need to be reached for the crystallization of amphibole (about 5 wt%), but the stability of amphibole depends also on anhydrous melt composition (Helz, 1973; Holloway and Burnham, 1972; Spulber and Rutherford, 1983; Sisson and Grove, 1993a). Concerning the crystallization of Fe-Ti oxides, there is no evidence that aH₂O and bulk water content increase the stability of magnetite. The occurrence of this mineral is enhanced by high fO₂ only in contrast to ilmenite which is also dependent on the proportion of the prevailing phases (and thus bulk water content). We confirm that high fO₂ will avoid a strong FeO* enrichment of the residual melts during differentiation.

Phase relations, crystallization sequence, and mineral compositions obtained from evolved melt compositions of MORB systems after 50 wt% crystallization are different from the

primitive MORB composition. In detail, the liquid lines of descent differ slightly (higher SiO_2 contents of melts are reached at identical p, T, aH$_2$O). However, the general compositional trends of residual melts obtained in both compositions are very similar.

3. Differentiation of Hydrous MORB at QFM–Buffer Conditions and 200 MPa: Implications for Fe-Ti Oxide Stability and Liquid line of Descent in MORB

3.1. Introduction

The trend of liquid composition in differentiation of a basaltic magma under crustal pressure and temperature conditions has been object of interest in many experimental studies. It is generally accepted that fO$_2$ (oxygen fugacity) is a critical parameter controlling the crystallization of Fe-Ti oxides in iron-bearing systems. As shown by e.g. Osborn (1959), Presnall (1966), Toplis and Carroll (1995), and Snyder et al. (1993) in 1 atm experiments for basaltic compositions, magnetite stability is enhanced at high fO$_2$ resulting in an early depletion of FeO* (total iron) and enrichment of SiO_2 in residual melts. Thus, these melt compositions show generally a tendency to follow a calc-alkaline differentiation trend (e.g., Miyashiro, 1974; Irvine and Baragar, 1971). At moderate (about NNO-QFM buffer) to low oxygen fugacities the liquid line of descent derived from experiments in basaltic systems are generally characterized by an early FeO*/MgO, and to a lesser extent, SiO_2 enrichment following a tholeiitic differentiation trend (e.g., Grove and Baker, 1984; Toplis and Carroll, 1995; Juster et al., 1989; Snyder et al., 1993). As outlined in chapter 2 H$_2$O is known to have a strong influence on phase relations in mafic systems and the effect of H$_2$O on the differentiation trend of primitive MORB´s at moderate pressure (100 - 200 MPa) is widely unknown. To the authors knowledge, experiments in this compositional systems and pressure

range have only been carried out by Spulber and Rutherford (1983), but in this study aH_2O (water activity) was not varied systematically.

Holloway and Burnham (1972) and Sisson and Grove (1993a) emphasized that typical calc-alkaline differentiation trend can be obtained at geologically relevant fO_2 if water is present in this systems because it promotes the early crystallization of Fe-Ti oxides. As shown in chapter 2 it can be confirmed that magnetite appears early in the crystallization sequence of a hydrous primitive MORB composition at high fO_2 ($MnO-Mn_3O_4$ buffer). However, in contrast to the assumptions of Sisson and Grove (1993a) the stability of magnetite was not found to be dependent of the ambient aH_2O. Experimental results of Spulber and Rutherford (1983) also show that oxide stability is not necessarily enhanced at high aH_2O since Fe-Ti oxides were not stable until 955 °C at 200 MPa in their study.

The two studies in hydrous MORB systems mentioned above have not been conducted at those fO_2, which are supposed to be relevant during the differentiation of MORB in nature. The experiments of Spulber and Rutherford (1983) were performed at the G-CH buffer, which is much lower than the fO_2 range prevailing in natural MORB magma reservoirs. On the other hand, the experiments performed at high fO_2 (see chapter 2) are useful to understand the role of aH_2O on phase relations and compositions, but the ambient fO_2 conditions of their experiments are too oxidizing for reliable comparison with nature. Since the fO_2 of natural MORB lavas was found to vary generally between QFM-2 and QFM+1 (e.g, Carmichael and Ghiorso, 1986; Christie et al., 1986), we performed equilibrium crystallization experiments under redox conditions corresponding to the QFM buffer in the temperature range 1150 °C – 950 °C. As experimental pressure of this study 200 MPa was chosen in order to represent the pressures of typical reservoirs of MORB magma which occur in Mid-ocean ridge system at shallow crustal levels at depth between 3 and 6 km (e.g., Fisk, 1984; Nicolas, 1989).

Our knowledge about the real water contents in natural MORB magmas undergoing differentiation is poor. For primitive, normal MORB, Sobolev and Chaussidon (1996),

Kovalenko et al. (2000), and Danyushevsky et al. (2000) determined water contents with average values of about 0.31 increasing up to 0.5 wt%. Moreover, since during the main stage of MORB crystallization only anhydrous minerals are formed, it is expected that the $a\mathrm{H_2O}$ will increase during differentiation. For a better understanding of the role of water during differentiation of MORB, the initial water content of our experimental system was varied systematically ranging from 0.35 wt% to 4.46 wt% $\mathrm{H_2O}$. The results are used to estimate the influence of $\mathrm{H_2O}$ (and $f\mathrm{O_2}$) on stability of Fe-Ti oxides and MORB liquid line of descent.

3.2. Experimental and Analytical Methods

3.2.1. Starting Material and Experimental Procedure

The starting material is the primitive 10-component MORB glass B1 used for experiments at high $f\mathrm{O_2}$ (see Tab. 2.1 in chapter 2). We performed crystallization experiments with B1 glasses containing different amounts of $\mathrm{H_2O}$.

Before using the B1 glass as starting material the glass was equilibrated in an 1 atm gas mixing furnace ($\mathrm{H_2/H_2O}$) at the desired $f\mathrm{O_2}$ of the experiments. For the experiments at relatively high temperatures between 1150 and 1050 °C, these glasses were loaded in iron pre-saturated $Au_{80}Pd_{20}$ capsules (see below) and the desired amount of water was added to the sample container (typically 100 mg glass and 0.35 to about 7 wt% $\mathrm{H_2O}$). The sealed capsules were brought directly to the final run temperature (for detailed information see chapter 2).

For lower run temperatures of 1000 °C to 950 °C this experimental procedure led to disequilibrium effects due to the fast crystallization in these low-viscosity systems before reaching a homogeneous distribution of the added water in the anhydrous B1 glass powder. Therefore, hydrous glasses with defined bulk water contents have been synthesized at 200 MPa, 1250 °C and a log $f\mathrm{O_2}$ = QFM (for control of $f\mathrm{O_2}$ see below). The water contents of the homogeneous crystal- and bubble free glasses were measured by Karl-Fischer-Titration (KFT; e.g., Behrens, 1995) and are given in Table 3.1 (bulk water contents of experiments performed

at 1000 and 950 °C). These hydrous glasses were grounded to a powder (100 – 200 µm grain size) and sealed into iron pre-saturated $Au_{80}Pd_{20}$ capsules.

To avoid iron-loss to the sample container (e.g., Johannes and Bode, 1978), $Au_{80}Pd_{20}$ capsules were used because they have a lower Fe-solubility than Pt and a higher melting point than pure Au which allows to perform experiments up to 1250 °C (Kawamoto and Hirose, 1994). Nevertheless, at the reducing redox conditions of our experiments a significant iron loss due to Fe diffusion into the $Au_{80}Pd_{20}$ capsule material was observed. Therefore, the $Au_{80}Pd_{20}$ capsules were presaturated in iron at fO_2 corresponding to the QFM buffer at 200 MPa and

Table 3.1. Experimental conditions and results for composition B1 (QFM buffer)

run	duration [h]	pressure [MPa]	wt% H_2O bulk	wt% H_2O[a] in melt	aH_2O	fH_2O [bar]	log fO_2[b] [bar]	Δ QFM[c] [bar]	phases detected and modal proportions [d, e]					ΣR^2
1150°C														
130	2.2	207.2	6.52[f]	*4.58*[h]	1	2085	-8.51	+0.2	gl(100) fl					
129	2.2	207.2	2.01[f]	2.08	0.33	696	-9.46	-0.75	gl(96.7) ol(3.3)					0.97
128	2	205.7	0.96[f]	1.02	0.10	215	-10.56	-1.85	gl(94.5) ol(5.5)					0.76
127	2	205.7	0.35[f]	0.38	0.02	36	-12.12	-3.41	gl(91.9) ol(5.9)	cpx(0.3)	pl(1.9)			0.83
1100°C														
134	3	202.7	6.41[f]	*4.53*	1	1998	-9.27	+0.09	gl(95.6) ol(4.4) fl					0.45
132	3	204.3	2.00[f]	2.37	0.40	806	-10.15	-0.80	gl(84.4) ol(7.9)	cpx(4.8)	pl(2.9)			0.68
133	3.1	202.7	1.01[f]	1.49	0.20	398	-10.67	-1.31	gl(67.3) ol(8.2)	cpx(9.0)	pl(15.5)			0.82
131	3.1	204.3	0.47[f]	0.85	0.07	150	-11.61	-2.26	gl(55.6) ol(11.2)	cpx(13.7)	pl(19.5)			0.43
1050°C														
142	4.5	207	6.36[f]	*4.84*	1	1999	-10.05	-0.01	gl(80.8) ol(7.3)	cpx(11.9)	pl (tr) fl			0.42
141	4.5	207	2.03[f]	3.33	0.64	1289	-10.43	-0.39	gl(60.9) ol(8.6)	cpx(17.6)	pl(12.9)			0.41
140	4.6	207.9	0.96[f]	2.90	0.51	1024	-10.57	-0.54	gl(33.0) ol(12.1)	cpx(24.3)	pl(30.6)			0.28
143	4.7	200.1	0.55[f]	2.04	0.32	616	-10.95	-0.91	gl(27.2) ol(12.6)	cpx(26.2)	pl(34.0)			0.35
1000°C														
148	9.2	206.8	4.46[g]	*5.06*	1	1947	-10.76	+0.01	gl(48.8) ol(11.4)	cpx(24.2)	pl(15.6) fl			0.13
147	5.5	206.7	1.91[g]	5.01	0.99	1921	-10.76	+0.02	gl(38.2) ol(11.5)	cpx(26.3)	pl(24.0)			0.19
146	5.5	206.7	1.12[g]	5.04	0.99	1946	-10.74	+0.03	gl(20.2) ol(12.0)	cpx(31.8)	pl(35.9)			0.28
145	5.5	206.7	0.55[g]	3.52	0.64	1248	-11.13	-0.36	gl(14.5) ol(14.5)	cpx(29.1)	pl(40.7)			0.40
950°C														
153	7.5	205.8	4.46[g]	*5.12*	1	1879	-11.48	+0.09	gl(18.5) ol(4.9)	cpx(25.8)	pl(28.5)	am(22.3) fl		0.56
152	7.5	205.8	1.91[g]	*5.12*	1	1879	-11.48	+0.09	gl(14.2) ol(8.2)	cpx(23.3)	pl(35.9)	am(18.4) fl		0.31
151	7.5	205.8	1.12[g]	*5.17*	1	1879	-11.48	+0.09	gl(7.9) ol(8.1)	cpx(29.1)	pl(36.6)	am(17.3) ilm(1.0) fl		0.16
150	7.5	205.8	0.55[g]	-	-	1879	-11.48	+0.09	ol cpx pl am ilm[i]					

[a] water content of the residual glasses estimated by mass balance calculations (see chapter 2)

[b] log fO_2 based on equation for MnO-Mn_3O_4 buffer curve (Chou 1978) assuming intrinsic buffering capacity of used IHPV corresponding to the MnO-$Mn O$ buffer (see text)

[c] Δ QFM indicates log fO_2 (experiment) - log fO_2 (QFM buffer) as estimated by Schwab and Küstner (1981)

[d] gl glass, ol olivine, cpx clinopyroxene, opx orthopyroxene, pl plagioclase, mt magnetite, ilm ilmenite, am amphibole, fl fluid

[e] phase proportions calculated by mass balance are given in wt%

[f] H_2O added to dry glass powder

[g] H O content in pre-hydrated glasses measured by Karl-Fischer-Titration

[h] numbers in italics indicate runs with aH_2O = 1 where water content was calculated using the Burnham model (Burnham 1979; see details in chapter 2)

[i] phases have been identified qualitatively

1200 °C (conditions similar to the desired $f\mathrm{O}_2$ in the crystallization experiments at $a\mathrm{H}_2\mathrm{O} = 1$) following the procedure described by Ford (1978). To allow saturation with Fe, $\mathrm{Au}_{80}\mathrm{Pd}_{20}$ tubes were loaded in a ceramic crucible containing a glass with similar composition as B1 and held for 3 days at 1225 °C in an 1 atm gas mixing furnace. The capsules were subsequently recovered by dissolving the surrounding glass in HF.

The experiments were conducted in an internally heated pressure vessel (IHPV) equipped with a rapid-quench sample holder to avoid crystallization during quenching. Due to the relatively high intrinsic $f\mathrm{O}_2$ of the vessel ($\mathrm{MnO}\text{-}\mathrm{Mn}_3\mathrm{O}_4$ buffer), a mixture of Ar and H_2 was used as pressure medium to adjust the $f\mathrm{O}_2$ in the pressure vessel at values which correspond to the QFM buffer. Therefore, in addition to the rapid-quench setup, an H_2-sensor membrane made of platinum is attached to the sample holder which allows to measure the $p\mathrm{H}_2$ prevailing at run conditions in the vessel. This experimental setup is described in detail in chapter 1.

The vessel has been loaded with two or four capsules (corresponding to the four different bulk water contents; Tab. 3.1) and brought directly to run temperature. Phase relations were investigated in 50 °C intervals from 1150 °C to 950 °C at a pressure of 200 MPa and a $f\mathrm{O}_2$ corresponding to the QFM buffer (at $a\mathrm{H}_2\mathrm{O} = 1$). Experimental duration was limited by the diffusive Fe-loss to the capsule material and varied with temperature from 2.2 to 9.2 h (Tab. 3.1). After quenching each capsule was weighed to check for leaks and than punctured to determine if a fluid phase was present or not. A cross-section of each capsule (including sample container) was prepared as polished section for electron microprobe analyses of solid phases and noble metal.

3.2.2. Analytical Techniques

The analytical techniques for water determination in glasses (Karl-Fischer-Titration, KFT; mass balance calculations; "by-difference"- method) and for major element analyses (microprobe; correction for alkali-loss) are identical to that described in chapter 2 and are not

described in detail here. The analyses of glasses in runs with low melt fractions have been possible because small batches of crystal-free residual liquid were located along the capsule rim. This was especially the case for run no. 151 containing about 8 wt% melt (from mass balance calculations).

The fO_2 was calculated for each charge using the H_2O dissociation constant of Robie et al. (1978) with fugacity coefficients for H_2 from Shaw and Wones (1964) and H_2O from Pitzer and Sterner (1994). pH_2 and thus fH_2 was recorded continuously and the experiments were stopped when a constant pH_2 was reached. The time needed to attain osmotic H_2-equilibrium between vessel and the H_2-sensor membrane is typically about 30 h at 1150 °C and 200 MPa. Because the duration at which the experimental charge is heated has to be lower (Fe-loss to the sample container) than the time needed for an exact pH_2-measurement, the capsules were quenched with the rapid-quench setup before cooling the pressure vessel (chapter 1). The quenched capsules stay on the bottom of the sample holder (in the cold area of the vessel with 20 – 25 °C) and no further reaction could take place in the capsule.

At water-saturated conditions, the proportion of H_2 added to the pressure medium (Ar) was chosen so as to reach a final pH_2 and therefore fO_2 corresponding to the QFM buffer (Tab. 3.1; calculation of fO_2 based on the equation of Schwab and Küstner, 1981). It should be noted that in water-undersaturated experiments fH_2O and thus fO_2 decrease with aH_2O (Scaillet et al., 1995) resulting in much more reducing fO_2 conditions at low aH_2O. To calculate fO_2 at water-undersaturated conditions we have used thermodynamic model of Burnham (1979) for calculating aH_2O. The good agreement between measured and calculated water solubility for the B1 starting material has been confirmed in an experiment performed at a temperature above the liquidus (4.46 wt% H_2O measured by KFT for a glass held at 1200 °C and 203.3 MPa at the QFM buffer and 4.50 wt% H_2O calculated with the "Burnham model" assuming $aH_2O = 1$ for the same pressure and temperature conditions).

The melt Fe^{2+}/Fe^{3+} ratio has been calculated after Kress and Carmichael (1991). As emphasized by Baker and Rutherford (1996) and Gaillard et al. (2001) the expression of Kress and Carmichael (1991) has not been calibrated against hydrous glasses. Baker and Rutherford (1996) and Gaillard et al. (2001) showed that, for H_2O-saturated rhyolitic melts, water has an oxidizing effect on the melt Fe^{2+}/Fe^{3+} ratio relative to the Kress and Carmichael (1991) expression, especially at fO_2 < NNO +1.5. Concerning the hydrous experiments performed in this study at the QFM buffer (which is below the NNO buffer conditions), the melt Fe^{2+}/Fe^{3+} ratios were not corrected with respect to the melt water content, because the data of Baker and Rutherford (1996) and Gaillard et al. (2001) were obtained for water-saturated conditions in very silicic melts only. Thus, the effect of dissolved H_2O on Fe^{2+}/Fe^{3+} ratio in basaltic melts, especially in runs at aH_2O is < 1, is unknown.

3.2.3. Attainment of Equilibrium and Loss of Iron

The experimental strategy in this study performing phase equilibrium experiments with hydrous low viscosity basaltic compositions is widely similar to that described in chapter 2. In the former study, in which experiments were conducted at high fO_2 (MnO-Mn_3O_4 buffer),
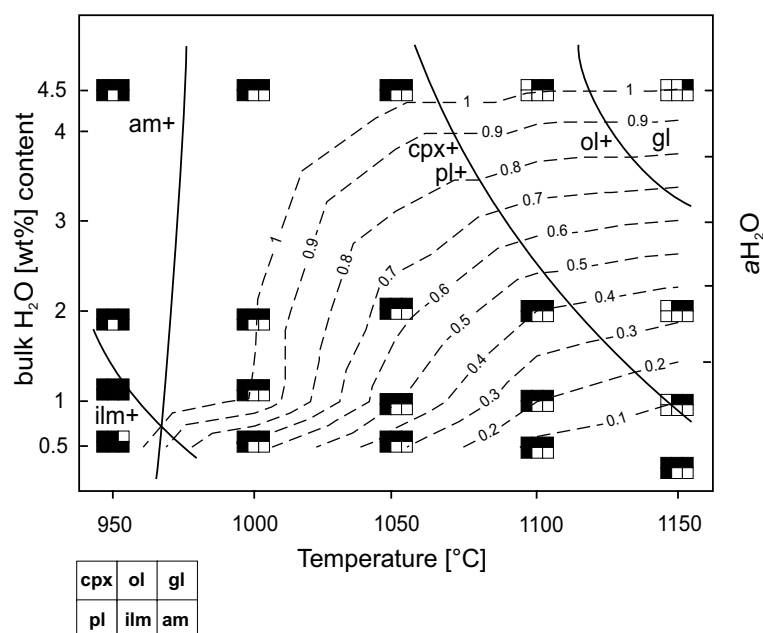
Figure 3.1 Phase relations of B1 composition as a function of temperature-bulk water content-aH_2O at 200 MPa and an oxygen fugacity corresponding to the QFM buffer. Abbreviations: gl glass, ol olivine, pl plagioclase, cpx clinopyroxene, mt magnetite, ilm ilmenite, am amphibole. Solid lines indicate saturation (+) of phases. Lines of equal aH_2O are determined from aH_2O calculated for each charge after Burnham (1979; Tab. 3.1).

equilibrium conditions have been reached as shown i.e. by mineral-melt and mineral-mineral

partitioning coefficients which are in good agreement with published data from other studies.

It should be noted that iron loss from the melt to the sample container is negligible at these

oxidizing conditions. In the present study performed at more reducing fO_2 iron loss is a

general problem (for detailed description see Sisson and Grove, 1993a). Following the

procedure described above, iron loss could be limited in our study. A melt composition profile

of run no. 130 (Tab. 3.6) performed above the liquidus temperature at 1150 °C and with about

4.58 wt% H_2O melt water content (Tab. 3.1) showed that iron has been lost mainly from the

rim of the experimental charge which is in direct contact with the capsule material. In the

middle of the capsule the initial iron concentration of the glass was preserved. The average

iron content along the profile is lower by about 4.8 wt% relative when comparing to the

starting material. Iron loss from the other experiments performed at 1150 °C have been

estimated to be between 6 and 8 wt% relative by mass balance calculations. At temperatures
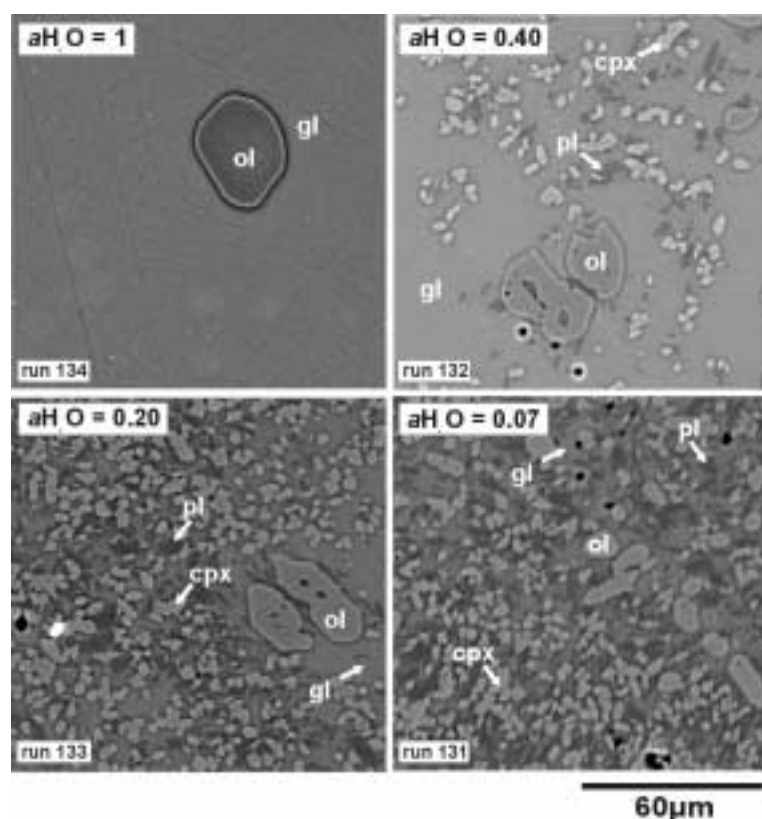
Figure 3.2 Back scattered electron images (BSE) of phases crystallizing at 1100 °C at the QFM buffer showing increasing solid phase proportions with decreasing aH_2O for a given temperature. Abbreviations see Figure 3.1.

below 1100 °C, Spulber and Rutherford (1983) and Sisson and Grove (1993a) emphasized that no significant amount of iron was lost from their samples to the capsule material. Therefore, iron content of the glasses analyzed in the middle of the capsule are believed to be realistic. This is confirmed by olivine-melt and clinopyroxene-melt partition coefficients, which agree with published data for these minerals (see below).

3.3. Results

3.3.1. Phase Stability

Phase relations of B1 composition are a function of both bulk water content and aH$_2$O, as shown in Figure 3.1. Varying aH$_2$O of the melt only, at constant pressure and temperature changes phase relations significantly (Fig. 3.2). Generally, olivine is the liquidus phase for all bulk water contents and starts to crystallize between 1125 °C and 1150 °C at water-saturated conditions. At aH$_2$O $<$ 0.4 olivine crystallizes at temperatures higher than 1150 °C. Plagioclase and clinopyroxene saturation temperature is about 50 °C below that of olivine. The crystallization sequence between these two phases is difficult to distinguish and could not be determined exactly by the runs at 50 °C temperature interval in this study. However, in run no. 127 (1150 °C, 0.35 wt% bulk water content) there is evidence from texture and phase
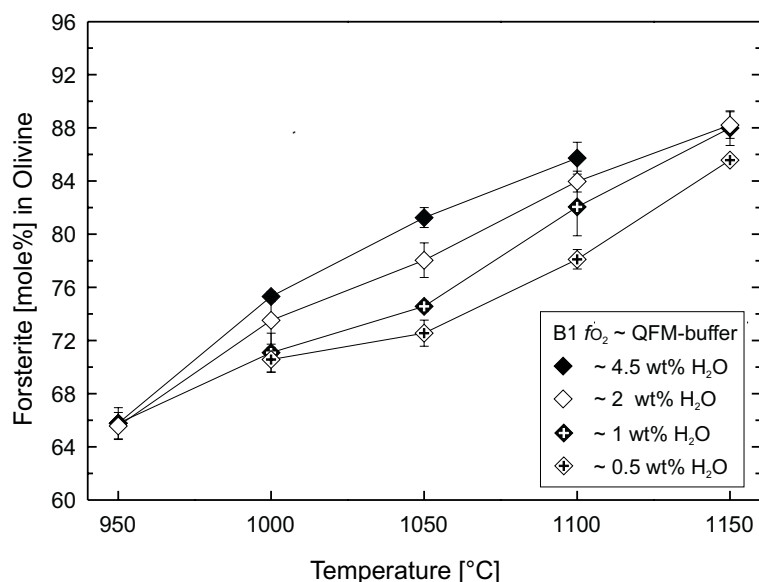
Figure 3.3 Olivine compositions plotted against temperature with respect to bulk water contents. Error bars correspond to standard deviation of average olivine compositions. If no errors bars are given, the height of the symbols corresponds to the average error.

proportions that plagioclase crystallizes first whereas in runs no. 132 and 142 (1100 °C, 2.0 wt% and 1050 °C, 4.46 wt% bulk water content, respectively) clinopyroxene seem to crystallize earlier than plagioclase. Amphibole is stable only in experiments at 950 °C in which water-saturated conditions have been reached even for low bulk water contents (Fig. 3.1). Ilmenite crystallizes in runs no. 151 and 150 at 950 °C (1.12 and 0.55 wt% bulk water content, respectively). Solidus temperature has been reached in run no. 150 and crystals were too small to analyze correctly. Thus, ilmenite as well as all other phases were only identified qualitatively in this experiment by back-scattered electron images.

3.3.2. Phase Compositions

X_{Fo} in olivine (Tab. 3.2; Fig. 3.3) decreases with decreasing bulk water content and temperature. Hence, a maximum X_{Fo} of 88 has been measured in run no. 129 with olivine as liquidus phase (1150 °C and 2.01 wt% bulk water content). The Mg# of the coexisting melt is high and reaches a value of 69 (Mg#, defined as X_{MgO} / (X_{MgO} + X_{FeO}) x 100 and Fe_2O_3 and FeO content calculated after Kress and Carmichael (1991). The minimum X_{Fo} has been observed in olivine crystallizing at 950 °C and is identical independently of bulk water (with a X_{Fo} of 66). This is related to melt Mg# which is almost identical in all 950 °C experiments content (ranging from 38 to 35 for 4.46 and 0.55 wt% bulk water content, respectively). Thus, decreasing X_{Fo} is a function decreasing melt Mg# with falling temperature and bulk water content due to the increasing amount of crystals (see below). As emphasized in chapter 2, in addition to the bulk water content, the water activity also influences olivine compositions in runs in which $a\mathrm{H_2O}$ is < 1 since the prevailing $f\mathrm{O_2}$ is lower than at $a\mathrm{H_2O} = 1$ resulting in a lower melt Mg# (due to the increasing melt Fe^{2+} with decreasing $f\mathrm{O_2}$). The olivine/melt partitioning of Fe-Mg, expressed as $Kd_{Fe-Mg}^{Ol-Melt}$ (Roeder and Emslie, 1970; defined as $X_{Ol-FeO}/X_{Melt-FeO}*X_{Melt-MgO}/X_{Ol-MgO}$), indicates a close approach to equilibrium. The average $Kd_{Fe-Mg}^{Ol-Melt}$ is 0.31 ($\pm$ 0.03) which is in good agreement with the value given by Roeder and

Emslie (1970) of about 0.3 (± 0.02). As emphasized in chapter 2, $D_{CaO}^{Ol-Melt}$ ($CaO_{Olivine}/CaO_{Melt}$, in wt%) differs from the model of Libourel (1999) which is calibrated for anhydrous melts. Figure 3.4 shows that the calculated $LnD*_{CaO}^{Ol-Melt}$ using the model of Libourel (1999) is not appropriate to describe the Ca partitioning between olivine and melt in our experiments, both at reducing and oxidizing conditions. As already shown in chapter 2 the calculated $LnD*_{CaO}^{Ol-Melt}$ is the less appropriate for experiments with high aH_2O and low SiO_2 content of the residual melt. The two trends observed for high and low fO_2 (Fig. 3.4) show that the deviation from the model is independent of fO_2 but mainly a function of aH_2O and melt structure which is influenced by dissolved water.

The clinopyroxenes have an average composition of $En_{44}Fs_{14}Wo_{42}$ (±2 mole%) and vary only slightly with changing experimental conditions (Tab. 3.3). The average $Kd_{Fe-Mg}^{Cpx-Melt}$ of clinopyroxene (defined as $X_{Cpx-FeO}/X_{Cpx-MgO}*X_{Melt-MgO}/X_{Melt-FeO}$) is 0.26 but generally increases with melt Mg# (Fig. 3.5). As reported by Hoover and Irvine (1977) and Toplis and Carroll (1995) $Kd_{Fe-Mg}^{Cpx-Melt}$ values increase independent of fO_2 with increasing melt Mg# up to 0.26 (for melt Mg# of about 40). Figure 3.5 confirms this observation by showing
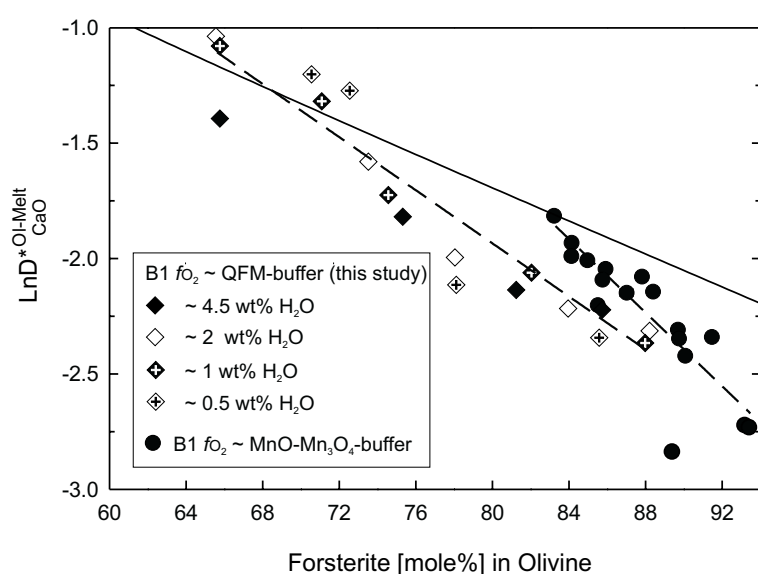
Figure 3.4 Calculated $LnD*_{CaO}^{Ol-Melt}$ values for olivine- melt pairs crystallized at oxidizing ($MnO-Mn_3O_4$ buffer; chapter 2) and reducing (QFM buffer) conditions after the model of Libourel (1999). Solid line shows $LnD*_{CaO}^{Ol-Melt}$ trend calculated using an empirical function of Libourel (1999). Dashed lines indicate calculated $LnD*_{CaO}^{Ol-Melt}$ trends approaching the described $LnD*_{CaO}^{Ol-Melt}$ obtained from the empirical function of Libourel (1999) due to increasing melt SiO_2 content and generally decreasing aH_2O. Water contents are given as bulk water contents.

experimental $Kd_{Fe-Mg}^{Cpx-Melt}$ values from numerous authors for different bulk compositions and fO_2. For relatively low melt Mg# in this study the obtained $Kd_{Fe-Mg}^{Cpx-Melt}$ values are in good agreement with published data. For melt Mg# above 50, the $Kd_{Fe-Mg}^{Cpx-Melt}$ deviates from the linear trend with values up to 0.41 (Fig. 3.4). The same observation has been made for partitioning of Mg and Fe^{2+} between clinopyroxene and melt under more oxidizing conditions which confirms that there is no dependence of $Kd_{Fe-Mg}^{Cpx-Melt}$ on fO_2 (Toplis and Carroll, 1995). It is noteworthy that the bulk water content has no influence on $Kd_{Fe-Mg}^{Cpx-Melt}$.

The composition of plagioclase as a function of temperature, bulk water content, and aH_2O is shown in Figure 3.6 and Table 3.4. In agreement with previous studies (e.g., Turner and Verhoogen, 1960; Carmichael et al., 1974; Panjasawatwong et al., 1995), at a given temperature, the An content of plagioclase increases with increasing melt water content and therefore increasing aH_2O. However, Figure 3.6 shows clearly that plagioclase composition is
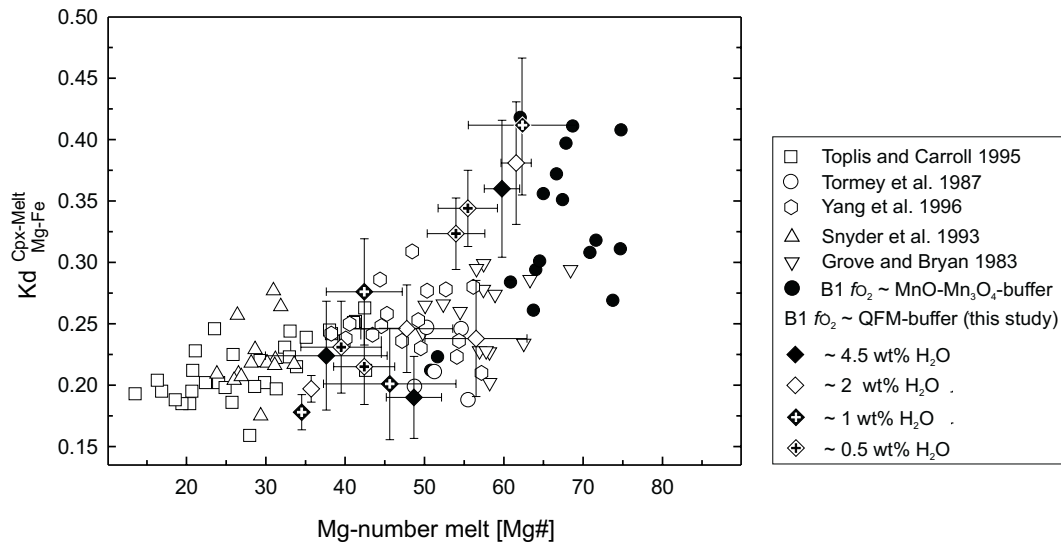
Figure 3.5 $Kd_{Fe-Mg}^{Cpx-Melt}$ of clinopyroxene are plotted against melt Mg#. $Kd_{Fe-Mg}^{Cpx-Melt}$ values for clinopyroxene-melt pairs obtained at high fO_2 (chapter 2) are shown as well as $Kd_{Fe-Mg}^{Cpx-Melt}$ values of numerous authors for various basaltic compositions. Water contents are given as bulk water contents.

also a function of bulk water content, because at 950 °C water-saturated conditions ($a\mathrm{H_2O}$ = 1) have been reached for all experiments (independently of bulk water content). At this temperature, plagioclase crystallizing in runs with high bulk water content is An-richer. The direct influence of $\mathrm{H_2O}$ on plagioclase composition can be shown in Figure 3.7. Partitioning coefficient of Ca and Na between plagioclase and melt ($\mathrm{Kd}_{\mathrm{Ca\text{-}Na}}^{\mathrm{Pl-Melt}}$ defined as $(\mathrm{Ca/Na})_{\mathrm{Plag}}$ / $(\mathrm{Ca/Na})_{\mathrm{Melt}}$) increases strongly with melt water content. $\mathrm{Kd}_{\mathrm{Ca\text{-}Na}}^{\mathrm{Pl-Melt}}$ values obtained in this study for plagioclase crystallizing from melts containing about 2 wt% and 4.84 to 5.17 wt% $\mathrm{H_2O}$, respectively, agree well with trends for high-alumina basalts of Sisson and Grove (1993a) and Baker and Eggler (1987) under comparable T-$\mathrm{H_2O}$ conditions (two regression lines for different melt water contents in Fig. 3.7). This suggests that the relation between $\mathrm{Kd}_{\mathrm{Ca\text{-}Na}}^{\mathrm{Pl-Melt}}$ and melt water content found by Sisson and Grove (1993a) for high-alumina basalts is also relevant to tholeiitic MORB systems. Generally, An content falls with temperature for all bulk water contents due to the strong depletion in melt Ca content and moderate enrichment in melt Na concentration (see below) with crystallization.

Experimental amphiboles are tschermakites (classification after Leake et al., 1997).
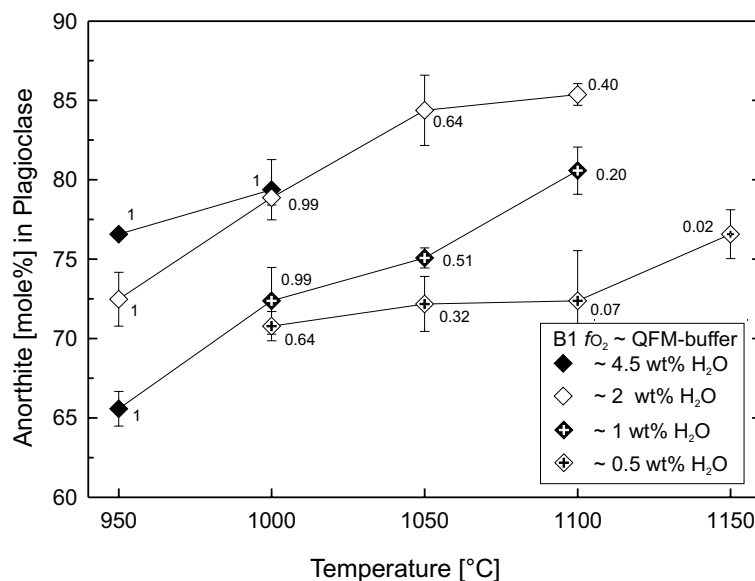
Figure 3.6 Plagioclase composition as a function of temperature and bulk water content. Errors bars correspond to standard deviation of average plagioclase compositions from multiple microprobe measurements. Water contents are given as bulk water contents. Numbers indicate $a\mathrm{H_2O}$ of the melt.

Amphibole Mg# (defined as $X_{Mg}/(X_{Mg}+X_{Fe}^{2+})$ x 100) decreases with decreasing bulk water content (Tab. 3.5). Partitioning coefficient of Al and Si between amphibole and melt (defined as $Kd_{Al-Si}^{Am-Melt}$ ($(Al/Si)_{Am}/(Al/Si)_{Melt}$) have values of about 1 (± 0.08) and correspond to $Kd_{Al-Si}^{Am-Melt}$ values given by Sisson and Grove (1993a) of about 0.94 ($\pm$ 0.06) for melt-amphibole pairs in compositions ranging from high-alumina basalt to rhyolite.

Ilmenite crystals in run no. 151 were relatively small and therefore difficult to analyze. However, ilmenite content (X_{Ilm}; calculated after Andersen et al., 1993) could be determined and is about X_{Ilm89}. As emphasized above, ilmenite in run no. 150 has been identified qualitatively only.

Experimental melt compositions are given in Table 3.6. The evolutions of melt SiO_2 and FeO* with temperature as a function of bulk water content are shown in Figure 3.8. Melt compositions vary strongly with temperature and bulk water content and follow a tholeiitic differentiation trend (Fig. 3.10, 3.11; Irvine and Baragar, 1971; Miyashiro et al., 1969) ranging from gabbroic to dioritic compositions (classified after Wilson (1989) using the TAS diagram). SiO_2 content of the melt (Fig. 3.8a) increases with falling temperature and bulk
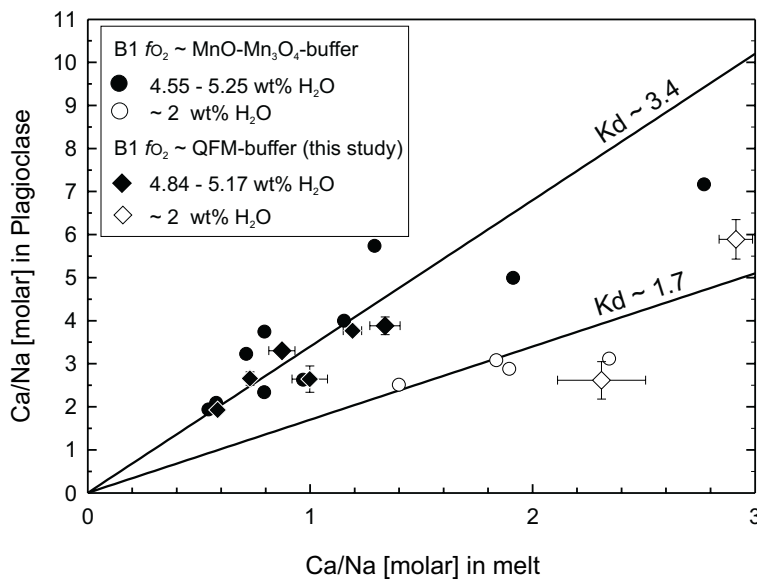
Figure 3.7 Ca/Na ratios for plagioclase-melt pairs obtained at water-saturated conditions ($aH_2O = 1$, melt water contents calculated after Burnham (1979; Tab. 3.1) and approximately 2 wt% H_2O in melt. Note that Ca/Na ratios for plagioclase-melt pairs obtained at high fO_2 (chapter 2) are also shown. Solid lines show $Kd_{Ca-Na}^{Pl-Melt}$ after Sisson and Grove (1993a) for plagioclase-melt pairs in high-alumina basalt (Sisson and Grove, 1993b); at 100 MPa and about 4 wt% H_2O in melt ($Kd_{Ca-Na}^{Pl-Melt}$ ~ 3.4) and about 2 wt% H_2O in melt at 200 and 500 MPa (Baker and Eggler, 1987; Kd ~ 1.7).

water content up to 61 wt% (run no. 151). FeO* concentration generally increases with decreasing temperature, but shows significant variations with changing bulk water content (Fig. 3.8b). For water-saturated melts, FeO* content increases slightly from 1150 °C to 950 °C (8.24 wt% at 1150 °C and 8.97 wt% at 950 °C). For lower bulk water contents, FeO* first increases with decreasing temperature and decreases at temperatures below 1050 °C. The highest FeO* is observed for about 0.5 wt% bulk water content with 10.95 wt% FeO* at 1050 °C (run no. 143). The FeO* content in water-saturated melts at 950 °C is identical in runs no.
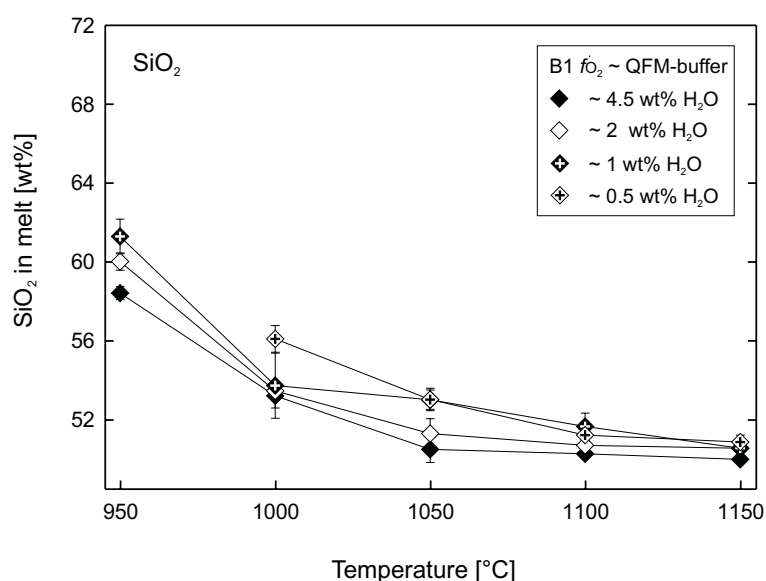
Figure 3.8a B1 melt SiO$_2$ content as a function of bulk water content and temperature. Errors bars are from standard deviation multiple microprobe measurements (Tab. 3.6). If no errors bars are given, the height of the symbols corresponds to the average error. Note that no melt SiO$_2$ and FeO* concentrations at 950 °C and 0.5 wt% bulk water are given since the solidus temperature is reached in this experiment (run no. 150; Tab. 3.1). Water contents are given as bulk water contents.
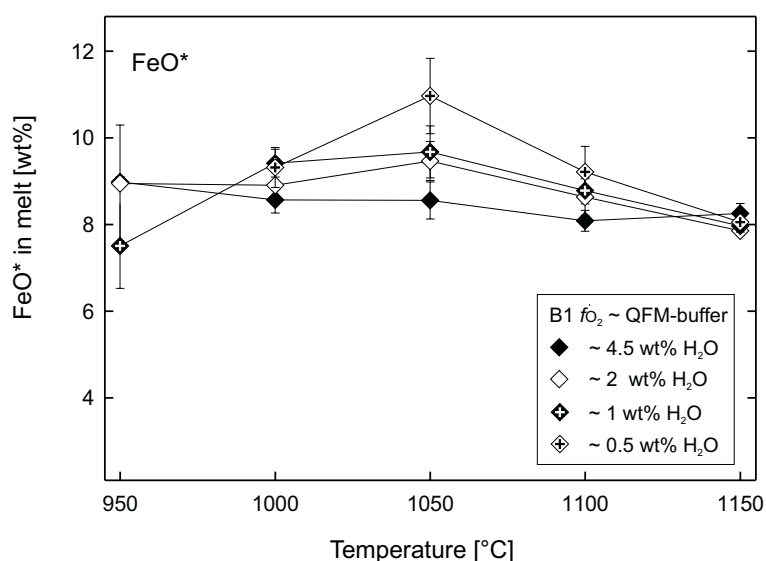
Figure 3.8b B1 melt FeO* content as a function of bulk water content and temperature. For detailed comments see Figure 3.8a.

153 and 152 (no ilmenite present). However, the melt FeO* content is significantly lower in run no. 151 containing ilmenite. With decreasing temperature and bulk water content, the melt MgO and CaO concentrations also decrease. In contrast, Na_2O and K_2O raise in concentration with falling temperature and bulk water content. A maximum TiO_2 content is reached at 1000 °C and decreases generally in all experiments at 950 °C. Melt Al_2O_3 content shows no systematic variation with changing experimental conditions but is slightly higher in runs performed at 1000 °C.

3.4. DISCUSSION

3.4.1. Comparison of Phase Relations at High and Low fO_2

Phase relations obtained for B1 starting composition at oxidizing ($MnO\text{-}Mn_3O_4$ buffer; see chapter 2) and reducing (QFM buffer) oxygen fugacities can be compared to estimate the effect fO_2 since all other parameters were equal (pressure, temperature, bulk water contents). For both oxygen fugacities olivine is the liquidus phase crystallizing at similar temperatures between 1150 °C and 1100 °C depending on bulk water content. In contrast to B1 phase relations at oxidizing conditions, orthopyroxene is not stable at reducing fO_2. This is in agreement with previous studies (e.g., Grove and Juster, 1989) which show that decreasing melt Mg# (due to decreasing fO_2) strongly confines the low-Ca pyroxene stability. Since orthopyroxene is not stable at reducing conditions (melt Mg# of about 35 at 950 °C; Tab. 3.6), olivine is present in the low temperature runs at 950 °C, in contrast to oxidizing conditions (melt Mg# of 61 to 68). As discussed in detail below, magnetite did not crystallize at reducing conditions due to the lower melt Fe^{3+}/Fe^{2+} ratio. Ilmenite stability is less dependent on oxidation state of the melt and this mineral is observed at the same temperature and bulk water contents both at reducing and oxidizing conditions. The clinopyroxene and plagioclase saturation is also widely independent on fO_2 since both phases crystallize between 1150 °C and 1050 °C.

3.4.2. Influence of H_2O and fO_2 on Fe-Ti Oxide Stability

Stability of Fe-Ti oxides in basaltic systems has been widely investigated because of its important influence on differentiation path. Generally, it is difficult to discriminate between single effects of H_2O, fO_2, and melt composition (and thus activities of critical components) on the stability of ilmenite and magnetite. As show by e.g., Toplis and Carroll (1995) and Snyder et al. (1993) for dry basaltic systems, magnetite stability field is dependent on the oxidation state of the melt and is strongly expanded to high temperature with increasing fO_2 (due to the increasing ferric iron content of the melt). In contrast, ilmenite is stable at lower fO_2 and is rather a function of melt TiO_2 content than of melt oxidation state (Toplis and Carroll, 1995).

Concerning the ilmenite stability in hydrous MORB systems, it has been shown that even at oxidizing conditions ilmenite is stable in experiments with B1 composition when melt TiO_2 content is high enough (see chapter 2). Combined with results in this study we show that the
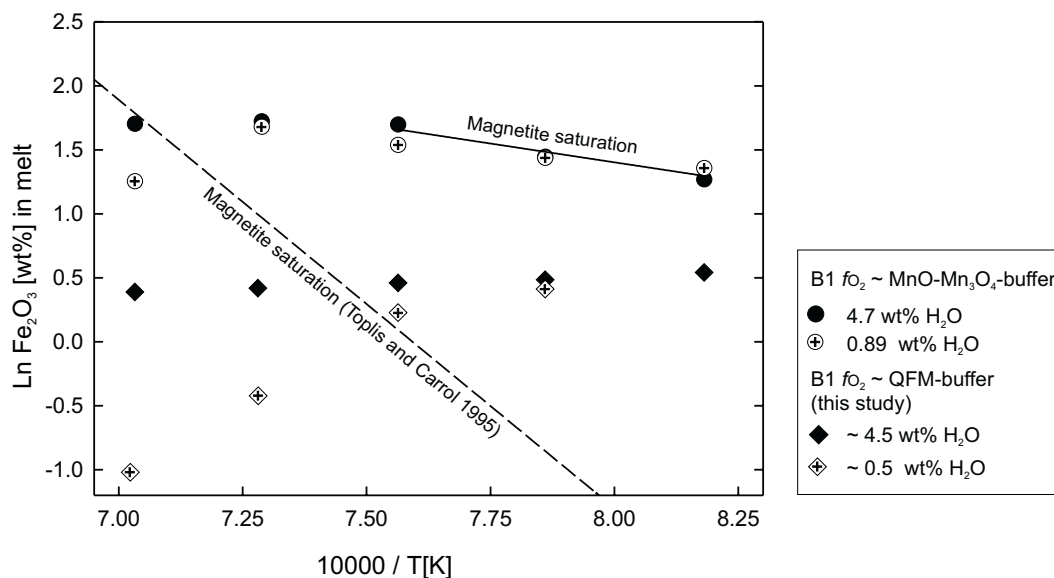
Figure 3.9 Ln Fe_2O_3 content of melts are shown as a function of the inverse temperature. Ln Fe_2O_3 contents of residual melt obtained at high fO_2 (MnO-Mn$_3$O$_4$ buffer; chapter 2) are also plotted. Only experiments with the highest (between 4.7 and 4.5 wt%) and lowest (between ~ 0.5 and 0.89 wt%) bulk water are considered. Solid line indicate experiments conducted at high fO_2 (MnO-Mn$_3$O$_4$ buffer) in which magnetite was a stable phase. Dashed line show Ln Fe_2O_3 contents of magnetite-saturated dry melts from Toplis and Carrol (1995).

stability field of ilmenite is identical for reducing and oxidizing conditions (Fig. 3.1 and Fig. 2.4a). This confirms the assumption of Toplis and Carroll (1995) suggesting that ilmenite is widely independent of melt oxidation state but depends mainly on melt TiO_2 content. Bulk water content seems not to have a direct influence on ilmenite stability but controls the melt fraction at a given temperature. At a given temperature, melts from experiments at low bulk water content have higher TiO_2 concentrations than melts in more water rich runs. Therefore, at a given temperature, ilmenite stability is enhanced with decreasing bulk water content, independently of fO_2.

Magnetite is stable in B1 runs performed at high fO_2 (chapter 2), but not in the experiments conducted at the QFM buffer. At high fO_2, magnetite crystallizes between 1100 °C and 1050 °C, but is not the liquidus phase since olivine, plagioclase and clinopyroxene are stable at higher temperatures (see Fig. 2.4a in chapter 2). This is in contrast to studies performed under dry conditions in basaltic systems at high fO_2, in which magnetite is usually the liquidus or at least a near-liquidus phase (e.g., Roeder, 1974; Grove and Juster, 1989; Juster et al., 1989) with a crystallization temperature of about 1100 °C, as estimated by Thy and Lofgren (1994), independently of bulk composition. A possible explanation for the lower saturation temperature in hydrous MORB systems is that the solubility of magnetite is higher in hydrous melts than in dry systems. Toplis and Carroll (1995) showed (with additional data of Snyder and Carmichael, 1992; Thy and Lofgren, 1994; Juster et al., 1989) that the ferric iron content of magnetite-saturated liquids is a linear function of the inverse temperature for a variety of dry basaltic compositions, independently of fO_2 (Fig. 3.9). The results at high fO_2 (chapter 2) show that magnetite saturation is reached at lower temperatures for a given melt Fe_2O_3 content compared to dry systems. This suggests that the activity of Fe_2O_3 in melt is probably lowered by H_2O compared to dry systems. The absence of magnetite in B1 at the QFM buffer can be explained by the lower melt Fe_2O_3 concentration (Fig. 3.9; note that the FeO* contents are generally higher in B1 melts obtained at the QFM buffer than those from experiments

performed under oxidizing conditions). It can be noted that magnetite is stable in dry basaltic compositions at the QFM buffer (although the crystallization temperature is lower when compared to more oxidizing conditions; e.g., Snyder et al., 1993). This also confirms that the stability of magnetite may be lowered by the presence of H_2O in MORB, both at high and low fO_2.

These observations contrast with results from earlier studies of Holloway and Burnham (1972) and Sisson and Grove (1993a) obtained in more alkali-rich compositions. A conclusion drawn from these investigations is that water stabilizes Fe-Ti oxides relative to silicates. In this study we show that it is the opposite in case of magnetite for hydrous MORB compositions. Magnetite stability is also found to be dependent on temperature and melt Fe_2O_3 content (Fig. 3.9) but the magnetite saturation curve is different from that described by Toplis and Carroll (1995) for dry conditions.

In conclusion, our results suggest that magnetite stability is a function of melt oxidation state and temperature but also on bulk compositional effects (i.e. alkalinity and H_2O content of the
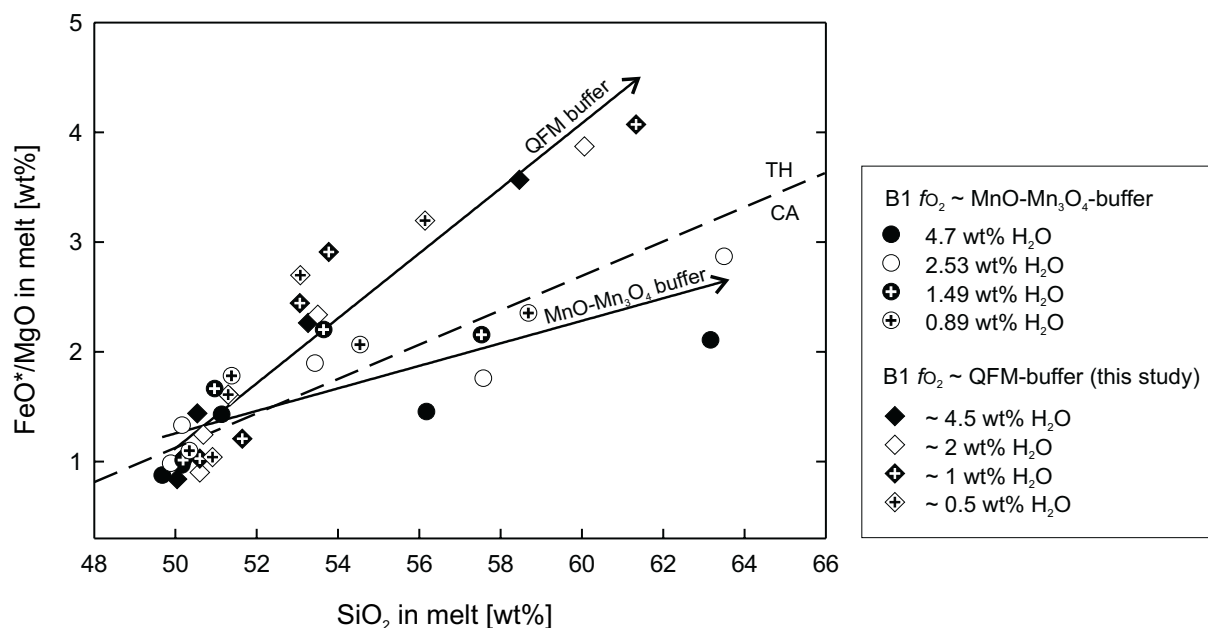
Figure 3.10 FeO*/MgO ratio of residual melts are plotted against melt SiO_2 content. Data obtained at high fO_2 (MnO-Mn$_3$O$_4$ buffer) are added. TH (tholeiitic) – CA (calc-alkaline) dividing line is from Miyashiro (1974). Water contents are given as bulk water contents.

melt). Thus, the Fe_2O_3 activity in melt and magnetite stability is dependent on a complex interplay of H_2O and fO_2 and melt compositional features. The stabilization of Fe-Ti oxides by H_2O as observed in calc-alkaline systems (e.g., Baker and Eggler, 1987; Sisson and Grove, 1993a), in contrast to MORB systems, may reflect the effect of compositional differences between these systems.

3.4.3. Differentiation Trend at High and Low Oxygen Fugacities

Residual melt compositions obtained in runs with high (chapter 2) and low fO_2 allow to estimate the influence of H_2O and fO_2 on liquid line of descent since all other parameters (bulk composition, bulk water contents, temperature, and pressure) were similar. As discussed above, the stability of Fe-Ti oxides, especially magnetite, depends strongly on fO_2 and consequently melt compositions differ as a function of fO_2. The residual liquids obtained at fO_2 conditions corresponding to the QFM buffer show a general increase in melt FeO*/MgO ratio with decreasing temperature due to absence of magnetite. These melts follow, independently of bulk water content, a tholeiitic differentiation trend (Fig. 3.10, 3.11; classification after Miyashiro, 1974, and Irvine and Baragar, 1971). This is in agreement with previous studies performed in basaltic systems at lower fO_2 in which Fe-Ti oxides are not stable until a significant amount of silicates crystallized and the melt is enriched in FeO* (e.g., Spulber and Rutherford, 1983; Juster et al., 1989; Snyder et al., 1993) causing a tholeiitic differentiation trend. Residual B1 melts from experiments at high fO_2 (MnO-Mn_3O_4 buffer; see chapter 2) coexist widely with magnetite and are consequently depleted in FeO* following a calc-alkaline differentiation trend (Fig. 3.10, 3.11). Thus, liquid lines of descent in primitive hydrous MORB´s are primarily controlled by the prevailing fO_2 (via crystallization of magnetite) and only little by the bulk water content.

These observations for a MORB composition contrast with results from Sisson and Grove (1993a) for calc-alkaline systems. Sisson and Grove (1993a) emphasized that for a constant fO_2 (corresponding to the NNO buffer) the addition of H_2O only changes differentiation path
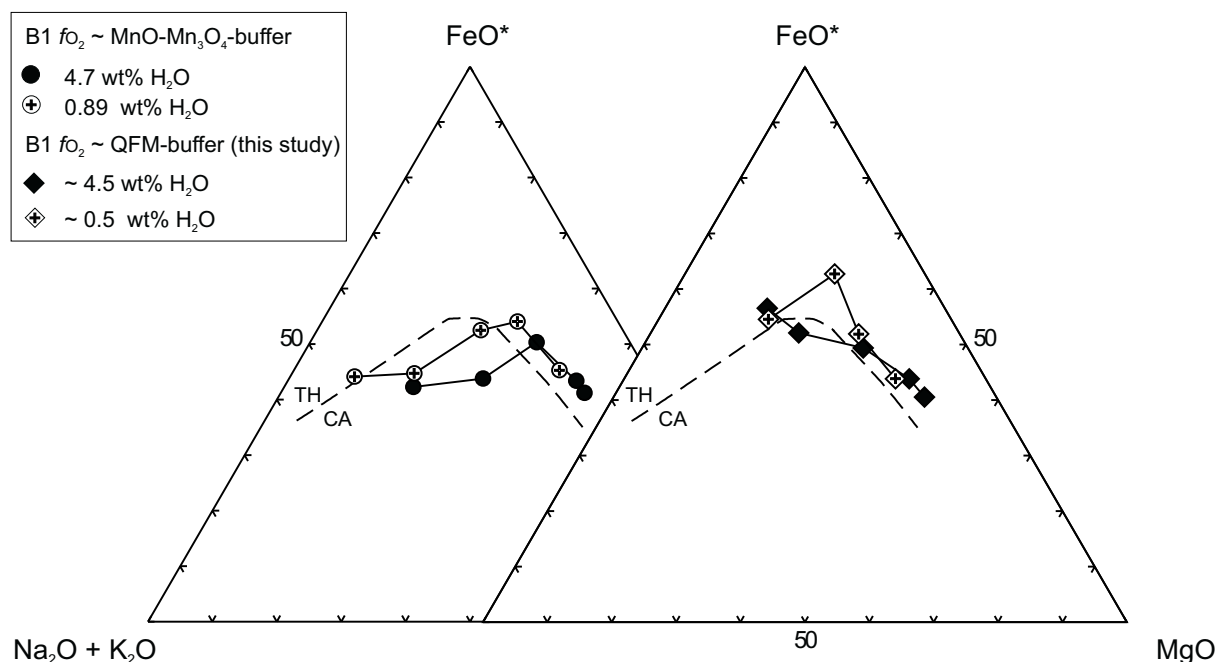
Figure 3.11 Experimental residual liquids are projected on the total alkali (Na_2O+K_2O)-total iron (FeO*)-MgO ternary diagram (calculated from melt composition in wt%). Only experiments with the highest (between 4.7 and 4.5 wt%) and lowest (between ~ 0.5 and 0.89 wt%) bulk water are shown. Data obtained at high fO_2 ($MnO-Mn_3O_4$ buffer) are added. TH (tholeiitic) – CA (calc-alkaline) dividing line is from Irvine and Baragar (1971).

from tholeiitic (dry conditions) to calc-alkalic (water-saturated) by an early stabilization of Fe-Ti oxides under hydrous conditions. The small effect of water which can be observed in Figures 3.8b and 3.11 (note that in Fig. 3.11 only melts from experiments with the highest and lowest bulk water are shown) can not produce a change from tholeiitic to calc-alkaline trend in primitive MORB´s.

3.4.4. Mechanisms of Melt FeO*-Enrichment

At low as well as at high fO_2 the melt FeO* content increases with decreasing temperature in the initial differentiation stages (Fig. 3.8b; see also Fig. 2.9c in chapter 2). When comparing the melt FeO* content at a given temperature as a function of the bulk water content, the highest differences can be observed at 1100 °C at oxidizing conditions and 1050 °C at reducing conditions. At these temperatures the highest melt FeO* is obtained for the lowest bulk water content. This can not be an effect of enhanced Fe-Ti oxide stability at high melt

water contents since magnetite is not stable under these conditions (Fig. 3.1; see also Fig. 2.4a in chapter 2). Another evidence showing that the melt FeO* enrichment in initial differentiation stages is not related to the presence of magnetite is given in melts from more evolved composition B2 obtained at 1100 °C (see Fig. 2.10 in chapter 2). As well as for the primitive B1 compositions, melt FeO* content increases with decreasing bulk water content. However, in this case magnetite is present for all bulk water contents and melt FeO* increases although the proportions of magnetite increase. This shows that magnetite is not responsible for melt FeO* enrichment in initial differentiation stages.

An important factor which may control the melt FeO* enrichment in initial differentiation stages is the proportion of plagioclase and Fe-Mg silicates. As shown by e.g. Yoder (1965), Sisson and Grove (1993a), and Gaetani et al. (1993), H_2O expands proportions of mafic Fe-Mg silicates (e.g., olivine, pyroxene, amphibole) relative to plagioclase. Thus, crystallization of higher proportions of Fe-Mg silicates and destabilization of plagioclase at high water contents depletes the melt in Fe and Mg. The plagioclase/Fe-Mg-silicate ratio for B1 is shown in Figure 3.12 for the highest and lowest bulk water contents at oxidizing and reducing conditions, respectively. As expected, plagioclase/Fe-Mg-silicate ratio is higher in runs with low bulk water content and independent on the fO_2. Consequently, residual melts obtained from experiments performed at low water contents should show systematically higher melt
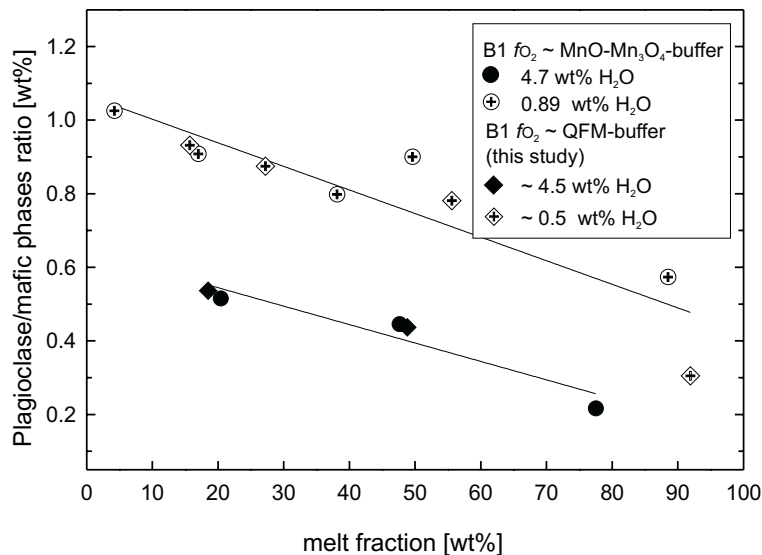
Figure 3.12 Plagioclase/mafic phase ratios are plotted against melt fractions (in wt%; both calculated by mass balances). Only experiments with the highest (between 4.7 and 4.5 wt%) and lowest (between ~ 0.5 and 0.89 wt%) bulk water are considered. Data obtained at high fO_2 (MnO-Mn$_3$O$_4$ buffer) are added.

FeO* concentrations than more hydrous liquids. This is the case for those runs conducted at high temperatures, but it is not observed for the low temperature runs since melt FeO* concentrations are almost similar at temperatures below 1100 °C (MnO-Mn_3O_4 buffer) and 1050 °C (QFM buffer; Fig. 3.8b and Fig. 2.9c in chapter 2). Additionally, it can be emphasized that the plagioclase/Fe-Mg-silicate ratio is a function of bulk water content because even if water-saturated conditions are reached at low temperatures (due to H_2O enrichment in the melt), plagioclase/Fe-Mg-silicate ratio is still higher in runs with low bulk water content.

Since increasing magnetite stability and higher proportions of plagioclase relative to Fe-Mg silicates with decreasing bulk water content can not explain melt FeO* enrichment in initial differentiation stages, another mechanism must be envisaged. The only possible parameters controlling this mechanism are crystal/melt ratio and $a H_2O$. Figure 3.13a shows the Δmelt fraction for a given temperature (in wt%, defined as melt proportion$_{(high\ bulk\ water)}$ − melt proportion$_{(low\ bulk\ water)}$) from runs performed at the highest (4.7 – 4.46 wt% H_2O) and the lowest bulk water content (0.89 – 0.35 wt% H_2O) at oxidizing and reducing conditions. The highest Δmelt fraction is obtained at 1100 °C for high fO_2 and 1050 °C for low fO_2. These temperatures correspond to those at which the highest difference in melt FeO* between high and low bulk water content is observed, as shown in Figure 3.13b (in this Figure ΔFeO* in wt% is defined as FeO*$_{(high\ bulk\ water)}$ − FeO*$_{(low\ bulk\ water)}$). At temperatures above 1100 °C and 1050 °C for high and low fO_2, respectively, the ΔFeO* is relatively small. In these runs the Δmelt fraction is low but $a H_2O$ changes strongly as a function of bulk water content. At low temperatures (950 °C and 1000 °C) ΔFeO* is also low. In these experiments Δmelt fraction is relatively low while $a H_2O$ is always close to 1. Thus, the highest ΔFeO* is observed at temperatures for which strong changes in $a H_2O$ are possible and in a temperature interval in which the crystallization of the major phases takes place. This shows that the crystal/melt

ratio (controlled by aH$_2$O) is the main parameter controlling the FeO* content of melts for a given temperature and fO$_2$.

It can be noted that the ΔFeO* in experiments between 950 °C and 1050 °C at MnO-Mn$_3$O$_4$ buffer is close to 0 although Δmelt fraction changes significantly in this temperature range. One explanation is that small variation of ΔFeO* due to variations of plagioclase/Fe-Mg-silicate ratio (see above) may be compensated by changing Fe-Ti oxide proportions in these
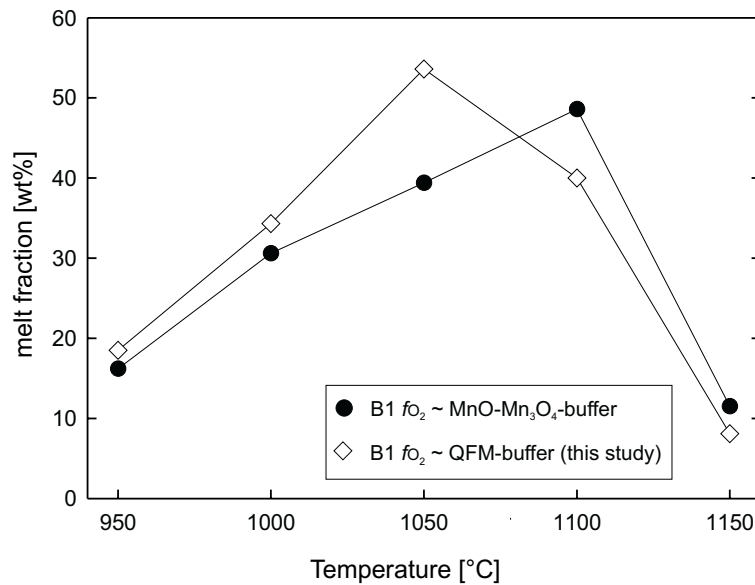
Figure 3.13a Δmelt fraction is plotted against temperature. Δmelt fraction is defined as melt proportion from experiments conducted with highest bulk water contents (between 4.7 and 4.5 wt%) - melt proportion from experiments conducted with lowest bulk water contents (0.89 − 0.35 wt% H$_2$O; e.g., at 1100 °C, QFM buffer: run no. 134 with 95.6 wt% melt − run no. 131 with 55.6 wt% melt result in a Δmelt fraction of 40; see also Tab. 3.1). Data obtained at high fO$_2$ (MnO-Mn$_3$O$_4$ buffer) are also shown.
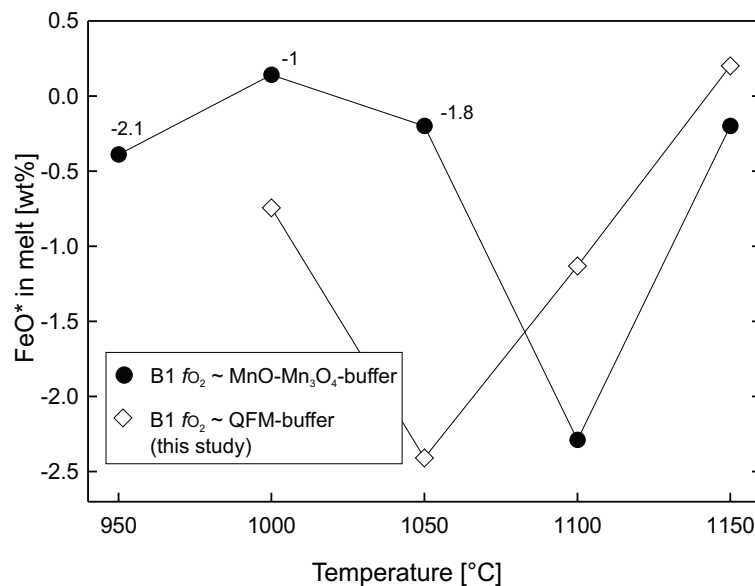
Figure 3.13b Δmelt FeO* contents are plotted against temperature. Δmelt FeO* is defined as FeO* content in residual liquids from experiments conducted with highest bulk water contents (between 4.7 and 4.5 wt%) - FeO* content in residual liquids from experiments conducted with lowest bulk water contents (0.89 − 0.35 wt% H$_2$O; e.g., at 1100 °C, QFM buffer: run no. 134 with 8.07 wt% FeO* in melt − run no. 131 with 9.20 wt% FeO* in melt result in a Δmelt FeO*of −1.13; see also Tab. 3.6). Data obtained at high fO$_2$ (MnO-Mn$_3$O$_4$ buffer) are added. Numbers indicate ΔFe-Ti-oxides (proportions in wt%) in experimental products obtained at high fO$_2$ calculated following the procedure described above, showing higher proportions of Fe-Ti oxides in experiments performed at low bulk water contents.

runs. The ΔFe-Ti oxides proportions (in wt%, defined as Fe-Ti-oxides$_{(high\ bulk\ water)}$ − Fe-Ti-oxides$_{(low\ bulk\ water)}$) are shown in Figure 3.13b. These values are negative which implies that higher Fe-Ti oxide proportions at low bulk water contents may compensate the small effect of melt FeO* enrichment due to the higher plagioclase/Fe-Mg-silicate ratio in these runs.

In conclusion, the addition of water can not change the general differentiation trend which is determined by the fO$_2$ in the B1 MORB composition. Nevertheless, melts from experiments performed at initially low aH$_2$O (low bulk water content) have a moderate FeO* enrichment in initial differentiation stages, independently of the fO$_2$. This is, however, not due to a depressed stability field of magnetite at low aH$_2$O but to a general higher crystal/melt ratio at low aH$_2$O in the main crystallization interval (and only to a lesser extent to high plagioclase/Fe-Mg silicate ratio).

3.4.5. Implications for the Origin of SiO$_2$-rich Residual Melts

Leucocratic rocks, such as plagiogranites, are commonly found in ophiolites (e.g., Malpas, 1979; Coleman and Peterman, 1975; Jenner et al., 1991) and are also present in minor abundances in the oceanic crust (e.g., Dick et al., 1991). The processes discussed to generate these SiO$_2$ –rich melts are 1. A partial melting of gabbro, basalt, or amphibolite (e.g., Flagler and Spray, 1991; Springer and Seck, 1997) 2. Crystal-liquid differentiation from a basaltic source magma (e.g., Martin, 1987; Arth et al., 1978) 3. Immiscibility between a Fe-enriched and a silicic residual liquid (Dixon and Rutherford, 1979). There is, however, no evidence in the experiments at high fO$_2$ and in this study that residual melts become immiscible at later stages of differentiation. SiO$_2$–rich residual melts containing more than 60 wt% SiO$_2$ are produced in the B1 crystallization experiments under oxidizing and reducing fO$_2$ conditions at 950 °C (Fig. 3.10). As expected, the B1 residual liquids obtained under high fO$_2$ are more SiO$_2$–rich than those at reducing conditions due to the crystallization of magnetite at high fO$_2$ which causes a stronger SiO$_2$ enrichment of the melt (e.g., Toplis and Carroll, 1995; about 64

wt% SiO_2 in residual melts at the $MnO-Mn_3O_4$ buffer and about 60 wt% SiO_2 in melts at the QFM buffer at 950 °C). Typical plagiogranites, however, have slightly higher bulk SiO_2 values between 65 and 75 wt% SiO_2 (e.g., Coleman and Peterman, 1975). Such values have been obtained using the fractionated B2 starting composition (chapter 2; B2 composition represents a residual liquid after 50% crystallization of B1) suggesting that fractionating processes need to be involved for the generation of residual melts with such high SiO_2 values (e.g., Barnes et al., 1992). Thus, it can be emphasized that no extreme fractionation of a MORB magma is required to produce a plagiogranitic residual liquid. A plagiogranitic liquid can be generated in the later stages of crystallization of a melt extracted from a primitive MORB system after 50% crystallization.

However, typical bulk FeO* contents in plagiogranites are in the range of 1- 7 wt% which does not match with the liquids obtained under QFM buffer conditions due to the tholeiitic trend caused by the absence of magnetite (with about 9 wt% melt FeO* content in the most evolved melts of B1; Tab. 3.6). In contrast, residual liquids produced under oxidizing conditions show melt FeO* contents of about 5 wt% corresponding to common bulk iron contents found in natural plagiogranites. This does, however, not mean that generation of plagiogranites takes place at such high fO_2. A fractionation event of B1 at QFM buffer would also result in FeO* depletion and SiO_2 enrichment of the melt as soon as the crystallization temperature of magnetite is reached. It can be noted that this temperature is significantly lower at QFM than $MnO-Mn_3O_4$ buffer conditions.

3.5. Conclusions

The comparison of crystallization experiments at QFM and $MnO-Mn_3O_4$ buffer conditions in a MORB system shows that water has no stabilizing effect on Fe-Ti oxides, in contrast to observations of Holloway and Burnham (1972) and Sisson and Grove (1993a) for calc-alkaline systems. Liquid lines of descent obtained at high and low fO_2 are controlled by the fO_2 rather than H_2O. Residual liquids from experiments conducted at an fO_2 corresponding to the

QFM buffer show a tholeiitic differentiation trend (due to the general absence of Fe-Ti oxides). Higher melt oxidation state (higher Fe^{3+}/Fe^{2+} ratio) in liquids obtained an fO_2 corresponding to the $MnO\text{-}Mn_3O_4$ buffer results in a relative early crystallization of magnetite. Consequently, the FeO*/MgO ratio continuously decreases with crystallization causing a calc-alkaline differentiation trend. Although fO_2 is the main parameter controlling the differentiation trends, it has been shown that aH_2O has a minor effect on melt FeO* enrichment, independently of fO_2. This is due to a general higher crystal/melt ratio at low aH_2O in the main crystallization interval (and only to a lesser extent to high plagioclase/Fe-Mg-silicate ratio). SiO_2–rich residual melts can be obtained under both, oxidizing and reducing fO_2 but at least one fractionation step is required to reach plagiogranitic residual melt compositions.

4. References

Andersen, D.J., Lindsley, D.H., and Davidson, P.M. (1993) QUILF: a PASCAL program to assess equilibria among Fe-Mg-Ti-oxides, pyroxenes, olivine and quartz. Computational Geosciences, 19, 1333-1350.

Arth, J.G., Barker, F., Peterman, Z.E., and Friedman, I. (1978) Geochemistry of the gabbro-diorite-tonalite-trondhjemite suite of tonalite and trondhjemite magmas. Journal of Petrology, 19, 289-316.

Bacon, C.R., and Hirschmann, M.M. (1988) Mg/Mn partitioning as a test for equilibrium between coexisting Fe-Ti oxides. American Mineralogist, 73, 57-61.

Baker, D.R., and Eggler, D.H. (1987) Compositions of anhydrous and hydrous melts coexisting with plagioclase, augite, and olivine or low-Ca pyroxene from 1 atm to 8 kbar: application to the Aleutian volcanic center of Atka. American Mineralogist, 72, 12-28.

Baker, L.L., and Rutherford, M.J. (1996) The effect of dissolved water on the oxidation state of silicic melts. Geochimica et Cosmochimica Acta, 60(12), 2179-2187.

Barnes, C.G., Barnes, M.A., and Kistler, W. (1992) Petrology of the Caribou Mountain pluton, Klamath Mountains, California. Journal of Petrology, 33, 95-124.

Beard, J.S., and Lofgren, G.N. (1991) Dehydration melting and water-saturated melting of basaltic and andesitic greenstones and amphibolites at 1, 3, and 6.9 kb. Journal of Petrology, 32, 365-401.

Behrens, H. (1995) Determination of Water Solubilities in High-Viscosity Melts - an Experimental-Study on $NaAlSi_3O_8$ and $KAlSi_3O_8$ Melts. European Journal of Mineralogy, 7(4), 905-920.

Behrens, H., and Schulze, F. (2000) Compositional dependence of water diffusivity in aluminosilicate glasses and melts. In D. Rammlmair, J. Mederer, T. Oberthür, R.B. Heimann, and H. Pentinghaus, Eds. Applied Mineralogy in Research, Economy, Technology, Ecology and Culture, 1, p. 95-98. A.A. Balkema Publishers Rotterdam.

Behrens, H., Romano, C., Nowak, M., Holtz, F., and Dingwell, D.B. (1996) Near-infrared spectroscopic determination of water species in glasses of system $MAlSi_3O_8$ (M=Li, Na, K): An interlaboratory study. Chemical Geology, 128(1-4), 41-63.

Berndt, J., Holtz, F., and Koepke, J. (2001) Experimental constraints on storage conditions in the chemically zoned phonolitic magma chamber of the Laacher See volcano. Contributions to Mineralogy and Petrology, 140(4), 469-486.

Berndt, J., Koepke, J., and Holtz, F. (2000) Phase Relationships and Differentiation of MORB up to 0.2 Gpa: Experimental Outline and First Results. Eighth International Symposium on Experimental Mineralogy, Petrology and Geochemistry, 5, p. 13. Journal of Conference Abstracts, Cambridge Publications, Bergamo.

Brooks, C.K., Larsen, L.M., and Nielsen, T.F.D. (1991) Importance of iron-rich tholeiitic magmas at divergent plate margins: A reappraisal. Geology, 19, 269-272.

Bryan, W.B., and Moore, J.G. (1977) Compositional variations of young basalts in the Mid-Atlantic Ridge rift valley near lat. 36°49´N. Bulletin of the Geological Society of America, 88, 556-570.

Burnham, C.W. (1979) The importance of volatile constituents. The evolution of the igneous rocks, 16. Princeton University Press.

Burnham, C.W., Holloway, J.R., and Davis, N.F. (1969) Thermodynamic Properties of Water to 1,000°C and 10,000 Bars. The Geological Society of America.

Carmichael, I.S.E., and Ghiorso, M.S. (1986) Oxidation-reduction relations in basic magma: a case for homogeneous equilibria. Earth and Planetary Science Letters, 78, 200-210.

Carmichael, I.S.E., Turner, F.J., and Verhoogen, J. (1974) Igneous Petrology. 739 p. University of California, Berkely.

Chekhmir, A.S., Persikov, M.B., Epel´baum, M.B., and Bukhtiyarov, P.G. (1985) Hydrogen transport through a model magma. Geokhimiya, 5, 594-598.

Chou, I.-M. (1978) Calibration of oxygen buffers at elevated P and T using the hydrogen fugacity sensor. American Mineralogist, 63, 690-703.

Chou, I.-M. (1986) Permeability of precious metals to hydrogen at 2 kb total pressure and elevated temperatures. American Journal of Science, 286, 638-658.

Christie, D.M., and Sinton, J.M. (1986) Major elements constraints on melting, differentiation and mixing of magmas from the Galapagos 95.5°W propagating rift system. Contributions to Mineralogy and Petrology, 94, 274-288.

Christie, D.M., Carmichael, I.S.E., and Langmuir, C.H. (1986) Oxidation state of mid-ocean ridge basalt glasses. Earth and Planetary Science Letters, 79, 397-411.

Coleman, R.G., and Peterman, Z.E. (1975) Oceanic plagiogranite. Journal of geophysical Research, 80, 1099-1108.

Danyushevsky, L.V., Sobolev, A.V., and Dmitriev, L.V. (1996) Estimation of the pressure of crystallization and H2O content of MORE and BABB glasses: Calibration of an empirical technique. Mineralogy and Petrology, 57(3-4), 185-204.

Danyushevsky, L.V., Eggins, S.M., Falloon, T.J., and Christie, D.M. (2000) H_2O abundance in depleted to moderately enriched mid-ocean ridge magmas; Part I: Incompatible behaviour, implications for mantle storage, and origin of regional variations. Journal of Petrology, 41(8), 1329-1364.

Devine, J.D., Gardner, J.E., Brack, H.P., Layne, G.D., and Rutherford, M.J. (1995) Comparison of microanalytical methods for estimating H_2O contents of silicic volcanic glasses. American Mineralogist, 80, 319-328.

Dick, H.J.B., Meyer, P.S., Bloomer, S., Kirby, S., Stakes, D., and Mawer, C. (1991) Lithostratigraphic evolution of an in-situ section of oceanic layer 31. In R.P. Von Herzen, P.T. Robinson, J. Fox, and A. Palmer-Julson, Eds. Proceedings of the ocean d rilling program: Scientific Results, 118, p. 439-538. College Station, TX (Ocean Drilling Program).

Dixon, J.E., Stolper, E.M., and Holloway, J.R. (1995) An Experimental Study of Water and Carbon Dioxide Solubilities in Mid-Ocean Ridge Basaltic Liquids. Part I: Calibration and Solubility Models. Journal of Petrology, 36(6), 1607-1631.

Dixon, S., and Rutherford, M.J. (1979) Plagiogranites as late-stage immiscible liquids in ophiolite and mid-ocean ridge suites: an experimental study. Earth and Planetary Science Letters, 45, 45-60.

Elthon, D. (1991) Experimental phase petrology of mid-ocean ridge basalts. In P.A. Floyd, Ed. Oceanic Basalts, p. 94-115. Blackie and Son, Glasgow and London.

Eugster, H.P. (1957) Heterogeneous reactions involving oxidation and reduction at high pressures and temperatures. Journal of Chemical Physics, 26, 1760-1761.

Eugster, H.P., and Wones, D.R. (1962) Stability Relations of the Ferruginous Biotite, Annite. Journal of Petrology, 3(1), 82-125.

Fisk, M.R. (1984) Depths and temperatures of mid-ocean-ridge magma chambers and the composition of their source magmas. In I.G. Gass, S.J. Lippard, and A.W. Shelton, Eds. Ophiolites and Oceanic Lithosphere, p. 17-23. The Geological Society by Blackwell Scientific Publications, Oxford London Edinburgh Boston Melbourne.

Flagler, P.A., and Spray, J.G. (1991) Generation of plagiogranite by amphibolite anatexis in oceanic shear zones. Geology, 19, 70-73.

Ford, C.E. (1978) Platinum-iron alloy sample containers for melting experiments on iron-bearing rocks, minerals, and related systems. Mineralogical Magazine, 42, 271-275.

Frantz, J.D., Ferry, J.M., Popp, R.K., and Hewitt, D.A. (1977) Redesign of the Shaw apparatus for controlled hydrogen fugacity during hydrothermal experimentation. Carnegie Institution of Washington Year Book, 76, 660-662.

Frey, F.A., Bryan, W.B., and Thompson, G. (1974) Atlantic Ocean floor, geochemistry and petrology of basalts from leg 2 and 3 of the Deep Sea Drilling Project. Journal of Geophysical Research, 79, 5507-5527.

Gaetani, G.A., Grove, T.L., and Bryan, W.B. (1993) The influence of water on the petrogenesis of subduction-related igneous rocks. Nature, 365, 332-335.

Gaillard, F., Scaillet, B., Pichavant, M., and Beny, J.L. (2001) The effect of water and fO$_2$ on the ferric-ferrous ratio of silicic melts. Chemical Geology, 174(1-3), 255-273.

Gardien, V., Thompson, A.B., Grujic, G., and Ulmer, P. (1995) Experimental melting of biotite + plagioclase + quartz ± muscovite assemblages and implications for crustal melting. Journal of Geophysical research, 100(15581-15591).

Grove, T.L. (1981) Use of FePt Alloys to Eliminate the Iron Loss Problem in 1 Atmosphere Gas Mixing Experiments: Theoretical and Practical Considerations. Contributions to Mineralogy and Petrology, 78, 298-304.

Grove, T.L., and Bryan, W.B. (1983) Fractionation of pyroxene-phyric MORB at low pressure: An experimental study. Contributions to Mineralogy and Petrology, 84, 293-309.

Grove, T.L., and Baker, M.B. (1984) Phase equilibrium controls on the tholeiitic versus calc-alkaline differentiation trends. Journal of Geophysical Research, 89, 3253-3274.

Grove, T.L., and Juster, T.C. (1989) Experimental investigations of low-Ca pyroxene stability and olivine-pyroxene-liquid equilibria at 1-atm in natural basaltic and andesitic liquids. Contributions to Mineralogy and Petrology, 103, 287-305.

Gunter, M.D., Myers, J., and Girsperberg, S. (1987) Hydrogen: Metal membranes. In G.C. Ulmer, Barnes, H.L., Ed. Hydrothermal experimental techniques, p. 100-120. Wiley, New York.

Gunter, M.D., Myers, J., and Wood, J.R. (1979) The Shaw bomb, an ideal hydrogen sensor. Contributions to Mineralogy and Petrology, 70, 23-27.

Hamilton, D.L., Burnham, C.W., and Osborn, E.F. (1964) The Solubility of Water and Effects of Oxygen Fugacity and Water Content on Crystallization in Mafic Magmas. Journal of Petrology, 5(1), 21-39.

Harvie, C., Weare, J.H., and O`Keefe, M. (1980) Permeation of hydrogen through platinum: a re-evaluation of the data of Chou et al. Geochimica et Cosmochimica Acta, 44, 899-900.

Helz, R.T. (1973) Phase Relations of Basalts in their Melting Range at PH$_2$O=5kb as a Function of Oxygen Fugacity. Part I. Mafic phases. Journal of Petrology, 14(2), 249-302.

Helz, R.T. (1976) Phase Relations of Basalts in their Melting Range at PH$_2$O=5kb. Part II. Melt Compositions. Journal of Petrology, 17(2), 139-193.

Helz, R.T. (1981) Phase relations and compositions of amphiboles produced in studies of the melting behavior of rocks. In P.H. Ribbe, and D.R. Veblen, Eds. Reviews in Mineralogy; Amphiboles: petrology and experimental phase relations, 9B, p. 279-353. Minerlogical Society of America.

Hewitt, D.A. (1977) Hydrogen Fugacities in Shaw Bomb Experiments. Contributions to Mineralogy and Petrology, 65, 165-169.

Hewitt, D.A. (1978) A redetermination of the fayalite-magnetite-quartz equilibrium between 650 and 850°C. American Journal of Science, 278, 715-724.

Hill, R., and Roeder, P.L. (1974) The crystallization of spinel from basaltic liquid as a function of oxygen fugacity. Journal of Geology, 82, 709-729.

Holleck, G.L. (1970) Diffusion and solubility of hydrogen in palladium and palladium-silver alloys. Journal of Physical Chemistry, 74, 503-511.

Holloway, J.R. (1971) Internally heated pressure vessels. In G.C. Ulmer, Ed. Research techniques for high temperature and pressure, p. 217-258. Springer Verlag, New York.

Holloway, J.R., and Burnham, C.W. (1972) Melting Relations of Basalt with Equilibrium Water Pressure Less Than Total Pressure. Journal of Petrology, 13(1), 1-29.

Holloway, J.R., and Wood, B.J. (1988) Simulating the Earth, Experimental Geochemistry. 196 p. Unwin Hyman Inc., London.

Holloway, J.R., Dixon, J.E., and Pawley, A.R. (1992) An internally heated, rapid-quench, high-pressure vessel. American Mineralogist, 77, 643-646.

Holtz, F., Behrens, H., Dingwell, D.B., and Johannes, W. (1995) H_2O Solubility in Haplogranitic Melts - Compositional, Pressure, and Temperature-Dependence. American Mineralogist, 80(1-2), 94-108.

Hoover, J.D., and Irvine, T.N. (1977) Liquidus relations and Mg-Fe partitioning on part of the system Mg_2SiO_4-Fe_2SiO_4-$CaMgSi_2O_6$-$CaFeSi_2O_6$-$KAlSi_3O_8$-SiO_2. Carnegie Institution of Washington Year Book, 77, 774-784.

Irvine, T.N., and Baragar, W.R.A. (1971) A guide to chemical classification of the common volcanic rocks. Canadian Journal of Earth Science, 8, 523-548.

Jenner, G.A., Dunning, G.R., Malpas, J., Brown, M., and Brace, T. (1991) Bay of Islands and Little Port complexes, revisited: age, geochemical and isotopic evidence confirm suprasubduction-zone origin. Canadian Journal of Earth Science, 28, 1635-1652.

Johannes, W., and Bode, B. (1978) Loss of iron to the Pt-container in melting experiments with basalts and a method to reduce it. Contributions to Mineralogy and Petrology, 67, 221-225.

Johnson, M.C., Andersen, A.T.J., and Rutherford, M.J. (1994) Pre-eruptive volatile contents of magmas. In M.R. Carroll, and J.R. Holloway, Eds. Reviews in Mineralogy

Jurewicz, A.J.G., and Watson, E.B. (1988) Cations in olivine, Part 1: Calcium partitioning and calcium-magnesium distribution between olivines and coexisting melts, with petrologic applications. Contributions to Mineralogy and Petrology, 99, 176-185.

Juster, T.C., Grove, T.L., and Perfit, M.R. (1989) Experimental Constraints on the Generation of FeTi Basalts, Andesites, and Rhyodacites at the Galapagos Spreading Center, 85°W and 95°W. Journal of geophysical research, 94(B7), 9251-9274.

Kawamoto, T. (1996) Experimental constraints on differentiation and H_2O abundance of calc-alkaline magmas. Earth and Planetary Science Letters, 144, 577-589.

Kawamoto, T., and Hirose, K. (1994) Au-Pd sample containers for melting experiments on iron and water bearing systems. European Journal of Mineralogy, 6, 381-385.

Koepke, J. (1997) Analyse von wasserhaltigen silikatischen Gläsern mit der Mikrosonde: Wassergehalte und Alkalienverluste. Berichte der Deutschen Mineralogischen Gesellschaft, Beiheft in European Journal of Mineralogy, 9, 200.

Koepke, J., Johannes, W., and Becker, A. (1996) Determination of crystal/melt fractions with the help of BSE-pictures and image analysis. Terra Nova, Abstract Supplement, 8, 36.

Kovalenko, V.I., Naumov, V.B., Yarmolyuk, V.V., and Dorofeeva, V.A. (2000) Volatile components (H_2O, CO_2, Cl, F, and S) in magmas of intermediate and acid compositions from distinct geodynamic settings: Evidence from melt inclusions and chill glasses. Petrology, 8(6), 525-556.

Kress, V.C., and Carmichael, I.S.E. (1991) The compressibility of silicate liquids containing Fe_2O_3 and the effect of composition, temperature, oxygen fugacity and pressure on their redox states. Contributions to Mineralogy and Petrology, 108, 82-92.

Kushiro, I. (1975) On the nature of silicate melts and its significance in magma genesis: Regularities in the shift of liquidus boundaries involving olivine, pyroxene, and silica materials. American Journal of Science, 275, 411-432.

Lange, R.A. (1997) A revised model for the density and thermal expansivity of K_2O-Na_2O-CaO-MgO-Al_2O_3-SiO_2 liquids from 700 to 1900 K: extension to crustal magmatic t emperatures. Contributions to Mineralogy and Petrology, 130, 1-11.

Lange, R.A., and Carmichael, I.S.E. (1990) Thermodynamic properties silicate liquids with emphasis on density, thermal expansion and compressibility. In P.H. Ribbe, Ed. Reviews in Mineralogy; Modern Methods of Igneous Petrology: Understanding Magmatic Processes, 24, p. 25-64. Mineralogical Society of America.

Langmuir, C.H., Bender, J.F., Bence, A.E., and Hanson, G.N. (1977) Petrogenesis of basalt from the FAMOUS are, Mid-Atlantic, Ridge. Earth and Planetary Science Letters, 36, 133-156.

Leake, B.E., Woolley, A.R., Birch, W.D., Gilbert, M.C., Grice, J.D., Hawthorne, F.C., Kato, A., Kisch, H.J., Krivovichev, V.G., Linthout, K., Laird, J., Mandarino, J., Maresch,

W.V., Nickel, E.H., Rock, N.M.S., Schumacher, J.C., Smith, D.C., Stephenson, N.C.N., Ungaretti, L., Whittaker, E.J.W., and Youzhi, G. (1997) Nomenclature of amphiboles - Report of the subcommittee on Amphiboles of the International Mineralogical Association Commission on New Minerals and Mineral Names. European Journal of Mineralogy, 9(3), 623-651.

Libourel, G. (1999) Systematics of calcium partitioning between olivine and silicate melt: implications for melt structure and calcium content of magmatic olivines. Contributions to Mineralogy and Petrology, 136, 63-80.

Longhi, J., Walker, D., and Hays, J.F. (1978) The distribution of Fe and Mg between olivine and lunar basaltic liquids. Geochimica et Cosmochimica Acta, 42, 1545-1558.

Longhi, J., and Pan, V. (1988) A reconnaisance study of phase boundaries in low-alkali basaltic liquids. Journal of Petrology, 29, 115-147.

Maestas, S., and Flanagan, T.B. (1973) Diffusion of Hydrogen in Gold-Palladium alloys. Journal of Physical Chemistry, 77(6), 850-854.

Malpas, J. (1979) Two contrasting trondhjemite associations from transported ophiolites in western Newfoundland: initial report. In F. Barker, Ed. Trondhjemites, dacites, and related rocks, p. 465-484. Elsevier, Amsterdam.

Martel, C., Pichavant, M., Bourdier, J.-L., Traineau, H., Holtz, F., and Scaillet, B. (1998) Magma storage conditions and control of eruption regime in silicic volcanoes: experimental evidence from Mt. Pelee. Earth and Planetary Science Letters, 156, 89-99.

Martin, H. (1987) Petrogenesis of Archean trondhjemites, tonalites, and granodiorites from Eastern Finland: major and trace element geochemistry. Journal of Petrology, 28, 921-953.

McKenzie, D.P., and Bickle, M.J. (1988) The volume and composition of melt generated by extension of the lithosphere. Journal of Petrology, 29, 625-679.

4. References
_____

Miyashiro, A. (1974) Volcanic rock series in island arcs and active continental margins. American Journal of Science, 274, 321-355.

Miyashiro, A., Shido, F., and Ewing, M. (1969) Diversity and Origin of Abyssal Tholeiite from the Mid-Atlantic Ridge near 24° and 30° North Latitude. Contributions to Mineralogy and Petrology, 23, 38-52.

Morimoto, N. (1988) Nomenclature of pyroxenes. Mineralogical Magazine, 52, 535-550.

Natland, J.H., and Melson, W.G. (1980) Compositions of basaltic glasses from the East Pacific Rise and the Siqueiros Fracture Zone, near 9°. In B.R. Rosendahl, Ed. Initial Reports of the Deep Sea Drilling Project.

Nicolas, A. (1989) Structures of Ophiolites and Dynamics of Oceanic Lithosphere. 367 p. Kluwer Academic Publishers, Dordrecht, Boston, London.

Ochs III, F.A., and Lange, R.A. (1999) The Density of Hydrous Magmatic Liquids. Science, 283, 1314-1317.

Ohlhorst, S., Behrens, H., Berndt, J., and Holtz, F. (2000) Volatiles in rhyolitic to basaltic melts: Calibration of IR spectroscopy and H_2O solubility. Eighth International Symposium on Experimental Mineralogy, Petrology and Geochemistry, 5, p. 79. Journal of Conference Abstracts, Cambridge Publications, Bergamo.

Osborn, E.F. (1959) Role of oxygen pressure in the crystallization and differentiation of basaltic magma. American Journal of Science, 257, 609-647.

Panjasawatwong, Y., Danyushevsky, L.V., Crawford, A.J., and Harris, K.L. (1995) An experimental stdy of the effects of melt composition on plagioclase - melt equilibria at 5 and 10 kbar: implications for the origin of magmatic high-An plagioclase. Contributions to Mineralogy and Petrology, 118, 420-432.

Pichavant, M. (1987) Effects of B and H_2O on liquidus phase relations in the haplogranite system at 1 kbar. American Mineralogist, 72, 11-12.

Pitzer, K.S., and Sterner, S.M. (1994) Equation of state valid continuously from zero to extreme pressures for H_2O and CO_2. Journal of Chemical Physics, 102, 3111-3116.

Piwinskii, A.J., Weidner, J.R., and Carman, J.H. (1973) An osmotic membran for hydrogen pressure measurements at elevated temperatures and pressures. Journal of Physics E: Scientific Instruments, 6, 603.

Presnall, D.C. (1966) The join forsterite-diopside-iron oxide and its bearing on the crystallization of basaltic and ultramafic magmas. American Journal of Science, 264, 753-809.

Ratajeski, K., and Sisson, T.W. (1999) Loss of iron to gold capsules in rock melting experiments. American Mineralogist, 84, 1521-1527.

Robertson, W.M. (1972) Hydrogen permeation, diffusion and solution in pure nickel and a nickel based superalloy. International Meeting on Hydrogen in Metals, Conference 6, 449-491.

Robie, R.A., Hemingway, B.S., and Fisher, J.R. (1978) Thermodynamic properties of minerals and related substances at 298.15 K and 1 bar (105 Pascals) pressure and at higher temperature. Geological Survey Bulletin, 1452, 456.

Roeder, P.L. (1974) Activity of iron and olivine solubility in basaltic liquids. Earth and Planetary Science Letters, 23, 397-410.

Roeder, P.L., and Emslie, R.F. (1970) Olivine-Liquid Equilibrium. Contributions to Mineralogy and Petrology, 29, 275-289.

Roux, J., and Lefevre, A. (1992) A fast-quench device for internally heated pressure vessels. European Journal of Mineralogy, 4, 279-281.

Sakamoto, Y., Hirata, S., and Nishikawa, H. (1982) Diffusivity and solubility of hydrogen in Pd-Ag and Pd-Au alloys. Journal of the Less-common Metals, 88, 387-395.

Scaillet, B., and Evans, B.W. (1999) The 15 June 1991 Eruption of Mount Pinatubo. I. Phase Equilibria and Pre-eruption P-T-fO$_2$-fH$_2$O Conditions of the Dacite Magma. Journal of Petrology, 40(3), 381-411.

Scaillet, B., Pichavant, M., and Roux, J. (1995) Experimental Crystallization of Leucogranite Magmas. Journal of Petrology, 36(3), 663-705.

Scaillet, B., Pichavant, M., Roux, J., Humbert, G., and Lefevre, A. (1992) Improvements of the Shaw membrane technique for measurement and control of fH$_2$ at high temperatures and pressures. American Mineralogist, 77, 647-655.

Schmidt, B.C., Scaillet, B., and Holtz, F. (1995) Accurate control of fH$_2$ in cold-seal pressure vessels with the Shaw membrane technique. European Journal of Mineralogy, 7, 893-903.

Schmidt, B.C., Holtz, F., and Pichavant, M. (1999) Water solubility in haplogranitic melts coexisting with H$_2$O-H$_2$ fluids. Contributions to Mineralogy and Petrology, 136(3), 213-224.

Schulze, F., Behrens, H., and Hurkuck, W. (1999) Determination of the influence of pressure and dissolved water on the viscosity of highly viscous melts: Application of a new parallel-plate viscometer. American Mineralogist, 84, 1512-1520.

Schwab, R.G., and Küstner, D. (1981) The equilibrium fugacities of important oxygen buffers in technology and petrology. Neues Jahrbuch für Mineralogie, 140, 112-142.

Shaw, H.R. (1963) Hydrogen-Water Vapor Mixtures: Control of Hydrothermal Atmospheres by Hydrogen Osmosis. Science, 139, 1220-1222.

Shaw, H.R., and Wones, D.R. (1964) Fugacity coefficients for hydrogen gas between 0°C and 1000°C, for pressures to 3000 atm. American Journal of Science, 262, 918-929.

Shi, P. (1993) Low-Pressure Phase Relationships in the System Na$_2$O-CaO-FeO-MgO-Al$_2$O$_3$-SiO$_2$ at 1100°C, with Implications for the Differentation of Basaltic Magmas. Journal of Petrology, 34(4), 743-762.

Sisson, T.W., and Grove, T.L. (1993a) Experimental investigations of the role of H$_2$O in calc-alkaline differentiation and subduction zone magmatism. Contributions to Mineralogy and Petrology, 113, 143-166.

Sisson, T.W., and Grove, T.L. (1993b) Temperatures and H_2O contents of low-MgO high-alumina basalts. Contributions to Mineralogy and Petrology, 113, 167-184.

Snyder, D.A., and Carmichael, I.S.E. (1992) Olivine-liquid equilibria and the chemical activities of FeO, NiO, Fe_2O_3, and MgO in natural nasic melts. Geochimica et Cosmochimica Acta, 56, 303-318.

Snyder, D., Carmichael, M.J., and Wiebe, R.A. (1993) Experimental study of liquid evolution in an Fe-rich, layered mafic intrusion: constraints of Fe-Ti oxide precipitation on the T-fO_2 and T-ρ paths of tholeiitic magmas. Contributions to Mineralogy and Petrology, 113, 73-86.

Sobolev, A.V., and Chaussidon, M. (1996) H_2O concentrations in primary melts from supra-subduction zones and mid-ocean ridges: Implications for H_2O storage and recycling in the mantle. Earth and Planetary Science Letters, 137(1-4), 45-55.

Springer, W., and Seck, H.A. (1997) Partial fusion of basic granulites at 5 to 15 kbar: implications for the origin of TTG magmas. Contributions to Mineralogy and Petrology, 127, 30-45.

Spulber, S.D., and Rutherford, M.J. (1983) The Origin of Rhyolite and Plagiogranite in Oceanic Crust: An Experimental Study. Journal of Petrology, 24(1), 1-25.

Stormer, J.C., Jr. (1983) The effects of recalculation on estimates of temperature and oxygen fugacity from analyses of multicomponent iron-titanium oxides. American Mineralogist, 68, 586-594.

Taylor, J.R., Wall, V.J., and Pownceby, M.I. (1992) The calibration and application of accurate redox sensors. American Mineralogist, 77, 284-295.

Thy, P., and Lofgren, G.E. (1994) Experimental constraints on the low-pressure evolution of transitional and mildly alkalic basalts: the effect of Fe-Ti oxide minerals and the origin of basaltic andesites. Contributions to Mineralogy and Petrology, 116, 340-351.

Toplis, M.J., and Carroll, M.R. (1995) An Experimental Study of the Influence of Oxygen Fugacity on Fe-Ti Oxide Stability, Phase Relations, and Mineral-Melt Equilibria in Ferro-Basaltic Systems. Journal of Petrology, 36(5), 1137-1170.

Toplis, M.J., and Carroll, M.R. (1996) Differentiation of Ferro-Basaltic Magmas under Conditions Open and Closed to Oxygen: Implications for the Skaergaard Intrusion and Other Natural Systems. Journal of Petrology, 37(4), 837-858.

Tormey, D.R., Grove, T.L., and Bryan, W.B. (1987) Experimental petrology of normal MORB near the Kane Fracture Zone: 22°-25° N, mid-Atlantic ridge. Contributions to Mineralogy and Petrology, 96, 121-139.

Turner, F.J., and Verhoogen, J. (1960) Igneous and Metamorphic Petrology. 694 p. McGraw Hill Book Company, New York.

Ulmer, P. (1989) The dependence of the Fe2+-Mg cation-partitioning between olivine and basaltic liquid on pressure, temperature and composition. Contributions to Mineralogy and Petrology, 101, 261-273.

Watson, E.B. (1979) Calcium content of forsterite coexisting with silicate liquid in the system Na_2O-CaO-MgO-Al_2O_3-SiO_2. American Mineralogist, 64, 824-829.

Webster, J.D., Kinzler, R.J., and Mathez, E.A. (1999) Chloride and water solubility in basalt and andesite melts and implications for magmatic degassing. Geochimica et Cosmochimica Acta, 63(5), 729-738.

Wilson, M. (1989) Igneous petrogenesis. Unwin Hyman, London.

Wiser, N.M., and Wood, B.J. (1991) Experimental determination of activities in Fe-Mg olivine at 1400 K. Contributions to Mineralogy and Petrology, 108, 146-153.

Yang, H.-J., Kinzler, R.J., and Grove, T.L. (1996) Experiments and models of anhydrous, basaltic olivine-plagioclase-augite saturated melts from 0.001 to 10 kbar. Contributions to Mineralogy and Petrology, 124, 1-18.

Yoder, H.S., Jr., and Tilley, C.E. (1962) Origin of Basalt Magmas: An Experimental Study of Natural and Synthetic Rock Systems. Journal of Petrology, 3(3), 342-532.

Yoder, H.S. (1965) Diopside-anorthite-water at five and ten kilobars and its bearing on explosive volcanism. Carnegie Institution of Washington Year Book, 64, 82-89.

Zhang, Y., and Stolper, E.M. (1991) Water diffusion in a basaltic melt. Nature, 351, 306-309.

Zhang, Y., Zhengjiu, X., and Behrens, H. (2000) Hydrous species geospeedometer in rhyolite: Improved calibration and application. Geochimica et Cosmochimica Acta, 64(19), 3347-3355.

5. Tables

Table 2.4. Experimental olivine compositions (MnO-Mn$_3$O$_4$ buffer)

	B1																
Experiment:	65		64		63		45		44		43		42		62		61	
T(°C):	1150		1150		1150		1100		1100		1100		1100		1100		*1100*	
wt% H$_2$O in melt:	2.56		1.54		1.01		*4.57*		3.13		2.45		1.79		*4.56*		1.72	
aH$_2$O:	0.47		0.21		0.10		1		0.61		0.43		0.27		1		0.25	
n:	4		5		4		8		6		6		7		3		2	
wt%																		
SiO$_2$	41.48	0.21	41.24	0.31	41.35	0.22	41.49	0.20	40.82	0.11	40.18	0.23	39.98	0.24	41.24	0.23	40.12	0.04
TiO$_2$	0.04	0.02	0.02	0.02	0.01	0.02	0.03	0.02	0.02	0.01	0.02	0.02	0.03	0.04	0.03	0.01	0.06	0.04
Al$_2$O$_3$	0.04	0.02	0.05	0.03	0.05	0.04	0.04	0.02	0.08	0.03	0.10	0.08	0.08	0.11	0.05	0.02	0.14	0.17
FeO	8.41	0.05	10.00	0.22	11.26	0.09	6.72	0.18	10.14	0.21	13.13	0.19	14.68	0.14	6.71	0.14	14.69	0.28
MnO	0.15	0.02	0.18	0.04	0.20	0.05	0.21	0.05	0.22	0.08	0.29	0.05	0.29	0.02	0.31	0.07	0.37	0.09
MgO	50.45	0.15	49.08	0.12	48.07	0.15	51.34	0.40	48.83	0.60	44.89	0.73	43.64	0.42	51.44	0.14	43.66	0.21
CaO	0.33	0.02	0.34	0.04	0.41	0.03	0.23	0.02	0.33	0.04	0.36	0.03	0.36	0.04	0.24	0.03	0.35	0.08
Na$_2$O	0.02	0.02	0.01	0.00	0.01	0.01	0.01	0.01	0.01	0.01	0.02	0.01	0.01	0.01	0.00	0.01	0.01	0.01
K$_2$O	0.01	0.00	0.01	0.01	0.01	0.01	0.01	0.01	0.01	0.01	0.01	0.01	0.00	0.00	0.00	0.00	0.01	0.01
Total	100.93		100.93		101.39		100.07		100.45		99.00		99.09		100.03		99.40	
XFo[a]	91.45		89.74		88.38		93.16		89.68		85.90		84.12		93.39		84.12	
Kd Ol-Melt/Mg-Fe[b]	0.334		0.349		0.331		0.319		0.327		0.339		0.335		0.318		0.343	

	B1															
Experiment:	41		40		39		38		37		36		35		34	
T(°C):	1050		1050		1050		1050		1000		1000		1000		1000	
wt% H$_2$O in melt:	4.73		*4.84*		3.63		2.34		*5.09*		*5.08*		*5.21*		*5.19*	
aH$_2$O:	1		1		0.70		0.38		1		1		1		1	
n:	3		6		2		2		2		2		3		2	
wt%																
SiO$_2$	41.19	0.06	40.44	0.25	40.13	0.23	39.75	0.11	41.16	0.10	40.90	0.41	41.07	0.13	40.89	0.00
TiO$_2$	0.02	0.03	0.02	0.01	0.05	0.06	0.02	0.02	0.03	0.04	0.04	0.02	0.04	0.01	0.04	0.00
Al$_2$O$_3$	0.04	0.03	0.05	0.03	0.35	0.30	0.08	0.03	0.07	0.04	0.24	0.28	0.25	0.26	0.60	0.60
FeO	9.90	0.14	11.92	0.21	14.24	0.24	15.60	0.28	9.66	0.68	11.61	0.01	13.15	0.17	13.10	0.23
MnO	0.30	0.09	0.31	0.04	0.32	0.04	0.41	0.06	0.33	0.08	0.31	0.00	0.38	0.05	0.37	0.09
MgO	46.70	0.52	44.76	0.63	45.13	0.62	43.40	0.47	49.16	0.91	46.86	0.72	44.37	0.38	43.34	1.25
CaO	0.19	0.03	0.29	0.05	0.32	0.00	0.32	0.03	0.20	0.05	0.24	0.04	0.23	0.04	0.19	0.04
Na$_2$O	0.02	0.02	0.01	0.01	0.05	0.01	0.05	0.02	0.01	0.01	0.04	0.03	0.03	0.03	0.06	0.03
K$_2$O	0.01	0.01	0.01	0.00	0.00	0.00	0.01	0.01	0.01	0.00	0.01	0.01	0.01	0.01	0.01	0.01
Total	98.37		97.81		100.61		99.63		100.61		100.24		99.53		98.61	
XFo[a]	89.37		87.00		84.96		83.22		90.07		87.80		85.74		85.50	
Kd Ol-Melt/Mg-Fe[b]	0.338		0.327		0.311		0.330		0.325		0.338		0.332		0.314	

[a] XFo x 100

[b] partition coefficient describing the distribution of iron and magnesium between melt and coexisting olivine defined as
(XOl-FeO/XMelt-FeO) x (XMelt-MgO/XOl-MgO) after Roeder and Emslie (1970)

5. Tables

Table 2.5. Experimental clinopyroxene compositions (MnO-Mn$_3$O$_4$ buffer)

B1

Experiment:	63		44		43		42		61		41		40		39		38	
T(°C):	1150		1100		1100		1100		1100		1050		1050		1050		1050	
wt% H$_2$O in melt:	1.01		3.13		2.45		1.79		1.72		4.73		4.84		3.63		2.34	
aH$_2$O:	0.1		0.61		0.43		0.27		0.25		1		1		0.70		0.38	
n:	4		4		5		5		2		3		3		3		5	
wt%																		
SiO$_2$	51.67	0.31	48.08	0.32	49.09	0.62	49.29	0.39	49.38	0.25	49.49	0.58	51.36	0.24	49.36	0.70	49.53	0.46
TiO$_2$	0.47	0.09	0.55	0.08	0.63	0.03	0.61	0.05	0.60	0.01	0.64	0.18	0.46	0.21	0.76	0.07	0.87	0.15
Al$_2$O$_3$	4.50	0.15	6.70	0.16	5.76	0.58	5.28	0.28	5.28	0.34	5.88	0.33	4.01	0.35	5.18	0.36	5.74	0.29
FeO*	6.11	0.38	7.61	0.26	7.79	0.37	8.16	0.30	8.17	0.19	6.75	0.05	6.40	0.01	7.89	0.11	8.58	0.87
MnO	0.18	0.05	0.09	0.04	0.15	0.05	0.19	0.04	0.20	0.01	0.28	0.03	0.19	0.05	0.25	0.01	0.20	0.03
MgO	16.84	0.14	14.74	0.18	14.71	0.49	15.13	0.23	15.28	0.08	15.20	0.56	15.18	0.00	15.59	0.26	15.09	0.10
CaO	21.11	0.56	21.73	0.14	20.84	0.40	20.40	0.30	20.30	0.25	21.22	0.46	21.97	0.51	20.16	0.24	18.89	0.04
Na$_2$O	0.25	0.03	0.27	0.04	0.37	0.06	0.36	0.03	0.35	0.04	0.32	0.05	0.29	0.06	0.36	0.06	0.39	0.09
K$_2$O	0.01	0.01	0.00	0.01	0.01	0.01	0.01	0.01	0.01	0.01	0.00	0.00	0.01	0.00	0.00	0.00	0.01	0.01
Total	101.14		99.77		99.35		99.43		99.55		99.77		99.86		99.55		99.30	
En [a]	47.39		42.51		43.08		43.89		44.21		44.19		43.80		44.99		44.91	
Fs	9.93		12.46		13.05		13.59		13.58		11.46		10.66		13.19		14.67	
Wo	42.68		45.03		43.87		42.52		42.21		44.35		45.54		41.83		40.42	
Mg#[b]	88.81		91.25		85.48		85.79		85.78		87.89		84.21		87.03		79.65	

B1

Experiment:	37		36		35		34		49		48		47		46	
T(°C):	1000		1000		1000		1000		950		950		950		950	
wt% H$_2$O in melt:	5.09		5.08		5.21		5.19		5.19		5.25		5.24		5.24	
aH$_2$O:	1		1		1		1		1		1		1		1	
n:	2		3		2		3		3		2		3		2	
wt%																
SiO$_2$	48.57	0.04	49.27	0.15	50.46	0.73	50.10	0.40	51.13	1.32	51.57	0.41	52.37	0.09	52.39	0.91
TiO$_2$	0.76	0.03	0.86	0.03	0.93	0.18	1.00	0.03	0.67	0.07	0.72	0.02	0.62	0.04	0.61	0.11
Al$_2$O$_3$	6.19	0.06	5.15	0.29	4.47	0.50	4.51	0.43	5.10	0.16	4.62	0.15	4.53	0.04	4.60	0.09
FeO*	7.54	0.17	7.41	0.81	7.15	0.42	7.83	0.66	7.12	0.35	7.19	0.12	5.57	0.03	5.49	0.12
MnO	0.19	0.04	0.25	0.02	0.30	0.07	0.23	0.08	0.28	0.05	0.27	0.04	0.28	0.05	0.25	0.06
MgO	15.63	0.23	15.66	0.42	15.67	0.47	15.70	0.23	15.84	0.26	15.75	0.33	14.92	0.14	14.99	0.27
CaO	20.50	0.49	20.58	1.28	20.19	0.53	19.72	0.29	20.50	0.16	20.89	0.21	20.58	0.13	20.70	0.17
Na$_2$O	0.32	0.00	0.34	0.06	0.40	0.01	0.42	0.04	0.35	0.06	0.45	0.09	0.43	0.03	0.41	0.05
K$_2$O	0.01	0.01	0.00	0.00	0.00	0.00	0.00	0.01	0.01	0.01	0.00	0.00	0.03	0.01	0.03	0.01
Total	99.70		99.52		99.57		99.51		100.99		101.46		99.32		99.47	
En [a]	45.03		45.07		45.60		45.65		45.62		45.07		45.22		45.30	
Fs	12.50		12.37		12.18		13.15		11.95		11.98		9.94		9.74	
Wo	42.47		42.56		42.23		41.20		42.43		42.96		44.84		44.96	
Mg#[b]	90.47		88.74		84.30		83.89		84.15		84.54		82.69		82.96	

[a] calculated after Morimoto (1988)

[b] mg number for pyroxene defined as XMg/(XMg+XFe) x 100

Table 2.5. continued

	B2														
Experiment:	91		92		93		94		95		96		98		99	
T(°C):	1100		1100		1100		1050		1050		1050		1050		1000	
wt% H_2O in melt:	2.10		1.84		1.45		*4.80*		2.65		2.48		2.22		*5.06*	
aH_2O:	0.34		0.28		0.19		1		0.43		0.38		0.32		1	
n:	2		2		2		2		4		5		3		4	
wt%															
SiO_2	48.42	0.94	51.11	0.20	51.21	0.54	47.92	0.97	48.34	0.48	49.91	0.48	49.83	0.47	48.22	0.65
TiO_2	1.06	0.04	0.73	0.04	0.82	0.03	1.12	0.07	1.25	0.25	0.99	0.10	0.87	0.13	1.43	0.11
Al_2O_3	5.61	0.68	3.87	0.62	3.82	0.09	5.54	0.29	5.39	0.27	4.75	2.17	3.73	0.81	6.76	0.20
FeO*	8.98	0.01	8.21	0.06	9.78	0.05	8.20	0.07	7.78	0.47	8.06	0.15	7.42	0.49	6.59	0.74
MnO	0.27	0.01	0.30	0.05	0.35	0.03	0.18	0.07	0.28	0.03	0.41	0.03	0.47	0.01	0.26	0.04
MgO	14.65	0.59	17.01	0.87	16.98	0.07	14.07	0.07	15.21	0.29	15.16	1.35	15.75	0.22	14.26	0.28
CaO	20.12	0.64	17.78	0.56	16.66	0.63	22.64	0.07	20.48	0.19	19.93	0.55	19.43	0.78	22.71	0.38
Na_2O	0.45	0.03	0.42	0.05	0.42	0.02	0.37	0.06	0.46	0.06	0.59	0.18	0.41	0.20	0.41	0.04
K_2O	0.02	0.01	0.02	0.02	0.01	0.02	0.01	0.01	0.00	0.00	0.02	0.03	0.03	0.00	0.01	0.03
Total	99.58		99.45		100.05		100.05		99.19		99.82		97.94		100.63	
En [a]	42.70		49.19		49.03		40.15		44.15		44.29		46.12		41.41	
Fs	15.14		13.83		16.41		13.43		13.13		13.88		12.97		11.17	
Wo	39.57		35.77		40.49		43.64		42.72		41.83		40.91		47.42	
Mg# [b]	85.15		82.63		79.11		91.67		89.66		84.87		85.10		91.80	

	B2														
Experiment:	100		101		102		103		104		105		106		111	
T(°C):	1000		1000		1000		950		950		950		950		950	
wt% H_2O in melt:	*5.18*		*5.26*		4.23		*5.19*		*5.14*		*5.29*		*5.20*		*5.18*	
aH_2O:	1		1		0.78		1		1		1		1		1	
n:	4		4		3		2		3		2		2		2	
wt%															
SiO_2	49.66	0.47	51.03	0.34	52.46	1.64	48.80	0.45	48.70	0.67	51.09	1.05	51.00	0.91	50.32	1.04
TiO_2	1.36	0.19	0.87	0.14	1.13	0.11	0.94	0.04	1.08	0.17	1.08	0.15	1.08	0.17	1.03	0.15
Al_2O_3	4.68	1.04	3.28	0.19	5.90	0.31	5.83	0.44	5.44	0.03	4.84	0.29	6.86	0.36	4.70	0.25
FeO*	8.26	0.73	8.30	0.52	6.04	1.21	7.02	0.08	7.08	0.45	6.94	0.49	5.01	0.21	6.93	0.11
MnO	0.41	0.02	0.54	0.07	0.46	0.02	0.29	0.00	0.39	0.03	0.39	0.04	0.43	0.11	0.41	0.06
MgO	16.27	1.25	16.37	0.02	15.37	0.42	14.22	0.31	14.36	0.20	14.76	0.56	17.01	1.01	15.19	0.30
CaO	17.95	0.98	18.96	0.55	15.53	1.60	21.49	0.26	20.87	0.32	19.47	0.68	18.20	0.74	20.91	0.55
Na_2O	0.51	0.13	0.47	0.01	0.77	0.18	0.56	0.00	0.48	0.05	1.36	0.21	0.69	0.25	0.53	0.09
K_2O	0.01	0.00	0.01	0.01	0.06	0.03	0.01	0.01	0.02	0.02	0.04	0.02	0.05	0.02	0.00	0.01
Total	99.13		99.82		97.72		99.16		98.44		99.97		100.34		100.03	
En [a]	47.79		46.83		50.93		42.11		42.80		44.91		51.32		44.23	
Fs	14.31		14.19		12.09		12.14		12.49		12.52		9.22		12.01	
Wo	37.90		38.98		36.98		45.75		44.70		42.57		39.46		43.76	
Mg# [b]	83.34		83.93		81.94		88.12		85.99		86.89		87.03		86.23	

for notes see Table 2.5

Table 2.6. Experimental orthopyroxene compositions (MnO-Mn$_3$O$_4$ buffer)

	B1											B2	
Experiment:	35		34		49		48		47		46		96	
T(°C):	1000		1000		950		950		950		950		1050	
wt% H$_2$O in melt:	5.21		5.19		5.19		5.25		5.24		5.24		2.48	
aH$_2$O:	1		1		1		1		1		1		0.38	
n:	2		5		3		2		3		2		3	
wt%														
SiO$_2$	54.63	0.62	53.94	1.08	55.40	0.32	55.52	0.18	55.43	0.05	55.44	0.33	53.56	0.06
TiO$_2$	0.34	0.08	0.40	0.07	0.24	0.02	0.31	0.02	0.25	0.02	0.25	0.08	0.49	0.03
Al$_2$O$_3$	3.17	0.60	3.35	0.77	3.50	0.35	3.20	0.10	3.02	0.01	2.99	0.29	4.02	1.60
FeO*	9.99	0.03	9.98	0.34	8.35	0.29	8.55	0.08	9.17	0.02	9.30	0.13	10.92	0.49
MnO	0.33	0.01	0.34	0.06	0.35	0.05	0.47	0.09	0.41	0.01	0.45	0.01	0.44	0.07
MgO	29.32	0.54	28.87	0.72	30.81	0.54	30.01	0.54	29.22	0.02	29.99	0.44	27.35	1.50
CaO	2.00	0.40	1.82	0.25	1.60	0.27	1.71	0.18	1.60	0.02	1.60	0.19	2.29	0.62
Na$_2$O	0.05	0.01	0.09	0.04	0.21	0.30	0.08	0.00	0.04	0.00	0.04	0.03	0.24	0.15
K$_2$O	0.00	0.00	0.01	0.01	0.05	0.07	0.01	0.01	0.02	0.01	0.03	0.01	0.01	0.01
Total	99.84		98.80		100.52		99.86		99.17		100.09		99.34	
En [a]	80.22		80.27		83.62		82.67		81.74		81.91	81.74	77.31	
Fs	15.85		16.10		13.26		13.95		15.04		14.95	14.86	18.03	
Wo	3.93		3.63		3.12		3.38		3.23		3.14	3.40	4.66	
Mg# [b]	83.95		83.76		87.24		86.22		85.04		85.18		81.70	

	B2													
Experiment:	98		100		101		102		104		105	106	111	
T(°C):	1050		1000		1000		1000		950		950	950	950	
wt% H$_2$O in melt:	2.22		5.18		5.26		4.23		5.14		5.29	5.20	5.18	
aH$_2$O:	0.32		1		1		0.78		1		1	1	1	
n:	2		2		2		2		3		1	1	1	
wt%														
SiO$_2$	55.62	0.77	54.89	0.18	54.33	0.13	54.32	0.52	54.04	0.28	56.20	54.69	55.03	
TiO$_2$	0.46	0.08	0.39	0.03	0.31	0.00	0.31	0.03	0.35	0.13	0.33	0.33	0.35	
Al$_2$O$_3$	1.98	0.43	2.99	0.05	3.34	0.74	5.14	0.82	4.68	0.94	3.15	5.72	5.40	
FeO*	12.37	0.57	8.69	0.17	10.25	0.33	11.28	0.43	8.79	0.60	11.32	10.98	9.63	
MnO	0.62	0.13	0.55	0.07	0.56	0.03	0.53	0.12	0.54	0.06	0.48	0.44	0.51	
MgO	26.97	0.08	30.31	0.08	27.98	1.47	23.98	1.55	28.93	2.70	26.52	22.88	26.70	
CaO	2.70	0.17	1.75	0.16	2.10	0.69	4.30	1.81	1.94	3.08	2.98	5.58	2.31	
Na$_2$O	0.16	0.01	0.06	0.01	0.21	0.22	0.47	0.02	0.22	0.15	0.26	0.49	0.31	
K$_2$O	0.01	0.01	0.00	0.00	0.01	0.02	0.02	0.02	0.00	0.01	0.02	0.03	0.03	
Total	100.89		99.64		99.10		100.35		99.50		101.25	101.15	100.28	
En [a]	74.49		82.46		78.66		71.13		81.31		75.17	68.71	78.39	
Fs	20.14		14.12		17.07		19.66		14.71		18.77	19.25	16.72	
Wo	5.37		3.42		4.27		9.21		3.98		6.06	12.04	4.88	
Mg# [b]	79.53		86.14		82.95		79.12		85.44		80.68	78.79	83.17	

for notes see Table 2.5

Table 2.7. Experimental plagioclase compositions (MnO-Mn$_3$O$_4$ buffer)

	B1												
Experiment:	63		44		43		42		61		41		40	
T(°C):	1150		1100		1100		1100		1100		1050		1050	
wt% H O in melt:	1.01		3.13		2.45		1.79		1.72		4.73		4.84	
aH$_2$O:	0.1		0.61		0.43		0.27		0.25		1		1	
n:	4		5		4		6		3		3		2	
wt%													
SiO	49.37	0.98	46.42	0.56	49.29	1.50	49.67	0.56	49.95	0.08	46.39	0.04	48.06	0.02
TiO	0.10	0.02	0.12	0.06	0.06	0.02	0.08	0.05	0.17	0.06	0.06	0.03	0.19	0.05
Al O	30.90	0.50	31.47	1.07	30.63	0.24	29.93	0.81	29.87	0.20	33.55	0.15	30.53	0.77
FeO*	1.39	0.19	1.85	0.52	1.36	0.27	1.56	0.02	1.34	0.11	1.18	0.06	2.07	0.30
MnO	0.02	0.02	0.01	0.01	0.05	0.03	0.04	0.03	0.01	0.01	0.04	0.05	0.06	0.02
MgO	0.80	0.20	0.82	0.50	0.41	0.16	0.45	0.19	0.43	0.02	0.18	0.03	0.76	0.21
CaO	16.12	0.67	17.05	0.41	15.32	0.79	14.94	0.43	15.02	0.07	18.24	0.33	16.36	0.32
Na$_2$O	2.39	0.36	1.63	0.08	2.72	0.54	2.87	0.27	2.70	0.02	1.41	0.04	1.81	0.04
K$_2$O	0.02	0.00	0.02	0.01	0.02	0.01	0.03	0.01	0.02	0.01	0.01	0.00	0.04	0.02
Total	101.12		99.39		99.85		99.56		99.48		101.04		99.88	
An	78.7		85.2		75.6		74.1		75.4		87.7		83.1	
Kd Plag-Melt/Ca-Na [a]	1.35		2.26		1.33		1.52		1.67		2.58		2.60	

	B1												
Experiment:	39		38		37		36		35		34		49	
T(°C):	1050		1050		1000		1000		1000		1000		950	
wt% H$_2$O in melt:	3.63		2.34		5.09		5.08		5.21		5.19		5.19	
aH O:	0.70		0.38		1		1		1		1		1	
n:	3		2		3		3		3		2		4	
wt%													
SiO$_2$	49.52	0.43	50.70	0.87	46.33	0.02	49.12	0.30	51.05	0.44	51.55	0.52	49.84	0.19
TiO	0.15	0.04	0.11	0.02	0.00	0.03	0.24	0.12	0.13	0.11	0.13	0.06	0.05	0.04
Al O	29.58	0.84	30.01	0.34	32.90	0.15	29.43	1.35	29.09	1.60	29.61	0.42	31.36	0.64
FeO*	1.58	0.13	1.30	0.18	1.25	0.04	1.93	0.31	1.51	0.49	1.30	0.17	1.32	0.10
MnO	0.00	0.00	0.01	0.01	0.04	0.02	0.02	0.01	0.02	0.03	0.04	0.05	0.02	0.01
MgO	0.56	0.14	0.45	0.12	0.19	0.04	1.00	0.45	0.72	0.64	0.50	0.27	0.38	0.15
CaO	14.32	0.64	14.25	0.11	17.41	0.09	15.19	0.57	14.33	0.14	13.67	0.02	15.97	0.23
Na O	3.00	0.10	3.14	0.09	1.68	0.11	2.10	0.10	3.01	0.30	3.24	0.10	2.36	0.18
K$_2$O	0.04	0.01	0.04	0.00	0.04	0.03	0.03	0.00	0.03	0.01	0.03	0.00	0.02	0.01
Total	98.76		100.00		99.83		99.06		99.90		100.08		101.33	
An	72.4		71.3		84.9		79.8		72.3		69.9		78.8	
Kd Plag-Melt/Ca-Na [a]	1.70		1.79		4.43		3.46		2.70		2.93		4.69	

[a] partition coefficient describing the distribution of calcium and sodium between coexisting plagioclase and melt defined as (XPlag-Ca/XPlag-Na) / (XCa-Melt/XNa-Melt)

Table 2.7. continued

	B1						B2							
Experiment:	48		47		46		92		93		96		98	
T(°C):	950		950		950		1100		1100		1050		1050	
wt% H O in melt:	*5.25*		*5.24*		*5.24*		1.84		1.45		2.48		2.22	
a H$_2$O:	1		1		1		0.28		0.19		0.38		0.32	
n:	2		2		3		2		2		3		3	
wt%														
SiO	51.57	0.38	52.31	0.16	53.39	0.17	52.75	0.93	53.79	0.29	53.66	0.38	54.17	0.30
TiO	0.22	0.06	0.22	0.04	0.14	0.08	0.11	0.02	0.24	0.20	0.42	0.10	0.10	0.12
Al O	27.59	1.13	28.51	0.02	28.31	0.51	28.49	0.28	27.04	1.13	24.51	0.92	24.44	1.83
FeO*	1.76	0.17	1.20	0.02	1.30	0.11	1.43	0.09	1.70	0.55	2.01	0.69	2.60	0.59
MnO	0.03	0.03	0.00	0.00	0.01	0.00	0.03	0.03	0.01	0.02	0.03	0.03	0.07	0.02
MgO	1.78	0.55	1.23	0.03	0.30	0.05	0.28	0.06	0.50	0.40	1.65	0.51	1.83	0.92
CaO	14.65	0.42	13.35	0.06	13.01	0.37	12.87	0.35	11.80	0.32	11.57	0.77	11.22	0.69
Na O	2.51	0.07	3.53	0.03	3.71	0.11	4.05	0.11	4.62	0.06	4.05	0.37	4.40	0.13
K O	0.04	0.01	0.05	0.03	0.05	0.02	0.04	0.03	0.05	0.01	0.08	0.04	0.10	0.02
Total	100.16		100.41		100.22		100.04		99.75		97.99		98.93	
An	76.2		67.4		65.8		63.5		58.3		60.9		58.1	
Kd Plag-Melt/Ca-Na [a]	4.50		3.58		3.54		1.27		0.99		1.50		1.53	

	B2													
Experiment:	100		101		102		103		104		105	106		111
T(°C):	1000		1000		1000		950		950		950	950		950
wt% H O in melt:	*5.18*		*5.26*		4.23		*5.19*		*5.14*		*5.29*	*5.20*		*5.18*
a H$_2$O:	1		1		0.78		1		1		1	1		1
n:	3		2		3		2		4		1	3		1
wt%														
SiO	53.45	0.71	54.60	1.76	54.34	0.35	49.54	0.90	56.26	3.24	54.25	55.99	0.89	55.80
TiO	0.29	0.09	0.21	0.02	0.43	0.34	0.15	0.03	0.29	0.47	0.80	0.21	0.03	0.33
Al$_2$O$_3$	26.24	2.07	26.19	0.95	25.19	1.08	29.56	0.62	24.44	0.51	25.88	24.77	0.91	24.53
FeO*	1.84	0.46	2.33	0.38	2.25	0.96	2.87	0.07	1.85	0.89	3.28	0.84	0.45	2.16
MnO	0.01	0.01	0.02	0.02	0.02	0.02	0.03	0.03	0.06	0.13	0.02	0.01	0.00	0.01
MgO	0.98	0.60	0.48	0.22	1.25	1.10	0.47	0.04	1.03	0.09	0.93	0.75	0.22	2.31
CaO	12.08	0.80	10.90	0.46	10.70	0.25	13.38	0.66	9.78	0.74	10.44	9.85	0.83	11.28
Na$_2$O	3.71	0.06	4.44	0.35	4.56	0.07	3.08	0.32	3.11	0.12	4.58	4.61	0.22	3.39
K$_2$O	0.08	0.02	0.09	0.06	0.10	0.01	0.04	0.01	0.13	0.07	0.10	0.12	0.05	0.09
Total	98.68		99.25		98.84		99.12		96.95		100.29	97.15	3.60	99.89
An	64.0		57.3		56.1		70.4		62.9		55.4	53.7		64.4
Kd Plag-Melt/Ca-Na [a]	2.06		2.12		2.28		2.80		2.52		2.07	2.90		2.48

Table 2.8. Experimental amphibole compositions (MnO-Mn_3O_4 buffer)

	B1										B2	
Experiment:	37		49		48		47		46		103	
T(°C):	1000		950		950		950		950		950	
wt% H_2O in melt:	5.09		5.19		5.25		5.24		5.24		5.19	
$a\,H_2O$:	1		1		1		1		1		1	
n:	3		6		3		2		3		4	
wt%												
SiO_2	42.66	0.29	44.71	0.37	45.08	0.82	44.05	0.24	44.02	0.51	43.61	1.43
TiO_2	1.77	0.03	1.65	0.12	1.92	0.41	2.09	0.34	2.12	0.23	2.13	0.17
Al_2O_3	12.48	0.28	11.60	0.26	11.85	0.69	12.56	0.55	12.39	0.37	11.95	0.52
FeO*	8.21	0.20	9.00	0.48	9.19	0.58	8.96	0.50	9.04	0.21	9.15	0.56
MnO	0.13	0.07	0.17	0.07	0.19	0.02	0.15	0.09	0.17	0.02	0.24	0.06
MgO	17.71	0.06	17.15	0.10	16.14	0.74	15.33	0.31	15.41	0.47	16.17	0.56
CaO	11.72	0.21	11.65	0.21	11.70	0.05	11.62	0.48	11.70	0.31	11.70	0.60
Na_2O	2.44	0.04	2.24	0.06	2.33	0.06	2.42	0.12	2.37	0.11	2.33	0.08
K_2O	0.04	0.02	0.05	0.01	0.06	0.01	0.07	0.02	0.06	0.03	0.06	0.02
Total	97.15		98.23		98.47		97.23		97.28		97.34	
Structural formulae												
Si	6.06		6.27		6.34		6.30		6.30		6.21	
AlVI	1.94		1.73		1.66		1.70		1.70		1.79	
M1-3 site												
AlVI	0.16		0.18		0.31		0.42		0.38		0.22	
Ti	0.19		0.17		0.20		0.22		0.23		0.23	
Fe^{3+}	0.98		1.05		0.77		0.59		0.61		0.88	
Mg	3.68		3.58		3.38		3.27		3.29		3.43	
Fe^{2+}	0.00		0.00		0.31		0.48		0.47		0.21	
M4 site												
Ca	1.78		1.75		1.76		1.78		1.79		1.79	
Na	0.13		0.23		0.24		0.22		0.21		0.21	
A site												
Na	0.54		0.37		0.40		0.45		0.45		0.43	
Mg#[a]	1.00		1.00		0.92		0.87		0.87		0.94	
	magnesiohastingsite[b]		tschermakite		tschermakite		tschermakite		tschermakite		tschermakite	

[a] mg number for amphibole defined as XMg/(XMg+XFe^{2+}) x 100
[b] nomenclature of amphiboles after Leake et al. (1997)

Table 2.9. Experimental magnetite compositions (MnO-Mn O buffer)

	B1													
Experiment:	41		40		39		38		37		36		35	
T(°C):	1050		1050		1050		1050		1000		1000		1000	
wt% H_2O in melt:	*4.73*		*4.84*		3.63		2.34		*5.09*		*5.08*		*5.21*	
aH O:	1		1		0.70		0.38		1		1		1	
n:	2		2		2		3		2		2		1	
wt%														
SiO	0.49	0.20	0.21	0.05	0.16	0.02	0.14	0.03	0.25	0.16	0.22	0.08	0.20	
TiO	2.47	0.02	2.45	0.70	3.67	0.75	4.94	0.15	2.49	0.06	3.27	0.07	4.35	
Al_2O_3	7.20	0.74	8.48	1.16	6.48	0.41	6.72	0.52	7.13	0.04	6.06	0.07	5.58	
Fe O	57.56		56.33		56.79		52.09		58.66		57.12		54.98	
FeO	22.19	0.73	22.41	1.47	24.51	2.57	25.51	2.01	21.51	0.97	22.97	0.44	24.94	
MnO	0.38	0.06	0.30	0.02	0.29	0.03	0.30	0.07	0.38	0.04	0.38	0.02	0.31	
MgO	7.49	0.20	7.15	0.34	6.56	0.31	6.04	0.06	7.84	0.09	6.96	0.02	6.31	
CaO	0.45	0.11	0.37	0.03	0.36	0.04	0.34	0.05	0.40	0.13	0.41	0.00	0.34	
Na_2O	0.02	0.02	0.04	0.02	0.02	0.04	0.06	0.05	0.01	0.01	0.01	0.01	0.00	
K O	0.00	0.01	0.01	0.01	0.00	0.00	0.00	0.00	0.01	0.01	0.01	0.01	0.00	
Total	98.22		97.75		98.83		96.15		98.69		97.42		97.00	
XUsp[a]	7.26		7.49		10.99		15.47		7.20		9.66		13.18	

	B1									B2				
Experiment:	34		49		48		47		46		90		91	
T(°C):	1000		950		950		950		950		1100		1100	
wt% H O in melt:	*5.19*		*5.19*		*5.25*		*5.24*		*5.24*		*4.63*		2.10	
aH O:	1		1		1		1		1		1		0.34	
n:	2		4		3		2		1		3		2	
wt%														
SiO	0.14	0.10	0.28	0.03	0.89	0.58	0.15	0.21	0.17		0.13	0.02	0.22	0.04
TiO_2	4.94	0.03	2.17	0.12	2.84	1.47	3.80	10.34	4.58		1.54	0.03	2.83	0.08
Al_2O_3	5.49	0.20	4.94	0.01	4.99	0.76	5.82	3.18	5.82		4.85	0.01	7.35	0.05
Fe_2O_3	53.91		60.52		57.12		55.53		53.85		63.02		56.95	
FeO	25.09	0.45	23.25	0.67	23.86	4.15	23.94	2.87	25.00		19.84	0.67	22.97	0.42
MnO	0.32	0.02	0.38	0.05	0.36	0.00	0.36	0.09	0.39		0.35	0.01	0.25	0.06
MgO	6.30	0.14	6.22	0.05	6.23	0.29	5.95	1.83	6.09		7.91	0.07	7.01	0.12
CaO	0.30	0.11	0.37	0.05	0.55	0.25	0.32	0.21	0.34		0.36	0.05	0.37	0.01
Na O	0.04	0.00	0.01	0.01	0.07	0.07	0.16	0.05	0.04		0.01	0.01	0.03	0.01
K O	0.02	0.01	0.00	0.00	0.01	0.00	0.01	0.00	0.01		0.01	0.02	0.01	0.01
Total	96.55		98.14		96.91		96.04		96.29		98.02		97.99	
XUsp[a]	15.00		6.07		8.42		11.53		14.01		4.08		8.62	

[a] ulvöspinell content (XUsp x 100) content of magnetite calculated after Stormer (1983)

Table 2.9. continued

	B2													
Experiment:	92		93		94		95		96		98		99	
T (°C):	1100		1100		1050		1050		1050		1050		1000	
wt% H O in melt:	1.84		1.45		*4.80*		2.65		2.48		2.22		*5.06*	
$a H_2O$:	0.28		0.19		1		0.43		0.38		0.32		1	
n:	2		3		2		3		2		3		2	
wt%														
SiO_2	0.96	0.75	0.27	0.07	0.18	0.01	0.73	0.35	0.43	0.01	0.12	0.01	0.22	0.04
TiO_2	4.46	0.08	5.49	0.44	1.96	0.04	3.93	0.21	5.85	0.00	6.57	0.16	2.44	0.04
Al_2O_3	6.59	0.11	6.21	0.27	4.85	0.14	5.88	0.32	4.34	0.17	3.87	0.03	5.91	0.02
Fe_2O_3	52.36		51.67		62.55		56.10		53.87		52.37		59.71	
FeO	26.23	0.37	27.25	0.90	19.27	0.14	24.01	0.82	27.36	0.14	28.73	0.42	19.63	0.01
MnO	0.24	0.00	0.28	0.04	0.41	0.02	0.43	0.05	0.46	0.04	0.46	0.01	0.56	0.11
MgO	6.19	0.13	5.59	0.08	8.53	0.20	7.08	0.04	5.67	0.05	4.89	0.03	8.46	0.06
CaO	0.76	0.37	0.40	0.05	0.32	0.07	0.55	0.18	0.45	0.07	0.30	0.04	0.43	0.02
Na_2O	0.00	0.00	0.01	0.01	0.02	0.03	0.06	0.07	0.05	0.07	0.01	0.00	0.02	0.01
K_2O	0.00	0.00	0.02	0.01	0.02	0.01	0.02	0.01	0.01	0.01	0.01	0.00	0.01	0.01
Total	97.80		97.20		98.10		98.80		98.48		97.34		97.38	
XUsp[a]	14.17		17.10		5.24		11.61		17.18		19.41		6.64	

	B2														
Experiment:	100		101		102	103		104		105		106	111		
T (°C):	1000		1000		1000	950		950		950		950	950		
wt% H_2O in melt:	*5.18*		*5.26*		4.23	*5.19*		*5.14*		*5.29*		*5.20*	*5.18*		
$a H_2O$:	1		1		0.78	1		1		1		1	1		
n:	2		3		1	2		2		3		1	2		
wt%															
SiO_2	0.21	0.11	0.18	0.12	0.14	0.39	0.21	2.38	2.61	0.21	0.11	0.97	0.87	0.32	
TiO_2	3.44	0.07	3.72	0.09	3.97	2.20	0.03	2.54	0.06	2.74	0.08	3.21	2.87	0.07	
Al_2O_3	4.50	0.04	3.56	0.02	3.37	4.56	0.09	4.17	1.07	3.13	0.55	3.93	4.39	0.25	
Fe_2O_3	58.97		58.85		57.36	59.74		55.91		59.66		56.74	58.11		
FeO	24.06	0.41	26.16	1.28	26.90	22.71	1.28	27.25	3.11	26.07	0.12	28.54	24.93	1.25	
MnO	0.52	0.04	0.53	0.05	0.40	0.72	0.04	0.55	0.02	0.56	0.11	0.39	0.84	0.06	
MgO	6.30	0.06	4.94	0.08	4.29	6.14	0.05	5.35	0.05	4.05	0.09	3.33	5.22	0.02	
CaO	0.35	0.10	0.36	0.05	0.36	0.29	0.38	0.73	0.47	0.38	0.46	0.95	0.72	0.16	
Na_2O	0.02	0.02	0.03	0.02	0.04	0.03	0.00	0.01	0.16	0.02	0.04	0.04	0.05	0.03	
K_2O	0.01	0.00	0.00	0.00	0.01	0.02	0.01	0.00	0.01	0.00	0.00	0.01	0.04	0.00	
Total	98.38		98.34		96.84	96.79		98.89		96.83		98.13	98.05		
XUsp[a]	9.64		10.41		11.54	5.66		7.38		7.51		9.53	7.62		

Table 2.10. Experimental ilmenite compositions (MnO-Mn$_3$O$_4$ buffer)

	B1		B2									
Experiment:	47	46	96	98	100	101	102	103	104	105	106	111
T(°C):	950	950	1050	1050	1000	1000	1000	950	950	950	950	950
wt% H$_2$O in melt:	*5.24*	*5.24*	2.48	2.22	*5.18*	*5.26*	4.23	*5.19*	*5.14*	*5.29*	*5.20*	*5.18*
aH$_2$O:	1	1	0.38	0.32	1	1	0.78	1	1	1	1	1
n:	1	1	1	1	2	1	2	2	2	2	2	2
wt%												
SiO$_2$	1.18	1.16	0.69	0.48	0.18	0.96	0.13	0.14	0.17	0.42	0.34	0.86
TiO$_2$	19.49	20.32	22.51	24.90	18.63	19.41	20.92	14.72	17.31	17.81	18.59	18.62
Al$_2$O$_3$	1.46	1.33	1.32	1.08	1.26	1.32	1.59	1.27	1.10	1.82	2.31	1.14
Fe$_2$O$_3$	58.89	57.83	53.87	50.83	61.89	58.50	61.01	69.18	63.01	65.51	62.40	61.92
FeO	11.56	13.09	13.50	16.10	10.15	12.49	12.11	8.29	10.02	8.40	9.55	10.61
MnO	0.22	0.23	0.25	0.22	0.25	0.18	0.20	0.14	0.23	0.17	0.17	0.35
MgO	3.41	2.99	3.67	3.33	3.27	2.87	2.79	2.44	2.79	3.06	2.78	3.25
CaO	0.62	0.55	0.48	0.52	0.43	0.54	0.73	0.30	0.39	1.42	1.22	0.69
Na$_2$O	0.06	0.06	0.03	0.01	0.04	0.02	0.15	0.03	0.01	0.14	0.19	0.02
K$_2$O	0.00	0.01	0.00	0.00	0.01	0.02	0.02	0.03	0.00	0.01	0.00	0.02
Total	96.89	97.56	96.32	97.47	96.09	96.30	99.65	96.54	95.03	98.76	97.55	97.48
XIlm[a]	31.49	34.24	37.21	42.72	29.51	33.07	35.61	23.78	28.32	29.07	32.82	29.03

[a] ilmenite (XIlm x 100) of content rhombohedral oxide calculated after Stormer (1983)

5. Tables

Table 2.11. Experimental glass compositions (MnO-Mn$_3$O$_4$ buffer)

	B1															
Experiment:	66		65		64		63		45		44		43		42	
T(°C):	1150		1150		1150		1150		1100		1100		1100		1100	
wt% H$_2$O in melt:	4.55		2.56		1.54		1.01		4.57		3.13		2.45		1.79	
aH$_2$O:	1		0.47		0.21		0.10		1		0.61		0.43		0.27	
n:	6		3		3		6		4		6		4		10	
wt% [a]																
SiO$_2$	49.67	0.20	49.88	1.12	50.19	0.19	50.34	0.45	50.15	0.74	50.16	0.47	50.96	0.53	51.38	0.57
TiO$_2$	0.85	0.09	0.77	0.12	0.86	0.10	0.93	0.16	0.82	0.06	0.91	0.14	1.25	0.10	1.46	0.11
Al$_2$O$_3$	16.01	0.21	16.29	0.30	16.72	0.20	16.58	0.18	16.29	0.35	17.42	0.40	17.12	0.80	15.97	0.57
FeO*	8.59	0.09	9.06	0.75	8.51	0.19	8.79	0.28	8.69	0.29	9.47	0.34	10.19	0.73	10.98	0.25
MnO	0.14	0.08	0.10	0.09	0.17	0.03	0.15	0.17	0.17	0.05	0.21	0.02	0.14	0.13	0.19	0.15
MgO	9.83	0.10	9.21	0.08	8.41	0.07	8.00	0.19	8.97	0.18	7.12	0.14	6.12	0.17	6.16	0.29
CaO	12.39	0.21	12.41	0.12	12.77	0.16	12.55	0.17	12.47	0.40	11.95	0.20	11.22	0.29	10.50	0.30
Na$_2$O	2.33	0.19	2.20	0.24	2.27	0.05	2.51	0.25	2.26	0.28	2.58	0.32	2.64	0.16	3.06	0.24
K$_2$O	0.10	0.08	0.03	0.01	0.07	0.05	0.11	0.07	0.11	0.05	0.09	0.06	0.14	0.02	0.12	0.07
P$_2$O$_5$	0.09	0.09	0.04	0.02	0.03	0.03	0.05	0.09	0.08	0.09	0.09	0.08	0.22	0.14	0.18	0.12
Total[b]	94.80	0.76	97.88	0.89	98.89	0.62	98.78	0.75	94.98	0.76	96.79	0.98	97.43	1.11	97.54	0.96
Mg#[c]	82.66	1.20	78.15	1.48	75.31	0.82	71.59	2.15	81.31	2.35	73.73	1.86	67.39	2.33	64.00	3.66

	B1															
Experiment:	62		61		41		40		39		38		37		36	
T(°C):	1100		1100		1050		1050		1050		1050		1000		1000	
wt% H$_2$O in melt:	4.56		1.72		4.73		4.84		3.63		2.34		5.09		5.08	
aH$_2$O:	1		0.25		1		1		0.70		0.38		1		1	
n:	3		3		2		6		5		2		3		4	
wt% [a]																
SiO$_2$	49.79	0.04	51.35	0.65	51.13	0.33	53.43	0.83	53.64	1.53	54.54	1.21	56.17	0.83	57.57	0.55
TiO$_2$	0.82	0.06	1.34	0.03	0.98	0.05	0.95	0.13	1.24	0.11	1.32	0.19	1.05	0.11	1.07	0.01
Al$_2$O$_3$	16.07	0.21	16.28	0.52	18.17	0.10	18.40	1.15	17.82	1.51	18.17	0.70	18.79	0.33	18.04	0.41
FeO*	8.84	0.04	10.68	0.14	8.62	0.46	8.77	0.66	9.34	0.42	8.82	0.76	6.50	0.27	6.82	0.42
MnO	0.19	0.02	0.16	0.07	0.24	0.14	0.20	0.14	0.21	0.05	0.23	0.08	0.13	0.14	0.12	0.04
MgO	9.10	0.07	6.20	0.22	6.03	0.04	4.63	0.17	4.24	0.19	4.27	0.39	4.47	0.07	3.88	0.28
CaO	12.79	0.17	10.54	0.37	12.19	0.08	10.37	0.65	9.73	0.96	8.79	0.83	8.76	0.29	8.05	0.14
Na$_2$O	2.11	0.06	3.16	0.32	2.43	0.18	2.99	0.25	3.47	0.28	3.46	0.89	3.74	0.67	3.84	0.23
K$_2$O	0.12	0.03	0.13	0.08	0.07	0.01	0.11	0.05	0.23	0.06	0.24	0.06	0.14	0.09	0.29	0.04
P$_2$O$_5$	0.17	0.07	0.15	0.09	0.15	0.09	0.15	0.08	0.08	0.06	0.15	0.11	0.24	0.02	0.33	0.17
Total[b]	95.15	0.70	97.92	0.61	94.16	0.98	94.89	0.45	96.24	1.11	96.95	1.28	94.53	1.50	94.74	1.95
Mg#[c]	81.31	0.85	64.51	2.80	74.76	0.79	68.66	3.32	63.70	3.82	62.05	6.84	74.69	1.81	70.84	6.22

	B1									
Experiment:	35		34		49		48		47[d]	46[d]
T(°C):	1000		1000		950		950		950	950
wt% H$_2$O in melt:	5.21		5.19		5.19		5.25		5.24	5.24
aH$_2$O:	1		1		1		1		1	1
n:	4		3		4		3		-	-
wt% [a]										
SiO$_2$	57.53	0.59	58.68	0.66	63.16	0.96	63.49	1.73	63.73	64.16
TiO$_2$	1.00	0.12	1.35	0.13	0.70	0.06	0.86	0.10	1.00	1.15
Al$_2$O$_3$	19.24	1.43	18.12	0.58	16.75	0.50	17.21	1.12	16.43	15.86
FeO*	6.43	0.68	6.36	0.06	5.31	0.38	5.24	0.21	5.75	5.70
MnO	0.16	0.12	0.27	0.06	0.12	0.13	0.02	0.30	0.02	0.22
MgO	2.99	0.27	2.70	0.22	2.52	0.30	1.82	0.34	1.35	1.29
CaO	7.74	0.84	7.09	0.35	6.43	0.33	6.20	0.13	5.78	5.49
Na$_2$O	4.39	0.29	4.91	0.42	4.45	0.66	4.78	0.67	5.48	5.54
K$_2$O	0.26	0.07	0.24	0.13	0.29	0.10	0.23	0.04	0.34	0.39
P$_2$O$_5$	0.26	0.10	0.27	0.07	0.25	0.25	0.15	0.03	0.15	0.21
Total[b]	93.85	1.13	93.13	1.65	92.94	1.49	93.05	1.28	-	-
Mg#[c]	66.63	7.33	64.96	6.42	67.83	9.69	60.82	13.17	51.62	50.76

[a] oxide concentrations from microprobe are normalized to 100 wt% with all Fe as FeO* (total iron)

[b] Total from microprobe

[c] mg number for glass defined as XMgO / (XMgO+XFeO) x 100 and Fe$_2$O$_3$ and FeO content calculated after Kress and Carmichael (1991)

[d] melt composition is calculated (see text for detailed comments)

Table 2.11. continued

	B2														
Experiment:	86		87		88		89		90		91		92		93	
T(°C):	1150		1150		1150		1150		1100		1100		1100		1100	
wt% H_2O in melt:	4.58		2.05		1.25		0.75		4.63		2.10		1.84		1.45	
aH_2O:	1		0.34		0.15		0.06		1		0.34		0.28		0.19	
n:	10		3		4		8		2		4		4		3	
wt% [a]															
SiO_2	51.17	0.23	50.91	0.61	51.43	0.27	51.71	0.29	52.24	0.74	52.00	0.62	52.85	0.07	53.08	0.30
TiO_2	1.43	0.06	1.51	0.05	1.49	0.13	1.41	0.08	1.41	0.03	1.61	0.02	1.70	0.08	2.02	0.11
Al_2O_3	15.93	0.16	15.68	0.24	15.80	0.29	15.90	0.24	16.14	0.44	15.80	0.40	15.35	0.32	14.74	0.26
FeO*	10.72	0.26	11.46	0.47	10.47	0.43	10.45	0.72	9.22	0.50	10.26	0.54	10.73	0.21	11.94	0.21
MnO	0.21	0.07	0.31	0.13	0.29	0.20	0.23	0.08	0.31	0.13	0.34	0.07	0.33	0.12	0.28	0.13
MgO	6.49	0.07	6.40	0.18	6.38	0.21	6.39	0.12	6.19	0.30	6.22	0.28	5.91	0.14	5.32	0.24
CaO	10.57	0.13	10.39	0.13	10.60	0.15	10.54	0.17	11.07	0.04	10.36	0.44	9.13	0.18	8.85	0.24
Na_2O	3.13	0.11	3.15	0.13	3.36	0.16	2.96	0.29	3.12	0.12	3.21	0.26	3.66	0.13	3.43	0.28
K_2O	0.15	0.04	0.06	0.02	0.09	0.02	0.14	0.06	0.16	0.04	0.09	0.03	0.18	0.05	0.22	0.02
P_2O_5	0.19	0.07	0.12	0.03	0.08	0.04	0.26	0.14	0.13	0.06	0.12	0.04	0.15	0.03	0.14	0.01
Total[b]	94.89	0.38	97.85	0.75	98.09	0.87	99.20	0.46	94.19	0.60	97.85	0.50	98.04	1.03	97.84	0.31
Mg#[c]	71.11	1.02	64.49	2.27	63.78	2.50	60.91	1.34	73.89	4.57	66.62	2.44	63.71	1.86	56.86	2.99

	B2														
Experiment:	94		95		96		98		99		100		101		102	
T(°C):	1050		1050		1050		1050		1000		1000		1000		1000	
wt% H_2O in melt:	4.80		2.65		2.48		2.22		5.06		5.18		5.26		4.23	
aH_2O:	1		0.43		0.38		0.32		1		1		1		0.78	
n:	3		3		5		4		3		3		4		5	
wt% [a]															
SiO_2	54.32	0.64	56.85	0.73	59.03	0.71	59.73	1.23	56.70	0.20	60.57	0.91	62.17	0.69	63.13	0.96
TiO_2	1.49	0.14	1.38	0.13	1.19	0.26	0.90	0.23	1.42	0.08	1.12	0.04	1.23	0.04	1.05	0.08
Al_2O_3	16.36	0.52	17.85	2.19	17.96	2.23	17.92	1.08	18.42	0.64	17.96	0.57	17.94	1.02	16.18	0.56
FeO*	7.46	0.46	5.99	0.41	5.74	0.74	5.56	0.53	5.82	0.89	5.94	0.22	5.32	0.56	5.43	0.42
MnO	0.15	0.06	0.30	0.12	0.23	0.22	0.09	0.02	0.14	0.05	0.39	0.08	0.25	0.29	0.08	0.06
MgO	5.88	0.15	4.17	0.36	3.70	0.32	3.19	0.31	4.21	0.07	2.30	0.27	1.93	0.04	1.70	0.25
CaO	10.74	0.21	9.16	0.01	7.72	0.77	7.58	0.42	9.30	0.15	6.84	0.49	5.67	0.19	5.59	0.55
Na_2O	3.31	0.20	3.94	0.03	4.05	0.11	4.54	0.57	3.67	0.41	4.32	0.53	4.89	0.68	5.42	0.22
K_2O	0.17	0.04	0.28	0.16	0.27	0.11	0.34	0.21	0.24	0.06	0.36	0.05	0.32	0.08	0.46	0.01
P_2O_5	0.13	0.06	0.09	0.04	0.09	0.09	0.15	0.00	0.08	0.03	0.21	0.06	0.28	0.01	0.95	0.14
Total[b]	93.81	0.90	97.25	0.75	97.18	1.08	97.60	1.49	93.71	0.34	95.28	0.77	94.41	1.03	95.39	1.21
Mg#[c]	77.43	2.58	71.59	7.78	69.08	7.54	66.15	7.79	75.99	1.78	62.38	8.62	60.85	1.59	56.71	9.77

	B2									
Experiment:	103		104		105		106		111	
T(°C):	950		950		950		950		950	
wt% H_2O in melt:	5.19		5.14		5.29		5.20		5.18	
aH_2O:	1		1		1		1		1	
n:	3		5		2		3		4	
wt% [a]										
SiO_2	64.87	0.13	65.88	0.85	65.98	1.18	70.02	1.13	65.36	1.21
TiO_2	0.82	0.23	0.84	0.09	0.78	0.09	0.65	0.09	0.91	0.12
Al_2O_3	17.18	0.25	15.94	0.42	16.79	0.06	13.08	1.05	16.32	0.94
FeO*	3.92	0.26	4.11	0.16	3.70	0.25	3.70	0.02	4.22	0.65
MnO	0.20	0.00	0.07	0.07	0.13	0.13	0.05	0.06	0.18	0.05
MgO	2.61	0.10	1.81	0.26	1.50	0.09	1.21	0.14	1.73	0.23
CaO	6.00	0.14	5.85	0.25	5.42	0.10	4.13	0.36	6.03	0.45
Na_2O	3.87	0.08	4.67	0.26	4.94	0.20	5.60	0.92	4.49	0.64
K_2O	0.24	0.04	0.30	0.02	0.34	0.11	0.82	0.02	0.33	0.08
P_2O_5	0.29	0.00	0.52	0.06	0.42	0.07	0.75	0.11	0.43	0.12
Total[b]	93.19	1.66	93.62	1.67	93.99	0.75	93.59	1.42	96.46	1.42
Mg#[c]	74.34	3.71	66.45	11.67	64.52	4.92	60.48	8.27	64.74	10.34

5. Tables

Table 3.2. Experimental olivine compositions (QFM buffer)

B1 QFM buffer

	129	128	127	134	132	133	131	142	141
Experiment:	129	128	127	134	132	133	131	142	141
T (°C):	1150	1150	1150	1100	1100	1100	1100	1050	1050
wt% H O in melt:	2.08	1.02	0.38	*4.53*	2.37	1.49	0.85	*4.84*	3.33
aH_2O:	0.33	0.1	0.02	1	0.4	0.2	0.07	1	0.64
ΔQFM:	-0.75	-1.85	-3.41	+0.09	-0.80	-1.31	-2.26	-0.01	-0.39
n:	4	3	5	3	4	9	5	8	8
wt%									
SiO_2	41.37 0.61	41.20 0.08	40.42 0.21	39.92 0.09	39.78 0.17	40.14 0.30	39.01 0.10	39.63 0.33	39.47 0.36
TiO_2	0.02 0.02	0.03 0.03	0.02 0.02	0.04 0.02	0.04 0.01	0.02 0.01	0.03 0.01	0.03 0.02	0.02 0.02
Al_2O_3	0.05 0.05	0.09 0.04	0.12 0.09	0.05 0.07	0.08 0.03	0.11 0.05	0.18 0.18	0.05 0.02	0.06 0.06
FeO	11.28 0.89	11.43 0.17	13.79 0.25	13.48 1.01	14.73 0.66	16.81 1.86	19.71 0.63	17.33 0.58	19.78 0.56
MnO	0.17 0.04	0.20 0.06	0.22 0.06	0.21 0.02	0.26 0.10	0.25 0.09	0.29 0.07	0.24 0.06	0.32 0.05
MgO	47.34 0.95	46.93 0.35	45.92 0.27	45.40 0.95	43.25 0.76	43.10 1.63	39.47 0.64	42.11 0.77	39.43 1.30
CaO	0.34 0.04	0.35 0.01	0.32 0.04	0.37 0.05	0.34 0.04	0.35 0.04	0.33 0.08	0.36 0.04	0.32 0.05
Na O	0.02 0.02	0.01 0.01	0.02 0.02	0.01 0.02	0.03 0.02	0.02 0.02	0.02 0.02	0.01 0.01	0.09 0.23
K_2O	0.00 0.00	0.00 0.00	0.00 0.00	0.01 0.01	0.00 0.00	0.01 0.01	0.01 0.01	0.01 0.01	0.01 0.01
Total	100.58	100.23	100.83	99.51	98.52	100.81	99.06	99.77	99.50
XFo [a]	88.21	87.98	85.58	85.72	83.96	82.05	78.11	81.25	78.04
Kd Ol-Melt/Mg-Fe [b]	0.301	0.257	0.295	0.360	0.304	0.359	0.327	0.343	0.365

B1 QFM buffer

	140	143	148	147	146	145	153	152	151
Experiment:	140	143	148	147	146	145	153	152	151
T (°C):	1050	1050	1000	1000	1000	1000	950	950	950
wt% H_2O in melt:	2.90	2.04	*5.06*	5.01	5.04	3.52	*5.12*	*5.12*	*5.17*
aH_2O:	0.51	0.32	1	0.99	0.99	0.64	1	1	1
ΔQFM:	-0.54	-0.91	+0.01	+0.02	+0.03	-0.36	+0.09	+0.09	+0.09
n:	4	4	4	6	5	10	3	3	3
wt%									
SiO_2	38.43 0.14	37.86 0.21	38.26 0.31	37.88 0.25	37.52 0.54	38.18 0.47	37.19 0.03	36.80 0.10	37.19 0.38
TiO	0.04 0.02	0.05 0.02	0.03 0.01	0.04 0.02	0.05 0.01	0.06 0.02	0.01 0.01	0.05 0.01	0.06 0.02
Al_2O_3	0.08 0.03	0.10 0.08	0.02 0.01	0.06 0.03	0.29 0.26	0.27 0.31	0.04 0.00	0.10 0.08	0.34 0.36
FeO	23.51 0.28	24.90 1.02	23.60 0.58	25.40 0.38	26.61 0.61	25.73 0.82	30.33 0.30	30.73 0.46	30.44 0.29
MnO	0.34 0.09	0.39 0.04	0.36 0.04	0.40 0.03	0.41 0.05	0.41 0.04	0.39 0.02	0.45 0.05	0.40 0.08
MgO	38.16 0.17	36.51 0.52	38.51 0.22	37.16 1.33	35.64 0.93	34.58 0.76	32.56 0.12	32.14 0.65	32.57 0.91
CaO	0.37 0.03	0.43 0.02	0.35 0.05	0.38 0.04	0.47 0.15	0.43 0.13	0.26 0.03	0.32 0.11	0.27 0.18
Na_2O	0.02 0.04	0.03 0.03	0.02 0.02	0.09 0.15	0.00 0.00	0.03 0.05	0.00 0.01	0.00 0.01	0.01 0.01
K_2O	0.00 0.00	0.01 0.01	0.02 0.01	0.00 0.00	0.00 0.01	0.00 0.00	0.01 0.02	0.01 0.02	0.01 0.01
Total	100.94	100.27	101.16	101.41	101.00	99.70	100.79	100.60	101.28
XFo [a]	74.56	72.55	75.31	73.52	71.08	70.56	65.77	65.56	65.77
Kd Ol-Melt/Mg-Fe [b]	0.290	0.282	0.326	0.351	0.308	0.272	0.315	0.298	0.276

[a] XFo x 100

[b] partition coefficient describing the distribution of iron and magnesium between melt and coexisting olivine defined as
(XOl-FeO/XMelt-FeO) x (XMelt-MgO/XOl-MgO) after Roeder and Emslie (1970)

Table 3.3. Experimental clinopyroxene compositions (QFM buffer)

	B1 QFM buffer														
Experiment:	127		132		133		131		142		141		140		143	
T(°C):	1150		1100		1100		1100		1050		1050		1050		1050	
wt% H O in melt:	0.38		2.37		1.49		0.85		*4.84*		3.33		2.90		2.04	
aH O:	0.02		0.4		0.2		0.07		1		0.64		0.51		0.32	
ΔQFM:	-3.41		-0.80		-1.31		-2.26		-0.01		-0.39		-0.54		-0.91	
n:	5		5		4		3		7		3		5		4	
wt%															
SiO	51.50	1.36	51.27	0.85	52.47	0.81	50.54	0.66	50.97	1.00	49.67	1.86	50.55	0.91	50.37	0.60
TiO	0.51	0.05	0.49	0.02	0.59	0.10	0.67	0.08	0.65	0.12	0.75	0.15	0.74	0.06	0.84	0.02
Al O	4.90	0.88	4.85	0.62	4.88	1.36	4.86	0.46	6.02	1.65	5.50	1.43	4.81	0.91	4.95	1.01
FeO*	6.33	1.33	6.36	0.79	6.94	0.68	8.42	0.46	6.48	0.66	7.77	0.79	8.41	0.99	8.94	0.76
MnO	0.14	0.05	0.18	0.07	0.16	0.02	0.24	0.03	0.12	0.03	0.18	0.07	0.19	0.03	0.23	0.07
MgO	16.31	0.74	14.99	0.41	15.60	0.90	15.22	0.38	15.00	1.58	15.12	0.79	15.46	0.33	14.91	0.85
CaO	20.63	0.53	20.80	0.72	20.49	1.13	19.18	0.42	20.39	0.82	21.05	0.77	19.82	0.73	19.39	0.62
Na_2O	0.33	0.13	0.22	0.03	0.31	0.09	0.33	0.03	0.28	0.15	0.21	0.06	0.29	0.21	0.34	0.08
K O	0.01	0.01	0.01	0.01	0.01	0.02	0.02	0.01	0.02	0.01	0.01	0.01	0.01	0.01	0.01	0.01
Total	100.67		99.16		101.45		99.47		99.93		100.27		100.29		99.97	
En [a]	46.91		44.60		45.46		44.94		44.97		43.57		44.77		43.87	
Fs	10.44		10.91		11.62		14.34		11.10		12.86		13.98		15.14	
Wo	42.65		44.49		42.92		40.72		43.94		43.57		41.25		41.00	
Mg# [b]	0.86		0.81		0.80		0.78		0.81		0.85		0.81		0.77	
Kd Cpx-Melt/Fe-Mg [a]	0.30		0.38		0.41		0.32		0.36		0.24		0.20		0.21	

	B1 QFM buffer													
Experiment:	148		147		146		145		153		152		151	
T(°C):	1000		1000		1000		1000		950		950		950	
wt% H_2O in melt:	*5.06*		5.01		5.04		3.52		*5.12*		*5.12*		*5.17*	
aH O:	1		0.99		0.99		0.64		1		1		1	
ΔQFM:	+0.01		+0.02		+0.03		-0.36		+0.09		+0.09		+0.09	
n:	3		4		10		6		3		3		3	
wt%														
SiO_2	48.90	1.36	50.43	0.39	49.73	0.79	51.01	0.86	51.10	0.29	51.59	0.19	50.38	0.73
TiO_2	1.17	0.42	0.89	0.07	1.23	0.13	1.17	0.15	0.62	0.06	0.70	0.03	1.02	0.11
Al_2O_3	6.52	1.82	4.75	0.31	6.49	1.40	5.67	1.89	3.60	0.49	3.37	0.06	5.27	0.98
FeO*	7.10	0.72	8.25	0.62	9.07	0.60	8.48	0.40	10.60	0.52	10.03	0.51	10.38	0.68
MnO	0.13	0.04	0.25	0.04	0.20	0.05	0.20	0.05	0.29	0.08	0.31	0.06	0.21	0.01
MgO	14.26	1.07	14.92	0.54	13.60	1.22	13.44	1.23	15.49	0.15	15.17	0.16	14.90	0.25
CaO	21.78	0.73	20.21	0.92	18.02	1.60	18.88	1.20	17.84	0.67	19.10	0.62	18.07	1.09
Na O	0.21	0.08	0.25	0.18	0.22	0.21	0.40	0.10	0.13	0.11	0.19	0.12	0.48	0.08
K O	0.00	0.00	0.01	0.01	0.02	0.02	0.03	0.02	0.02	0.01	0.01	0.01	0.02	0.00
Total	100.08		99.97		98.59		99.27		99.68		100.47		100.73	
En [a]	41.98		43.60		42.82		42.15		44.99		43.72		44.05	
Fs	11.94		13.94		16.39		15.28		17.75		16.72		17.57	
Wo	46.08		42.46		40.79		42.57		37.26		39.56		38.38	
Mg# [b]	0.83		0.79		0.73		0.74		0.73		0.74		0.748	
Kd Cpx-Melt/Fe-Mg [a]	0.19		0.25		0.28		0.23		0.22		0.20		0.18	

[a] calculated after Morimoto (1988)

[b] mg number for pyroxene defined as XMg/(XMg+XFe) x 100

[c] partition coefficient describing the distribution of Mg and Fe^{2+} between coexisting clinopyroxene and melt defined as
(XCpx-FeO/XCpx-MgO) x (XMelt-MgO/XMelt-FeO)

5. Tables

Table 3.4. Experimental plagioclase compositions (QFM buffer)

	B1 QFM buffer													
Experiment:	127		132		133		131		141		140		143	
T (°C):	1150		1100		1100		1100		1050		1050		1050	
wt% H_2O in melt:	0.38		2.37		1.49		0.85		*3.33*		*2.90*		2.04	
aH_2O:	0.02		0.4		0.2		0.07		0.64		0.51		0.32	
ΔQFM:	-3.41		-0.80		-1.31		-2.26		-0.39		-0.54		-0.91	
n:	2		5		4		6		3		6		5	
wt%														
SiO_2	50.09	0.51	47.14	0.43	49.78	0.57	51.15	1.04	47.58	0.88	50.10	0.56	50.95	0.43
TiO	0.11	0.02	0.05	0.05	0.12	0.06	0.18	0.10	0.07	0.03	0.33	0.13	0.14	0.07
Al_2O_3	30.07	0.22	32.42	0.31	30.29	1.33	28.44	1.70	32.54	0.47	27.78	2.71	29.69	0.86
FeO*	1.19	0.06	0.95	0.08	1.31	0.33	1.32	0.50	0.97	0.24	2.38	0.78	1.10	0.15
MnO	0.00	0.00	0.01	0.02	0.02	0.02	0.04	0.02	0.04	0.04	0.04	0.04	0.02	0.03
MgO	0.75	0.05	0.44	0.11	1.22	0.69	0.95	0.62	0.41	0.10	1.56	1.77	0.49	0.16
CaO	15.74	0.50	17.48	0.16	16.18	0.17	14.56	0.63	17.14	0.43	14.54	1.10	14.37	0.31
Na O	2.65	0.14	1.64	0.08	2.13	0.19	3.04	0.38	1.73	0.24	2.65	0.34	3.04	0.29
K_2O	0.02	0.01	0.03	0.01	0.03	0.01	0.04	0.02	0.03	0.01	0.04	0.02	0.03	0.02
Total	100.62		100.16		101.08		99.70		100.51		99.42		99.83	
An	76.6		85.4		80.6		72.4		84.4		75.1		72.2	
Kd Plag-Melt/Ca-Na [a]	1.15		2.02		1.73		1.07		2.72		1.96		1.13	

	B1 QFM buffer													
Experiment:	148		147		146		145		153		152		151	
T (°C):	1000		1000		1000		1000		950		950		950	
wt% H_2O in melt:	*5.06*		5.01		5.04		3.52		*5.12*		*5.12*		*5.17*	
aH_2O:	1		0.99		0.99		0.64		1		1		1	
ΔQFM:	+0.01		+0.02		+0.03		-0.36		+0.09		+0.09		+0.09	
n:	4		2		3		5		3		4		2	
wt%														
SiO_2	48.20	0.38	48.57	0.22	50.88	1.15	50.41	0.51	49.21	0.33	50.37	0.58	51.82	0.08
TiO	0.03	0.02	0.14	0.07	0.41	0.23	0.25	0.08	0.14	0.03	0.12	0.05	0.15	0.09
Al_2O_3	32.97	0.47	31.82	0.70	27.37	1.55	28.53	1.06	30.84	0.64	29.68	1.02	29.37	1.19
FeO*	0.70	0.14	0.99	0.15	2.25	0.94	1.73	0.31	1.40	0.08	1.36	0.37	1.34	0.46
MnO	0.03	0.03	0.03	0.04	0.06	0.04	0.04	0.04	0.06	0.04	0.02	0.02	0.06	0.06
MgO	0.15	0.19	0.46	0.04	1.39	0.60	1.09	0.57	0.33	0.30	1.01	0.66	0.51	0.45
CaO	16.17	0.40	15.82	0.36	13.25	0.86	13.61	0.60	15.07	0.26	14.24	0.49	13.19	0.22
Na O	2.30	0.21	2.32	0.01	2.77	0.53	3.09	0.25	2.52	0.05	2.96	0.27	3.79	0.25
K_2O	0.02	0.01	0.03	0.01	0.04	0.02	0.03	0.01	0.03	0.02	0.03	0.01	0.04	0.01
Total	100.57		100.18		98.43		98.78		99.59		99.80		100.28	
An	79.4		78.9		72.4		70.8		76.6		72.5		65.6	
Kd Plag-Melt/Ca-Na [a]	2.89		3.15		2.63		2.79		3.76		3.61		3.26	

[a] partition coefficient describing the distribution of calcium and sodium between coexisting plagioclase and melt defined as (XPlag-Ca/XPlag-Na) / (XCa-Melt/XNa-Melt)

Table 3.5. Experimental amphibole and ilmenite compositions (QFM buffer)

	Amphibhole B1 QFM buffer						Ilmenite B1 QFM buffer		
Experiment:	153		152		151			151	
T(°C):	950		*950*		*950*			950	
wt% H_2O in melt:	*5.12*		*5.12*		*5.17*			*5.17*	
aH_2O:	1		1		1			1	
ΔQFM:	+0.09		+0.09		+0.09			+0.09	
n:	3		6		6			3	
wt%									
SiO_2	43.02	0.51	43.08	0.98	43.12	0.31	SiO_2	3.94	1.67
TiO_2	1.97	0.45	2.82	1.01	2.73	0.63	TiO_2	46.61	1.79
Al_2O_3	13.24	0.73	12.08	0.17	12.44	0.99	Al_2O_3	1.65	1.25
							Fe_2O_3	5.23	0.65
FeO*	11.62	0.13	11.83	0.34	12.11	0.27	FeO	34.28	0.07
MnO	0.16	0.05	0.14	0.04	0.14	0.04	MnO	0.43	0.03
MgO	14.51	0.43	14.63	0.22	14.21	0.16	MgO	5.78	0.17
CaO	10.64	0.22	11.37	0.38	11.14	0.46	CaO	1.04	0.48
Na_2O	2.52	0.18	2.37	0.41	2.57	0.27	Na_2O	0.06	0.03
K_2O	0.07	0.03	0.07	0.01	0.09	0.01	K_2O	0.01	0.00
Total	97.74		98.40		98.55		Total	99.04	
Structural formulae							Xilm[d]	89.22	
Si	6.11		6.14		6.14				
AlVI	1.89		1.86		1.86				
M1-3 site									
AlVI	0.32		0.16		0.23				
Ti	0.21		0.30		0.29				
Fe^{3+}	1.21		0.95		0.92				
Mg	3.07		3.11		3.02				
Fe^{2+}	0.17		0.45		0.53				
M4 site									
Ca	1.62		1.74		1.70				
Na	0.38		0.26		0.30				
A site									
Na	0.31		0.39		0.41				
Mg#g[a]	0.95		0.87		0.85				
Kd Am-Liq/Si-Al [b]	1.02		1.00		0.98			1.00	0.08
	tschermakite [c]		tschermakite		tschermakite				

[a] mg number for amphibole defined as XMg/(XMg+XFe^{2+}) x 100

[b] partition coefficient describing the distribution of aluminium and silicium

between coexisting amphibole and melt defined as (XAl-Am/XSi-Am) / (XAl-Melt/XSi-Melt)

[c] nomenclature of amphiboles after Leake et al. (1997)

[d] ilmenite (XIlm x 100) of content rhombohedral oxide calculated after Stormer (1983)

Table 3.6. Experimental glass compositions (QFM buffer)

B1 QFM buffer

Experiment:	130	129	128	127	134	132	133	131	142	141
T(°C):	1150	1150	1150	1150	1100	1100	1100	1100	1050	1050
wt% H_2O in melt:	*4.58*	2.08	1.02	0.38	*4.53*	2.37	1.49	0.85	*4.84*	3.33
aH_2O:	1	0.33	0.1	0.02	1	0.4	0.2	0.07	1	0.64
ΔQFM:	+0.2	-0.75	-1.85	-3.41	+0.09	-0.80	-1.31	-2.26	-0.01	-0.39
n:	16	3	3	5	6	5	9	6	13	11
wt% [a]										
SiO_2	50.04 0.18	50.60 0.06	50.60 0.07	50.91 0.36	50.32 0.25	50.75 0.40	51.70 0.68	51.26 0.27	50.54 0.66	51.34 0.76
TiO_2	0.80 0.05	0.84 0.00	0.87 0.05	0.92 0.08	0.80 0.03	0.87 0.02	1.04 0.09	1.19 0.14	0.90 0.05	1.07 0.10
Al_2O_3	16.03 0.23	16.70 0.18	16.76 0.14	16.79 0.40	16.90 0.12	17.62 0.33	16.53 0.82	17.52 1.25	18.78 0.25	17.95 0.93
FeO*	8.24 0.23	7.84 0.11	7.95 0.14	8.04 0.20	8.07 0.24	8.62 0.42	8.77 0.31	9.20 0.59	8.54 0.43	9.45 0.45
MnO	0.11 0.06	0.14 0.02	0.13 0.03	0.15 0.04	0.19 0.07	0.17 0.05	0.12 0.04	0.19 0.10	0.11 0.06	0.17 0.07
MgO	9.82 0.10	8.71 0.07	7.74 0.13	7.73 0.12	8.11 0.14	6.78 0.17	7.30 0.67	5.63 0.33	5.94 0.18	5.93 0.58
CaO	12.62 0.14	12.84 0.14	13.45 0.10	12.78 0.23	13.23 0.18	12.60 0.18	11.72 0.61	12.04 0.29	12.30 0.35	10.84 0.67
Na_2O	2.20 0.12	2.22 0.06	2.34 0.12	2.47 0.09	2.15 0.09	2.38 0.10	2.68 0.22	2.70 0.19	2.73 0.41	2.98 0.26
K_2O	0.07 0.02	0.05 0.05	0.09 0.04	0.10 0.02	0.09 0.03	0.08 0.02	0.08 0.03	0.11 0.02	0.08 0.05	0.10 0.04
P_2O_5	0.08 0.05	0.05 0.05	0.09 0.04	0.10 0.02	0.13 0.09	0.11 0.08	0.07 0.06	0.16 0.04	0.10 0.06	0.16 0.06
Total[b]	95.71 0.39	97.97 0.37	98.63 0.15	99.08 0.48	94.69 0.79	97.59 0.22	98.15 0.68	98.89 0.75	93.48 0.79	96.44 0.36
Mg#[c]	71.65	69.23	65.32	64.09	68.39	61.41	62.14	53.87	59.77	56.5

B1 QFM buffer

Experiment:	140	143	148	147	146	145	153	152	151
T(°C):	1050	1050	1000	1000	1000	1000	950	950	950
wt% H_2O in melt:	2.90	2.04	*5.06*	5.01	5.04	3.52	*5.12*	*5.12*	*5.17*
aH_2O:	0.51	0.32	1	0.99	0.99	0.64	1	1	1
ΔQFM:	-0.54	-0.91	+0.01	+0.02	+0.03	-0.36	+0.09	+0.09	+0.09
n:	4	7	7	6	3	6	3	2	2
wt% [a]									
SiO_2	53.06 0.49	53.07 0.57	53.26 0.62	53.50 0.29	53.77 1.65	56.14 0.68	58.46 0.33	60.06 0.44	61.33 0.88
TiO_2	1.58 0.02	2.01 0.23	1.25 0.04	1.49 0.03	1.80 0.17	1.90 0.10	1.18 0.03	1.13 0.36	1.17 0.16
Al_2O_3	18.05 0.59	17.65 1.12	19.25 0.32	18.94 0.23	18.56 1.33	17.23 0.65	17.59 0.16	16.77 0.49	17.98 1.71
FeO*	9.66 0.60	10.95 0.87	8.55 0.30	8.89 0.41	9.40 0.32	9.30 0.46	8.97 0.12	8.93 1.35	7.49 0.98
MnO	0.14 0.11	0.23 0.04	0.17 0.10	0.24 0.16	0.14 0.10	0.12 0.11	0.09 0.04	0.11 0.08	0.10 0.05
MgO	3.95 0.66	4.06 0.33	3.78 0.24	3.80 0.41	3.23 0.33	2.91 0.35	2.52 0.48	2.31 0.66	1.84 1.27
CaO	9.79 0.34	9.34 0.56	9.54 0.26	8.75 0.14	8.27 0.63	7.39 0.35	6.60 0.12	5.81 0.33	4.98 0.90
Na_2O	3.49 0.48	2.23 0.27	3.93 0.34	4.05 0.25	4.55 0.21	4.67 0.26	4.15 0.54	4.36 0.74	4.67 0.70
K_2O	0.19 0.06	0.22 0.03	0.16 0.04	0.17 0.02	0.17 0.03	0.17 0.03	0.23 0.03	0.27 0.03	0.18 0.02
P_2O_5	0.11 0.05	0.25 0.06	0.12 0.06	0.16 0.08	0.11 0.11	0.17 0.08	0.21 0.14	0.25 0.11	0.26 0.09
Total[b]	96.73 2.21	97.82 1.35	92.99 1.46	93.23 0.83	94.69 1.97	95.57 1.05	92.75 0.10	93.56 1.89	92.89 2.64
Mg#[c]	45.62	42.40	48.67	47.77	42.42	39.49	37.62	35.71	34.53

[a] oxide concentrations from microprobe are normalized to 100 wt% with all Fe as FeO* (total iron)

[b] Total from microprobe

[c] mg number for glass defined as XMgO / (XMgO+XFeO) x 100 and Fe_2O_3 and FeO content calculated after Kress and Carmichael (1991)

6. Appendix

Equation of Harvie et al. (1980):

$$\frac{\mathrm{dwt}_{H_2}}{\mathrm{d}t} = \frac{2\pi kl}{\ln\left(\dfrac{r_e}{r_i}\right)}\left[\left(f_{H_2}^{i}\right)^{\frac{1}{2}} - \left(f_{H_2}^{e}\right)^{\frac{1}{2}}\right]$$

r_e and r_i are outer and inner radii of the capsule or membrane, k is the permeability constant, l is the length of capsule or membrane, $f_{H_2}^{i}$ and $f_{H_2}^{e}$ are hydrogen fugacities inside and outside the capsule or membrane